Lehigh University
Lehigh Preserve

Theses and Dissertations

2015

Dynamic Interaction of a Marine Hydrokinetic Turbine with Its Surrounding Environment

Nitin S. Kolekar
Lehigh University

Follow this and additional works at: http://preserve.lehigh.edu/etd

Part of the Mechanical Engineering Commons

DYNAMIC INTERACTION OF A MARINE HYDROKINETIC TURBINE WITH ITS SURROUNDING ENVIRONMENT

by

Nitin Kolekar

Presented to the Graduate and Research Committee
of Lehigh University
in Candidacy for the Degree of
Doctor of Philosophy

in

Mechanical Engineering

LEHIGH UNIVERSITY

May 2015

DISSERTATION SIGNATURE PAGE

Approved and recommended for acceptance as a dissertation in partial fulfillment of the requirements for the degree of Doctor of Philosophy.

_____
Date

_____
Dissertation Director

_____
Accepted Date

Committee members:

_____
Prof. Arindam Banerjee
(Committee Chair)

_____
Prof. Sudhakar Neti
(Committee Member)

_____
Prof. Donald Rockwell
(Committee Member)

_____
Prof. Panos Diplas
(Committee Member)

ACKNOWLEDGEMENTS

TABLE OF CONTENTS

Page

LIST OF FIGURES

x

LIST OF TABLES

NOMENCLATURE

A_t	turbine rotation disc area [m^2]
A_c	channel cross-section area [m^2]
a	axial induction factor
a'	angular induction factor
B	blockage ratio
b	channel depth [m]
C_d	drag coefficient
C_l	lift coefficient
C_p	power coefficient
C_T	thrust coefficient
c	chord length [m]
C_p	power coefficient
$C_{p_{Measured}}$	measured power coefficient
$C_{p_{Corrected}}$	corrected power coefficient to account for blockage
D	turbine diameter [m]
d_τ	particle image diameter [m]
d_r	pixel pitch [m]
d_p	particle diameter [m]
$dQ\ \&\ dT$	torque & thrust developed on a blade element at radius r [N & N.m]
$F_{Hub}\ \&\ F_{Tip}$	hub loss & tip loss correction factors
F_{shear}	shear force at bypass and wake interface [N]
Fr	Froude number
f	body force vector per unit volume [N/m^3]
$f\#$	f-number of camera lens
g	acceleration due to gravity [m/s^2]
h_1	channel depth [m]
h_U	tip to free surface clearance [m]
M_0	laser magnification
N_B	number of blades

p	pressure [Pa]
Q	turbine torque [N.m]
R	turbine radius [m]
Re	flow Reynolds number based
Re_{Diameter}	flow Reynolds number based on turbine diameter
Re_{chord}	flow Reynolds number based on chord-length
Re_{ref}	reference Reynolds number for hydrodynamic data input
r	radius of blade element [m]
r_{hub}	hub radius [m]
T	turbine thrust force [N]
U, U_1	flow velocities [m/s]
$\vec{U}_r$	relative flow velocity in rotating reference frame [m/s]
U_{b}	flow velocity in bypass region [m/s]
U_{tip}	flow velocity at blade tip [m/s]
U_{w}	flow velocity in wake region [m/s]
U_∞	equivalent free stream velocity [m/s]
$U_{\text{Normalized}}$	stream-wise velocity normalized by channel velocity
$V_{\text{Normalized}}$	vertical velocity normalized by channel velocity
u', v', w'	turbulence fluctuations in velocity component in X, Y, and Z directions [m/s]
X, Y, Z	coordinates in the streamwise, vertical, and transverse directions

GREEK SYMBOLS

α	wake flow factor (wake flow velocity/channel velocity)
β	bypass flow factor (bypass flow velocity/channel velocity)
Δp	pressure gradient across the turbine [N/m^2]
$\Delta C_p\%$	% change in power coefficient compared to free-stream conditions
$\Delta U\%$	% change in power coefficient compared to free-stream conditions
Δt	time difference between consecutive laser pulses [seconds]
δ	displacement field [m]

δ_y	streamwise deflection
δ_z	depth of field [m]
δh_U	tip clearance ratio
λ	operating *TSR*
λ_d	design *TSR*
λ_l	laser wavelength
μ	dynamic viscosity of water [Pa.s]
Ω	turbine rotational speed [rad/s]
ω	three-dimensional vorticity field
ϕ	angle of relative flow [°]
ρ	water density [kg/m^3]
τ	Cauchy stress tensor
θ	stereo half angle [°]
θ_{po}	blade pitch angle [°]
θ_t	blade twist angle [°]
σ	local blade solidity
σ_U	standard deviation of velocity
σ_v	von-Mises Stress
σ_y	flap-wise bending stresses
$\sigma_{\Delta X}$	r.m.s. random in-plane displacement error
$\sigma_{\Delta V}$	r.m.s. random in-plane velocity error
$\sigma_{\Delta Z}$	r.m.s. random out of plane displacement error

ACRONYMS

ALE	arbitrary Lagrangian Eulerian method
BEM	blade element momentum theory
CCD	charge-coupled device
CFD	computational fluid dynamics
FEA	finite element analysis
FSI	fluid-structure interaction

GA	genetic algorithm
MHkT	marine hydrokinetic turbine
TSR	tip speed ratio
PIV	particle image velocimetry
VOF	volume of fluid
RPM	rotations per minute
r.m.s.	root mean square
SPIV	stereoscopic particle image velocimetry

ABSTRACT

A marine hydrokinetic turbine (MHkT) operating in its natural environment is subjected to dynamic effects due to variations in its operating conditions. Though the flow velocity and direction are predictable and do not undergo drastic variations as in wind turbines (wind gusts and changes in wind direction), a denser working medium due to placement in water imposes higher structural loading on turbine blades. Furthermore, a variation in water depth alters the turbine depth of immersion during operation. These dynamic conditions change the ratio between the turbine rotation disc (area) and channel area that affects blockage and hence the performance characteristics. Furthermore, variations in blade tip clearance from free surface is hypothesized to affect flow-field and performance characteristics of a marine hydrokinetic turbine, especially those operating in a shallow channel. Significant flow acceleration occurs in and around the turbine rotation plane; the magnitude of which depends on size of the turbine relative to the channel cross-section and is commonly referred to as solid blockage. In addition, the wake behind the turbine creates a restriction to the flow called wake blockage. Understanding the effects of solid and wake blockages in presence of free surface proximity on performance of MHkT is crucial for deployment and efficient operation of individual turbines. In addition, since the free surface is deformable, it is expected to modify both near and far-wake characteristics behind a turbine which must be accounted for in order to develop efficient models of MHkT farms where an array of such devices are deployed in the river bed.

In this dissertation, the dynamic interaction of a stall regulated, fixed pitch, horizontal axis MHkT with its environment is addressed through closely coupled experimental, computational and analytical studies. The analytical model was developed

based on blade element momentum theory to investigate effect of rotational speed, flow speed, blade pitch, chord length, twist angle on hydrodynamic and structural performance of turbine. The model was further extended to perform one way fluid-structure interaction analysis and a multi-objective optimization (with Genetic Algorithm) study for improving hydrodynamic and structural performance of river-turbine-prototype. To validate the results of analytical model, a three dimensional coupled- computational fluid dynamics- finite element analysis scheme was developed in ANSYS Workbench. In addition, a coupled experimental and computational study was carried out with the objective of unraveling the influence of boundary proximity and blockage effects on the turbine performance. Experimental efforts consisted of performance measurements with a lab-scale prototype in a water channel at various flow velocities, rotational speeds, and depths of immersions to understand effects of free surface proximity, Reynolds number, and Froude number on power and thrust developed by the turbine. The experimental measurements were complimented by a steady state and transient CFD analysis for flow-field characterization behind the turbine. Further, to quantify the influence of free surface proximity on blockage effects, two different models were developed: first for a closed-top channel, and second an open surface water channel (free surface proximity environment). The blockage effects were quantified in terms of percentage change in flow velocity, power coefficient, and thrust coefficient compared to an unblocked, non-free surface environment. In addition, to understand the mechanism responsible for variation of power coefficient with rotational speed and free surface proximity, stereoscopic particle image velocimetry measurements were carried out in the near-wake region of turbine at various rotational speeds and blade tip-free surface clearances. Time averaged measurements were

carried out to determine the ensemble-averaged statistics of flow quantities such as mean velocity, strain rates, Reynolds stresses, and turbulence parameters at various turbine operating conditions. In addition to free-run PIV, a phase locked PIV measurements were carried out in the wake region to study transient phenomena like wake development and propagation process, tip and hub vortices formation and propagation.

A reduction in tip-depth of immersion was observed to improve the turbine performance until it reached an optimum depth beyond which a reduction in performance was observed due to free surface interaction with wake and bypass region. For low tip clearance ratios, a significant drop (up to 5 to 10% of channel depth) in free surface was observed (from both experimental investigations and transient CFD analysis) behind the turbine with complex three dimensional flow structures that lead to a skewed wake affecting its expansion and restoration process. The percent change in power coefficient (with respect to unblocked, non-free surface environment) was found to be dependent on flow velocity, rotation speed and free surface to blade tip clearance. Flow field visualization, based on SPIV, showed presence of slower wake at higher rotational velocities and increased asymmetry in wake at high free surface proximity. In addition, significant difference in flow structures was observed between upper and lower bypass regions.

CHAPTER 1

INTRODUCTION AND OVERVIEW

1.1 BACKGROUND

Marine hydrokinetic and tidal turbines (MHkT) are a class of low head energy conversion devices which convert kinetic energy of flowing water in rivers, tides and ocean waves into mechanical work that is then converted to electrical power by suitable power-take off devices [1, 2]. The operating principle of MHkT is similar to wind turbines which are lift/drag devices as compared to conventional hydro-turbines which operate under large heads (>10 m) [3, 4]. Traditionally, hydropower has accounted for the bulk of the renewable energy production in the United States. The total electricity use in the U.S. in 2011 was 3856 TWh/yr with ~9% of that output coming from renewables; traditional hydroelectric or micro-hydro facilities contributing ~35% of the total renewable energy production [5]. However, growth of conventional hydropower plants is constrained by the number of available natural sites, large capital (initial) investment, extensive pay-back time and environmental concerns [6, 7]. In lieu of this, marine and hydrokinetic systems offer many advantages as these are portable systems with small initial set-up costs that do not require large infrastructure and can be quickly deployed [1, 2, 6, 8, 9]. A study conducted by Electric Power Research Institute (EPRI) for U.S. rivers estimated the total technically recoverable hydrokinetic power at 120 TWh/yr (~ 3% of the total electricity use) with the Lower Mississippi region contributing nearly 48% and Alaska region constituting ~17% of the total resource estimate [10]. Another study conducted by EPRI evaluated many, but not all tidal energy sites in U.S. and estimated 250 TWh/yr of tidal energy (~ 6% of the total electricity use) with 94% of the available energy in Alaska and the remaining 6% in continental United states (mostly in Washington and Maine) [11].

MHkTs are lift/drag devices similar to wind turbines, and their performance is governed by several non-dimensional quantities: (i) the tip-speed ratio ($TSR : \lambda = \dfrac{R\Omega}{U}$) which is defined as ratio of blade tip speed to fluid speed (U) (where R is turbine radius) and Ω is the rpm); (ii) solidity ($\sigma = \dfrac{N_B c}{2\pi R}$) that is defined as the ratio of the product of the blade chord length (c) and the number of blades (N_B) to the turbine circumference; and, (iii) the chord Reynolds number ($Re = \rho U c / \mu$), where ρ and μ are the density and viscosity of the fluid medium.

Unlike wind turbines, marine hydrokinetic turbines (MHkT) operate in a bounded flow environment where the flow is constrained between the free surface and the channel (river/sea) bed. In many cases, the channel depth for commercial scale MHkT installation is between 1.5D to 3D (where D is the turbine diameter) which leads to a blockage ratio (B=ratio of turbine area to channel area) greater than 0.1 [12]. Under such circumstances, the turbine is subjected to effects of solid blockage that modifies the flow-field around the turbine and hence affects its performance [13-15]. In addition, the rotational motion of the blades creates a low pressure, low velocity *wake* region behind the turbine; the rotating wake presents an additional restriction to the flow called wake blockage. Collectively, these two blockage effects result in accelerated flow near the rotor plane which in turn yields a higher performance compared to a turbine operating in an unblocked environment [16-18]. Though the solid blockage is constant for a given turbine in a given channel, the extent of wake blockage (that affects total blockage) varies with flow speed and turbine rotation speed. Quantifying the wake recovery distance behind a MHkT is thus important for designing optimum locations for multiple devices in a farm environment. Although the

problem appears to be similar to wind-farm design, important differences exist primarily due to the bounded flow environment which alters the mechanism of wake recovery. This invalidates usage of wind-farm models in which wake restoration takes place by absorbing energy from the atmospheric boundary layer which can be treated as an infinite ambient reservoir [19]. For MHkT, where a limited water depth is available, the wake is tightly restricted between channel bottom wall and free surface that limits free expansion in directions perpendicular to the bounding surfaces. Installation also plays a pivotal role; MHkT can either be bottom mounted on a pier anchored to the channel bed or can be supported from a floating platform moored to the channel bed [20]. In both cases, they are subjected to effects of boundary proximity of either the deformable free surface or the channel bed. Proximity of a turbine to the free surface presents additional complexity to flow structures and hence affects the turbine performance. The deformable free surface allows the water level to drop behind the turbine rotational plane [21]. Though the solid blockage is constant, the drop in free surface height and its deformation behind the turbine with the associated wake modifications are expected to influence the flow-field and hence turbine performance. The effects may vary significantly due to changes in effective flow conditions, operating *TSR*, Reynolds number (*Re*=ratio of inertial forces to viscous forces) and Froude number (*Fr*=ratio of characteristic flow velocity to gravitational wave velocity). The severity of this effect is expected to be function of various parameters including but not limited to blade shape (airfoil shape, chord and twist distribution), blade pitch angle, *TSR*, free surface proximity, channel wall proximity, and solid blockage itself.

Further, MHkT operate in an environment where the water velocity and water level above the turbine rotation disc undergo cyclic variations. For marine current turbines, the

period of this cycle is of the order of a day, while for hydrokinetic turbines fluctuations are seasonal and occur over entire year [22]. Therefore, for an efficient operation of MHkT it is crucial to understand effect of these fluctuations on its performance characteristics. Turbine blades are made from airfoil sections and any change in flow velocity modifies its lift/drag characteristics affecting turbine performance. If *TSR* is to be held constant at the design *TSR* value, an increase in flow velocity implies increased rotational speed. Thus, for a similar *TSR* value, turbine performance is different at different flow speed and rotation speed combinations. The higher the turbine rotation speed, the stronger the wake and higher the wake blockage that improves turbine performance. The variation in performance with flow speed (and rotational speed) may be due to variation in Reynolds number or in wake blockage or both.

Thus, when MHkT operates in its natural environment, it is subjected to dynamic effects of its interaction with surrounding environment. Denser incoming flow causes higher structural stresses in turbine blades. In addition, presence of MHkT in flow channel modifies the flow around it affecting not only the performance of MHkT behind it but its own performance as well. The incoming flow, deformable free surface and blockage effects, along with turbine geometry (chord, twist, pitch), and operating conditions (*TSR*, proximity to free surface and sea/river bed) affect the flow-field behind MHkT (wake and bypass – region outside wake) affecting its performance. Very little is known about this dynamic interaction between wake, bypass flow and free surface, and its effect on turbine performance. It was the principle goal of current research to address these issues which led to the following twofold objectives: first to understand and improve component level (turbine blades) performance of MHkT through fluid-structure interaction analysis, and

multi-objective optimization study. And second, to understand the dynamic effect of working environment (blockage and free surface proximity) on performance and flow-field of MHkT systems. The following sections (§1.2-1.5) summarize current state of art in MHkT performance and flow-field characterization, thereby identifying unresolved issues that motivate current work. The unresolved problems and approaches used in this study to address them are discussed briefly in §1.5.

1.2 PERFORMANCE CHARACTERIZATION OF MHKT

Hydrodynamic performance of a MHkT is governed by various operating conditions and blade profile geometry that includes parameters like *TSR*, *U*, Ω, σ, B and *Re*. Over the last decade, the flow-dynamics of wind turbines and MHkT have been investigated using computational fluid dynamics (CFD) [4, 23, 24] and laboratory scale experiments [25-29]. Blade-element-momentum (BEM) analysis which forms the backbone of wind turbine rotor design can also be used for MHkT design [30]. Apart from BEM, low-order CFD tools like vortex and panel methods can be used for hydrodynamic analysis of these devices [31-34]. In addition, computationally expensive higher-order techniques that involve solving Reynolds-averaged-Navier-Stokes equations (RANS) and large eddy simulations (LES) with turbulence models have been successfully used for hydrodynamic analysis of MHkT [4, 24, 28, 35-39]. Consul *et al.* [4] performed a two dimensional CFD analysis to understand the influence of number of blades on performance of cross flow turbines and found improved performance with a higher number of blades. Hwang *et al.* [40] investigated the effect of variation of *TSR*, chord length, number of blades and the shape of hydrofoil on performance of a variable pitch vertical axis water turbine using both experiments and numerical calculations. Duquette and co-workers [23, 24] performed

9

experiments and 2-D numerical analysis to study the effect of number of blades and solidity on the performance of a horizontal axis wind turbine. Their analysis concluded that the range of *TSR* for maximum power coefficient (henceforth referred to as C_p = ratio of turbine power to water power) depends strongly on solidity and weakly on the number of blades. This indicates that, the chord length plays an important role in defining the optimum *TSR* range that leads to maximizing the turbine performance. Mukherji *et al.* [35] performed three-dimensional steady-state CFD to understand the effects of *TSR*, solidity, blade pitch and number of blades on the performance of MHkT and reported a strong influence of *TSR* on performance coefficient for various turbine geometries. Further, increase in turbine solidity and blade numbers were reported to maximize the C_p that was observed at lower *TSR*. Batten *et al.* [39] used a coupled actuator disc-RANS based model to predict the performance and loads on a tidal turbine and obtained up to 94% agreement between numerical and experimental velocity variation measured along the centerline of the wake. LES simulations performed by Churchfield *et al*. [38] reported presence of lateral asymmetric wake behind turbine which was a result of interaction between inlet shear flow and wake rotation. Myers and Bahaj [25-27] experimentally investigated the flow field and wake recovery behind marine current turbines using mesh disk simulators and found that recovery depends on proximity to water surface, sea bed roughness (which governs vertical velocity profile and turbulent kinetic energy of flow) and to a lesser extent on rotor thrust. An experimental study by Neary *et al.* [29] on an axial flow hydrokinetic turbine in a large open channel reported velocity and turbulence quantities behind the turbine using an acoustic Doppler velocimeter and a pulse coherent acoustic Doppler profiler technique. A flow recovery of 80% was reported at ten diameters downstream the rotor plane.

1.3 OPTIMIZATION STUDIES FOR MHKT PERFORMANCE IMPROVEMENT

A large majority of the available literature on MHkT focuses on the hydrodynamics and blade optimization for improving the hydrodynamic performance and does not consider fluid structure interaction analysis. The interaction of fluid flow with the turbine structure is an important aspect of design for MHkT due to a denser working medium. This coupled fluid structure interaction (FSI) problem can be solved traditionally by two different approaches: (a) a monolithic approach in which governing equations for the structure and flow field are solved simultaneously using a single solver; and, (b) a partitioned approach in which two distinct solvers are used to independently solve two sets of governing equations described in §2 [33, 41, 42]. Young [43] performed FSI analysis on carbon fiber composite blades for a marine propeller by combining boundary element and finite element methods and validated his computational results with experimental studies. Young *et al.*[33] performed a coupled boundary element- finite element (FE) hydro-elastic transient analysis of tidal/ marine current turbines and compared results with tow- tank experiments. He *et al.* [44] performed a hydro-elastic optimization of a composite marine propeller in a non-uniform wake using CFD-FEM coupled analysis. Compared to the initial blade design, the final design with optimized ply angle and stacking sequence was reported to have 70.6% reduction in vibratory loads. Selig and Coverstone-Carroll [45] used a genetic algorithm (GA) for optimizing annual energy production (AEP) and cost of energy of low-lift airfoils for stall regulated wind turbines and found that AEP is more sensitive to rotor radius than the peak power. Belesis [46] presented GA for constrained optimization of stall regulated wind turbine and found it to be superior to classical optimization methods. GA implementation was reported to have a 10% gain in the energy

production for different sized stall regulated wind turbines. Fuglsang and Madsen [47] performed multi-disciplinary optimization on stall regulated horizontal axis wind turbine considering fatigue, maximum load and AEP. They used sequential linear programming and method of feasible directions for optimizations. Operating parameters like *TSR*, blade pitch, as well as blade geometry were found to have a significant effect on performance as well as structural strength of the turbines.

1.4   EFFECT OF BLOCKAGE ON TURBINE PERFORMANCE CHARACTERISTICS

An extensive literature review on wind-turbines was undertaken due to similarity in the working principle with MHkT. Several experimental studies have been carried out for wind turbines in both unblocked and blocked flow environments to investigate the effects of tip speed ratio, Reynolds number, blade profile, and velocity gradient that may exist across the rotor plane and turbulent wind characteristics [5, 19, 48-50]. However, the results are not directly applicable as MHkT operate in a flow medium which is fundamentally different from wind turbines; denser working fluid leads to higher structural stresses on turbine blades [33, 51]. Several experimental studies have also been performed to quantify blockage effects on turbine performance. Majority of the early experimental work was done either in wind-tunnels or water channels with the aim of validation and verification of simple physics based models of such flows [5, 13, 48]. Chen and Liou [5] experimentally investigated effects of tunnel blockage on turbine performance. Blockage effect was quantified in terms of blockage factor by measuring tunnel flow velocity with and without turbine. The blockage factor was found to be strongly related to solid blockage, *TSR*, and blade pitch angle. Higher blockage effects were observed at higher solid blockage

12

and higher *TSR* values. McTavish *et al.* [14] studied effect of blockage on initial wake expansion for different sized rotors in water channel using dye visualization technique. Higher blockage was found to narrow down the wake expansion and modify the vortex pairing behind the turbine. The presence of turbine in a tidal channel not only affects the downstream flow but also the flow upstream of the turbine. Experimental and computational investigations of Medici *et al.* [48] show influence of blockage on flow up to three turbine diameters upstream of the rotor plane. Near upstream flow showed three dimensional flow structures indicating effect of turbine geometry on incoming flow, similar to near wake flow. Lartiga and Crawford [52] used actuator disc modelling with blockage corrections to predict the performance of tidal turbine in blocked environment. Flow field data from PIV measurements and CFD simulations were used to account for blockage effect. Analytical predictions were in good agreement at lower blockage ratio but showed significant deviations at higher blockage ratios. Computational study by Sun [53] with porous discs reported localized flow acceleration in region between wake and channel bottom. Free surface drop behind the mesh disc was observed to affect wake characteristics and turbine performance as well.

1.5 EFFECT OF FREE SURFACE PROXIMITY ON TURBINE PERFORMANCE AND FLOW-FIELD

In addition to wake blockage, when MHkT is installed in a near-free surface environment to take advantage of higher flux near free surface, they may be subjected to additional blockage due to free surface deformation [54]. The proximity of turbine to the free surface provides additional restriction to flow by compressing the wake flow in radial direction. Several studies have also been performed to analyze effect of free surface

proximity on turbine performance using porous discs to replicate the turbine rotors [13, 54-57]. Myers & Bahaj [55] carried out experiments with mesh discs to study effect of disc proximity to sea bed/water surface on wake structures behind porous discs. Varying the disc proximity to sea/bed and water surface was found to affect wake structure and its recovery duration. Bahaj *et al.* [56] performed analytical and experimental study to investigate the effect of surface proximity on turbine performance. Their experiments in a cavitation tunnel and tow tank showed reduction in turbine power with decreasing blade tip-free surface clearance. Experimental investigations by Birjandi *et al.* [57] with a vertical axis hydrokinetic turbine reported improved performance with increasing free surface proximity.

Flow visualization techniques based on dye and particle image velocimetry (PIV) have been used by many researchers to identify the flow features in the wake of wind turbines and marine hydrokinetic turbines. Chamorro *et al.* [58] performed a three dimensional PIV study in the wake of a miniature axial-flow hydrokinetic turbine and reported wake expansion proportional to one-third power of the stream-wise distance. Wake rotation was observed up to three rotor diameters with higher tangential velocities near the wake core and higher radial velocities near the turbine tip. Experimental investigations by Whale [59] on a lab-scale wind turbine reported high blockage at large *TSR* values due to obstruction offered by slow moving (stream-wise) wake to free stream flow. A vortex merging and reduced vortex pitch was reported at higher *TSR* values with a plausible occurrence of wake acceleration. Flow visualization was carried out with PIV technique and a comparison was presented with rotor Vortex Lattice method which showed good qualitative agreement for wake shape, expansion and tip vortex pitch. Experimental

14

analysis by Manar *et al.* [60] through experimental study on rotating wing in a confined space concluded that the magnitude of measured blade forces was dependent on Reynolds number and blade-to wall tip clearance. The measured lift coefficients were highest for the tip clearance of $0.5c$ (c=chord length = $0.2R$, R=rotor radius). An increase in tip clearance to $3c$ and $5c$ did not show any effect on force measurements at the low Reynolds number. The case with $3c$ clearance performed similar to $5c$ case at low Reynolds number and similar to $0.5c$ case at elevated the Reynolds numbers. A stronger wall to tip vortex interaction was observed for $0.5c$ case that entrained dye off the wall into the tip vortex path. A slight upward movement of the dye streak (originating from near-wall region) was observed for $3c$ clearance without any entrainment. For a marine hydrokinetic turbine operating in near free surface environment similar phenomena are expected leading to increased thrust and torque. However, flow entrainment in this case is expected to result in free surface deformation modifying the near-wake field and its propagation downstream the turbine which is one of the primary focus of current work.

Analytical models for characterizing the turbine performance are based on application of linear momentum theory. Garrett and Cummins [61] applied linear momentum theory for flow constrained between two rigid surfaces and found increase in turbine power with increasing blockage ratio. Houlsby *et al.* [21] used linear momentum theory to analyze a pressure constrained, parallel-sided tube scenario with an extension to open channel flow. A quartic equation was presented relating the flow Froude number, blockage ratio, and flow speeds in wake and bypass region behind turbine. A similar analysis was presented by Whelan *et al.* [21] yielding a quartic equation relating above quantities. Analytical predictions were comparable with experimental data for mesh disc

15

simulator and two bladed rotor in wind tunnel and water channel for different blockage conditions. Consul *et al.* [15] investigated effect of blockage and free surface deformation on performance of a marine cross-flow turbine for different blockages and free surface boundary conditions using two-dimensional CFD modelling. The deformable free surface boundary condition lead to 6.7% performance improvement compared to closed top condition due to higher effective blockage caused by free surface deformation. Froude number (over the range studied: 0.08 to 0.13) was reported to have very small effect on power coefficient (henceforth referred to as C_p = ratio of turbine power to water power) but significantly affected the free surface drop. Recently Bai *et al.* [62] performed numerical simulations using immersed boundary method to predict marine current turbine performance under free surface flow conditions and validated it with experimental data. No significant free surface deformation was reported with turbine operating with blade tip immersed ~1× R below the free surface, where R denotes the turbine radius. Computational study by Zhou and Wang [63] investigated the effect of Froude number, turbine diameter and depth of immersion on free surface wave induced by tidal turbine and its effect on turbine performance. But the computational study was not able to conclude on the effect of depth of immersion on turbine performance. Though there is an increasing body of work focusing on experiments, computations and analytical models to quantify blockage and free-surface effects on performance, the majority of the experimental and computational studies model turbine as a porous mesh disc and analytical models are limited to actuator disc modelling [27, 53, 55, 56].

1.6   THE UNRESOLVED ISSUES: MOTIVATION AND APPROACH

1.6.1   Performance Characterization and Improvement – Fluid-Structure Interaction and Optimization

Higher power to weight ratio of MHkT (compared to wind turbines) necessitates a structurally stronger design. Majority of the optimization studies for MHkT performance improvement are directed to maximizing its hydrodynamic performance. However, an improvement in hydrodynamic performance may be accompanied by an increased structural loading on turbine blades. Hence for an efficient design of MHkT, both hydrodynamic and structural aspects of design need to be considered and coupled together.

Current work accomplishes this objective through development of a coupled hydro-structural analysis and optimization tool based of BEM and simple bending theory. The optimization scheme was validated with a detailed three dimensional CFD-FEA coupled fluid-structure interaction study. The analysis is performed for two different blades: a constant chord, zero twist design; and a variable chord, twisted design. Figure 1.1 shows a flow chart for the design approach that has been adopted in this paper. As a starting point, a hydrodynamic analysis was carried out using BEM theory to study the effect of various operating parameters on the forces and torque developed on turbine blades for a constant chord turbine. During the preliminary design process when a detailed flow field solution is not available, stresses in the turbine blade are computed based on forces obtained from BEM. The turbine blade was modeled as a cantilever beam fixed at the hub; stresses were calculated based on blade section area. The hydro-structural optimization was carried out for a constant chord blade turbine using GA in MATLAB optimization toolbox.
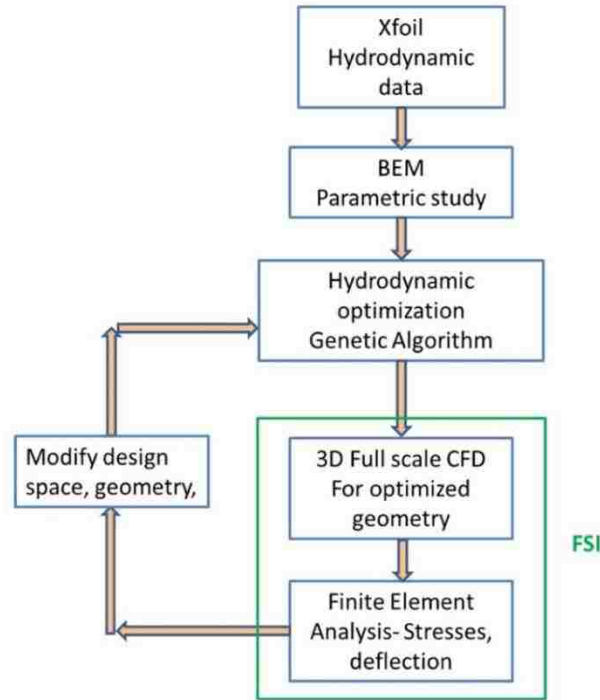
Figure 1.1: Hydro-structural optimization and design method for HKTs.

A Pareto optimal solution set obtained from GA was used as an input to the coupled FSI analysis. To check the fidelity of BEM and the optimized design, the results of lower order BEM model for a constant chord blade design are compared with a detailed three-dimensional coupled CFD-FEA analysis. The CFD domain is coupled with the structural domain using an arbitrary Lagrangian-Eulerian (ALE) scheme and FEA is performed to find deflection and stresses in the turbine components. The results of structural analysis are then used to modify the turbine geometry and design space for hydro-structural optimization, imposing limits on operating parameters and size. Further, to improve the structural strength of the turbine blade, chord and twist distributions are added to the turbine blade. A multi-objective (hydro-structural) optimization was performed for this variable chord twisted blade geometry to maximize hydrodynamic performance and minimize structural stresses in turbine blade.

1.6.2 Experimental Investigations for Performance Characterization in Free Surface Environment - Performance Measurements and CFD Study

MHkT operates in an environment where flow is bounded between free surface and channel bed (Figure 1.2). A close proximity to free surface is expected to affect wake recovery and flow structures in a near-wake region that might affect turbine performance. To the knowledge of authors, there is no quantitative computational or experimental study exploring the effect of blockage and wake-bypass flow interaction aiming to determine optimum depth of immersion for MHkT installations.
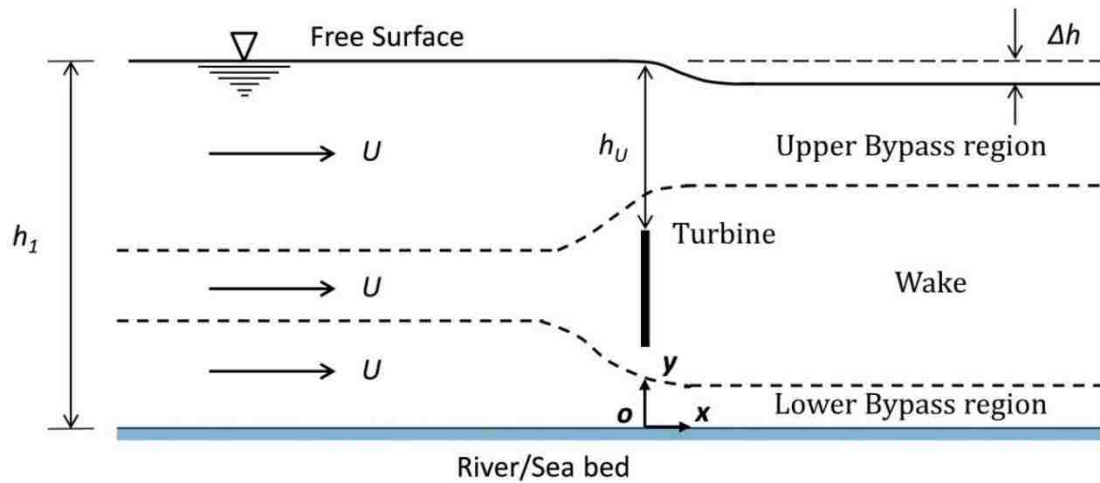
Figure 1.2: Schematic of flow around MHkT in a shallow channel showing wake, upper bypass and lower bypass regions

During current study, we report results of computational and experimental investigations to quantify the effect of blockage and boundary proximity on the performance of a three bladed MHkT. Experimental investigation are augmented by a flow field characterization with steady and transient computational fluid dynamics study. Three dimensional CFD with rotating reference frame technique was used to quantify the effect of Reynolds number and blockage ratio on turbine performance characteristics. Transient CFD calculations for wake and free surface flow characterization take into account

19

buoyancy effects and free surface effects using a volume of fluid (VOF) approach [64]. Experiments were carried out in an open surface water channel with a constant chord, zero twist hydrokinetic turbine under various operating conditions. Flow speed, rotational speed and turbine submerged depth were varied during the experiment to study their effects on turbine performance. Flow speed was varied from 0.5m/s to 0.73m/s to achieve different Froude numbers [0.20, 0.27, 0.3]. Further, to investigate the effect of surface proximity, turbine submerged depth was varied so that blade tip to free surface clearance (h_U) is between 0.01m - 0.22m. This lead to turbine tip clearance ratios (δh_U) of 0.03 to 0.73 (see Figure 1.2), which represents the ratio of water height above turbine rotation disc (h_U) up to free surface to the turbine diameter (*D*). Current experimental and computational investigations will enhance our limited understanding of the flow-field around MHkT in its natural environment. Further, experimental investigations will provide useful means to quantify the effect of boundary proximity on MHkT performance thereby facilitating MHkT site selection and deployment process.

1.6.3   Experimental Investigations to Quantify Blockage Effects for Turbine Operating in Free Surface Environment- Performance Measurement and Stereoscopic PIV Study

The majority of the earlier reported experimental investigations attempting to quantify effect of blockage on turbine performance are limited to a turbine operating at single flow speed and/or single depth of immersion and very little is known about effect of free surface proximity on performance and flow dynamics of MHkT. To the authors knowledge, current work is the first to report experimental findings of force measurements

(thrust and torque) and flow-field visualization for MHkT operating over a range of flow velocities in near free surface environment.

The current work is aimed to contribute towards understanding the influence of flow velocity and free surface proximity on blockage effects thereby identifying the governing flow physics through an experimental study. The blockage effects are quantified in terms of increase in flow velocity, increase in power and thrust coefficient. The experimental investigations are supported by stereoscopic particle image velocimetry (SPIV) based flow-field visualization to identify the governing mechanisms responsible for performance variation. Experimental investigations are conducted on a three bladed, constant chord, zero twist hydrokinetic turbine in a $0.61\text{m} \times 0.61\text{m}$ cross section water channel. The turbine was subjected to various flow speeds, rotational speeds and depth of immersions. The torque and thrust data was obtained from a submerged torque-thrust sensor connected in-line with the turbine axis. Experimental data was corrected to account for the effect of blockage on turbine performance, to arrive at unblocked dataset. Two different formulations were developed; first for a closed-top water channel and second, for an open surface water channel that incorporated presence of free surface. A comparison is presented between unblocked data and blocked experimental data at various flow velocities, rotational speeds and depths of immersion. Further, to identify the flow structures associated with wake blockage and free surface deformation, a quantitative flow visualization was carried out with SPIV technique (both time averaged and phase averaged) in the near-wake region of MHkT.

1.7   Outline of Dissertation:

This dissertation is organized as follows: Chapter 1 presents the introduction and overview of marine hydrokinetic turbines-design, analysis, and working environment. A review of recent analytical, computational and experimental work is presented that motivated the current research. In chapter 2, various methods that were developed/used during current work are discussed. Chapter 3 demonstrates the use of analytical and computational models to perform multi-objective optimization study for MHkT. In chapter 4, a coupled computational and experimental investigation is presented to understand effect of boundary proximity and blockage on turbine performance and flow-field. Finally chapter 5 presents the results of flow visualization (SPIV) study for near-wake field of MHkT with the aim of identifying the variation of the flow structures behind turbine (in the upper-bypass, lower-bypass and wake region) and relate them to the variation in turbine performance characteristics.

CHAPTER 2

ANALYTIC, COMPUTATIONAL FRAMEWORKS AND EXPERIMENTAL SETUP

During current work analytical, computational and experimental techniques were developed to investigate effect of operating conditions on flow-field and performance of MHkT. The analytical model was developed based on blade element momentum theory that was used for design and analysis of MHkT prototype. The computational study consisted of computational fluid dynamics investigations using steady state and transient techniques. The experimental setup was developed which comprises a lab-scale MHkT prototype loaded by a stepper motor that was submerged inside a water channel for performance and flow-field investigations. This chapter describes theory and development of these techniques which were used during current work.

2.1 ANALYTICAL AND COMPUTATIONAL MODELING FOR PERFORMANCE CHARACTERIZATION OF RIVER TURBINE PROTOTYPE*

2.1.1 BEM Theory

The analytical model was derived based on blade element momentum theory, originally attributed to Betz [65-67] and Glauert [30] which is a combination of blade element theory and momentum theory. According to the blade element theory, forces on a turbine blade can be obtained by dividing the blade into a number of hydrodynamically independent elements [68]. Hydrodynamic forces on these elements are calculated based on local flow conditions using two dimensional lift-drag data. The forces on these elements are then summed together to find the total force on the turbine blade. Aerodynamic data: lift coefficients (C_L) and drag coefficients (C_d) for the SG6043 hydrofoil that were adopted for our MHkT blades are obtained from Xfoil [69]. Preliminary structural analysis is based

Please refer to Chapter 3 for detailed description of analytical and computational models.

on an assumption that the turbine blade can be modeled as a cantilever beam supported at the blade root and flap-wise bending moment can be found from thrust forces acting on the blade.

2.1.2 Fluid-structure interaction analysis

The FSI problem involves a fluid domain and a structural domain interacting with each other at a fluid-structure interface. During current study, FSI analysis was carried out in ANSYS Workbench by coupling CFD and FEA solvers. The load transfer at the interface is done using arbitrary Lagrangian-Eulerian (ALE) formulation [33, 41, 42, 70]. The fluid-structure interface is the common boundary between the two domains where data transfer takes place. The CFD analysis was performed using a steady state approach (rotating reference frame) to take into account the effect of turbine rotation by transforming an unsteady flow in an inertial (stationary) frame to a steady flow in a non-inertial (moving) frame. The fluid forces from CFD analysis were then mapped onto the FEA model to find stress field in turbine blades. The details of CFD and FEA methodologies used during current work are presented in § 3.2.

2.1.3 Multi-objective optimization

To maximize the hydrodynamic and structural performance of turbine blades, the analytical model described in § 2.1.1 was incorporated in a multi-objective optimization scheme that was developed in MATLAB using Genetic Algorithm (GA). The problem consists of finding a set of decision variables: blade pitch, *TSR* and chord length which optimizes C_p and thrust forces. The objective function $F(x)$ is defined as:

$$F(x) = [f_1(x), f_2(x)], \text{ where } f_1(x) = -C_p(\theta_{po}, TSR, c), \quad f_2(x) = +T(\theta_{po}, TSR, c) \quad (2.1)$$

GA algorithm is designed to minimize both $f_1(x)$ and $f_2(x)$; the negative sign on C_p and positive sign on T ensure that both hydrodynamic and structural performances are maximized.

2.2 COMPUTATIONAL FLUID DYNAMICS FOR LAB-SCALE TURBINE MODEL: STEADY AND TRANSIENT ANALYSIS FOR LAB PROTOTYPE IN FREE SURFACE ENVIRONMENT

To understand the flow-field around a marine hydrokinetic turbine operating under various Reynolds number and boundary proximity conditions, a three dimensional CFD analysis was carried out using both steady state and transient solver schemes. Steady state analysis was carried out using multiple reference frame approach in CFX as described in earlier section. A moving mesh technique was adapted for transient simulations for which inner domain containing turbine rotates at specified angular velocity during each time step until convergence for continuity and momentum equations is reached. The flow domain consisted of 3.5 million hybrid cells with prism layers on the turbine surface for boundary layer resolution (Figure 2.1). A grid convergence study was carried out by varying the mesh size from 1.5×10^6 cells to 4×10^6 cells and a mesh with 3.5 million cells was found to be optimum from computational and accuracy standpoint which resulted in less than 5% variation in torque compared to a finer mesh of 4×10^6 cells. The mesh used for fluid domain is such that average y^+ (which defines distance of first mesh node from the wall) is 2.2 with y^+ ranging between ($0.1 \leq y^+ \leq 9$) for the highest flow speed and RPM case, i.e. U = 0.9m/s, TSR = 8 that corresponds to tip speed velocity of 7.26m/s. Reynolds averaged Navier-Stokes (RANS) equations were solved using κ-ω SST turbulence model for which $y^+ \leq 10$ is acceptable for predicting boundary layer separation effects [71, 72].
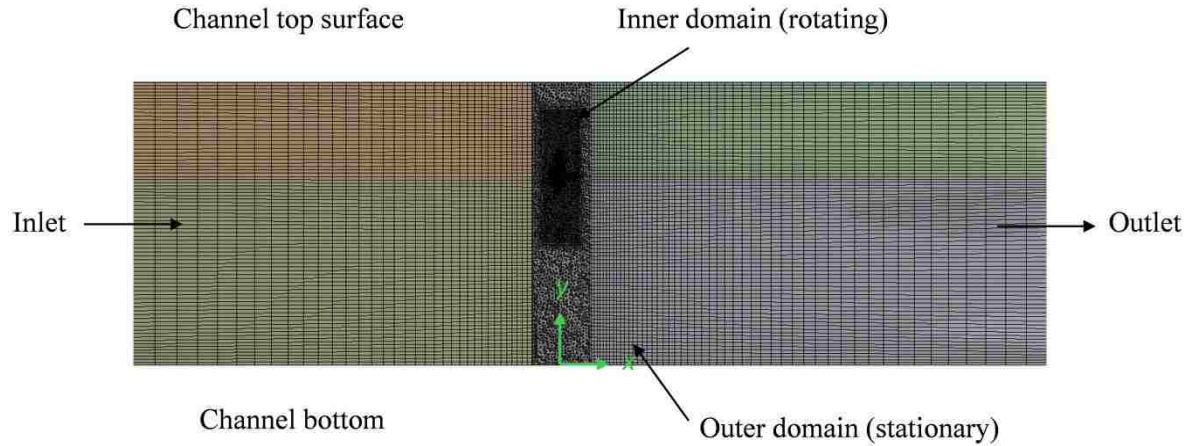
Figure 2.1: Computational mesh used for CFD study

The simulation domain for current study was modeled to an actual water channel test section of size 0.61m × 0.61m and 1.98m long. A uniform velocity of 0.5m/s was specified at the inlet. The channel outlet was specified as an outlet boundary condition with relative pressure of zero. The reference pressure for simulations was set to atmospheric pressure. The channel walls were modeled as no-slip walls and channel top is modeled as entrainment with zero relative opening pressure. With entrainment option at channel top surface, the flow direction is not specified but the flow solver locally calculates the flow direction based on flow velocity field. Buoyancy effects were modeled during transient simulations but were neglected for steady state analysis. The tunnel bottom was specified as a reference for gravity and hydrostatic pressure calculations along the channel depth. Transient simulations were carried out for flow velocity of 0.5m/s and rotational speed of 200RPM which corresponds to *TSR* (ratio of blade tip speed to flow speed) of 5.85. Time step was selected such that turbine rotated 2° during each time step which lead to average CFL (Courant–Friedrichs–Lewy condition) number of less than 5. CFL number defines a necessary condition for numerical stability of a hyperbolic partial equation. The restriction

27

on CFL number depends on the type of solver (discretization scheme) used for CFD analysis. For explicit solver, CFL<1 provides good convergence, while for implicit solver higher values of CFL are acceptable. Current CFD analysis was performed with an implicit solver within CFX for which CFL<5 was acceptable from numerical stability and expense standpoint [73].

Further, to ascertain the convergence with respect to time step size, an independence study was performed by varying time step size such that the turbine blade rotated 5°, 3°, 2° and 1° per time step. The difference between calculated power coefficients with respect to 2° case was 11%, 7%, 0% and 1.5% respectively. Thus, a time step that corresponds to 2° rotation was chosen for current analysis considering numerical stability, accuracy and computational expenses. The fluid domain was initialized with a flow velocity of 0.5m/s and turbulence intensity of 5% throughout the domain. In addition, the hydrostatic pressure at every point (and time step) in the domain was determined from density, volume fraction and hydrostatic head at that instant of time using a user defined function. The turbulence boundary conditions at inlet and outlet were specified as turbulence intensity of 5% and turbulent viscosity ratio of 10%. The convergence criteria for r.m.s. residuals of continuity, momentum, and turbulence quantities were set to 10^{-5}. During transient simulation, initial free surface height at the channel outlet is specified as 95% of the inlet height (5% free surface drop). This assumption was based on the blade element momentum calculations incorporating a quartic equation relating blockage ratio, Froude number, bypass flow and wake flow for current turbine prototype and operating conditions [21, 50]. In addition, during experimentation, the free surface height at the channel exit was found to be dependent on flow speed, rotational speed and depth of immersion that varied from 1% to

5% of channel depth. Since the value of the free-surface drop is not known *a priori*, a value of 5% obtained from BEM predictions which also corresponds to the maximum drop measured during experimentation was used in all simulations. The dynamic variation of free surface height along the channel length (and width) is determined during transient simulations using VOF formulations. Free surface simulations were carried out in ANSYS CFX 15.0 using multiphase modeling with a homogeneous model which uses the VOF approach and is based on the concept of fluid volume fraction. A common flow field, temperature and turbulence field is shared by all fluids and for a given transport process, transported properties (except volume fraction) are assumed to be same for all phases [35]. The VOF model as developed by Hirt and Nichols [64] is based on the Eulerian approach (volume-tracking) where fluid flows through a fixed mesh. The VOF method assumes that each control volume contains only one phase (water, air or interface between the two, in this case) and solves only one set of momentum equation for all phases (Equation 2.2):

$$\frac{\partial}{\partial t}\left(\rho u_j\right) + \frac{\partial}{\partial x_i}\left(\rho u_i u_j\right) = -\frac{\partial P}{\partial x_j} + \frac{\partial}{\partial x_j}\mu\left(\frac{\partial u_i}{\partial x_j} + \frac{\partial u_j}{\partial x_i}\right) + \rho g_j + F_j \qquad (2.2)$$

where, u represents fluid velocity components, P is fluid pressure, μ represents effective fluid viscosity, ρ is fluid density, g is acceleration due to gravity, and F represents body forces. In this approach, actual interface is not tracked but, is reconstructed from other flow field properties like volume fraction. A step function (α) is used to define presence or absence of water within the computational domain. A value of 1 defines presence of water and value of zero defines presence of air within the control volume. The control volumes for which α are neither zero nor one, represent the interface region between water and air.

The tracking of the interface between the fluids is accomplished by solving the volume fraction continuity equation for one of the phases (q^{th} phase in Equation 2.3).

$$\frac{1}{\rho_q}\left[\frac{\partial}{\partial t}\left(\alpha_q \rho_q\right)+\nabla\cdot\left(\alpha_q \rho_q \vec{v}_q\right)=\sum_{p=1}^{n}\dot{m}_{pq}-\dot{m}_{qp}\right] \tag{2.3}$$

where, $\dot{m}_{qp}$ is the mass transfer from phase q to phase p and $\dot{m}_{pq}$ is mass transfer from phase p to phase q. It was assumed that the interface between the two phases remain distinct and well defined so that air does not get entrained into water.

2.3   FACILITY, EXPERIMENTAL SET-UP AND MODEL PROTOTYPE

All experiments were carried out in an open surface recirculating water channel at Lehigh University with a test cross-section size of 0.61m×0.61m and length of 1.98m (Engineering Laboratory Design, USA). This facility is equipped with a 25HP single stage axial flow propeller pump with maximum discharge of 5590 gallons per minute. The propeller pump RPM and hence the test section flow velocity is controlled and regulated through a transistor inverter type variable frequency controller (Toshiba Model VFAS1-2185PM-HN). The flow velocity can be varied from 0.03m/s to 0.94m/s and can be measured within an accuracy of $\pm 2\%$. The flow quality is such that the turbulence intensity is maintained to a value of less than 1%.

2.3.1   Turbine prototype

The model prototype used for current study is a three bladed, 0.14m radius (R), zero twist, constant chord (0.01676m) blade turbine made from corrosion resistant aluminum alloy (Figure 2.2). Turbine blades are formed from SG6043 airfoil on a five-axis CNC machine. Turbine blades are held together inside a two-part hub and their orientation can

be changed to adjust blade pitch angle to the desired value. To limit the number of independent variables to a minimum, all experimental runs were performed with turbine blades oriented at 10° blade pitch. The turbine prototype when operated in our facility leads to an area based blockage ratio of 16.5%.
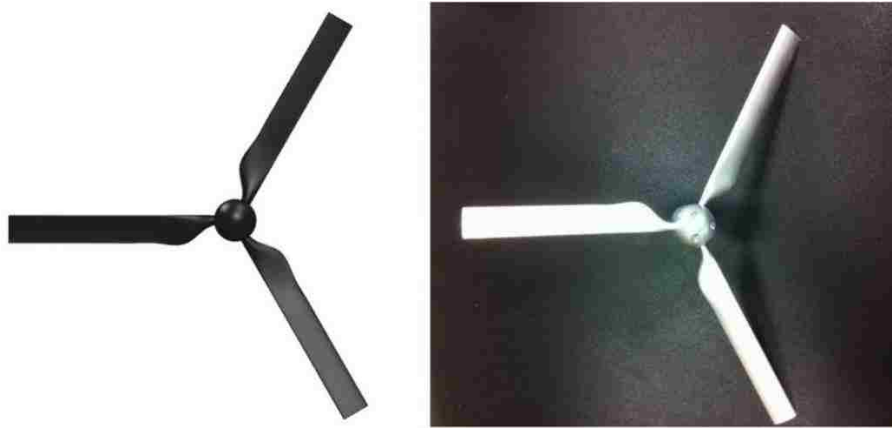
Figure 2.2: CAD model and photograph of turbine prototype used for current study [R=0.14m]

2.3.2 Experimental setup

Designing an experimental set-up that can operate in water and cover full operating *TSR* range was a challenge. Our initial attempts consisted of measuring the turbine torque using strain gauges attached to a vertical shaft (outside the water channel) which was connected to the turbine shaft through a pair of bevel gears. The turbine was loaded through a magnetic particle clutch to control its RPM at various flow speeds. But the torque measurements in this case were flawed as the vertical shaft was subjected to both thrust and torque forces transferred from the turbine. Thus, the vertical shaft was acting as a beam under combined bending and torsional loading, and hence, the strain measured on it was a combined effect of thrust and torque and not the pure torque. To address this issue, a submerged watertight enclosure was designed in which magnetic particle clutch was

31

placed. Though this scheme was able to take accurate measurements of torque, it was not able to capture full *TSR* range. In this configuration, the turbine had a tendency to stall with increasing loading. To overcome this problem, finally a magnetic particle clutch was replaced by a stepper motor that maintained a precise rotational velocity in addition to providing a constant loading on the turbine.

The final experimental setup (see Figure 2.3) consisted of a lab scale model hydrokinetic turbine attached to a horizontal shaft, driven by a stepper motor which maintained a precise rotational velocity through a micro-stepping driver and controller mechanism. The stepper motor used for current study was NEMA23 series, 24VDC motor with resolution of 1600 micro-steps per revolutions. The stepper motor was connected to the turbine shaft through a flexible coupling. The motor and flexible coupling were enclosed inside a watertight acrylic cylinder, which was then connected to a thrust torque sensor (Model # TFF400, Futek Inc.). The acrylic cylinder was continuously pressured and purged to avoid water leakage into the system.

1 – Turbine, 2 – Flexible Coupling, 3 – Motor, 4 – Thrust-Torque Sensor,
5 – Support Structure, 6 – To Motor Controller, 7 – To Data Logging
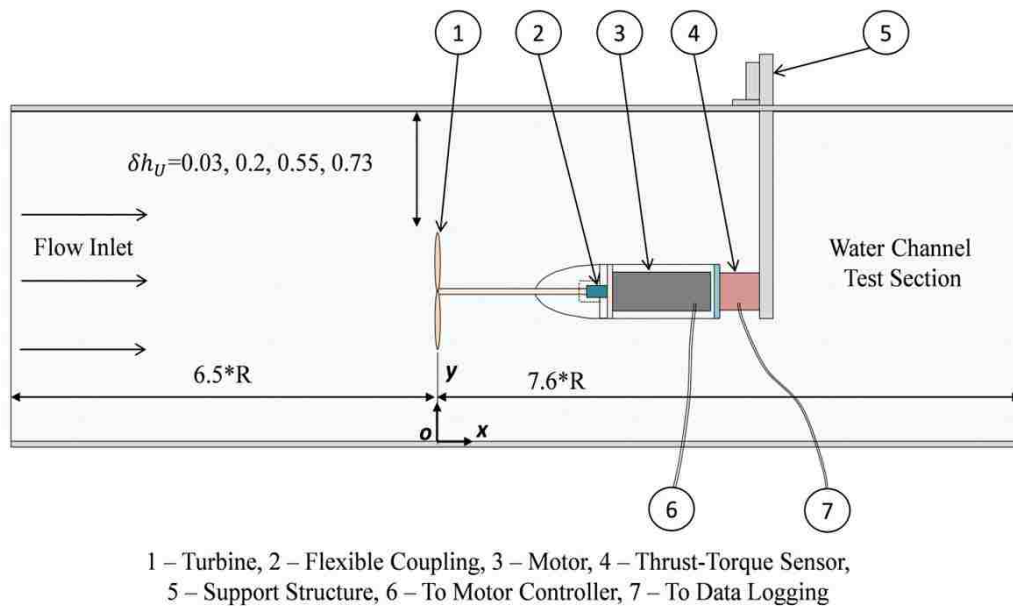
Figure 2.3: Schematic of experimental set-up [*R*=0.14m]

Finally, the reaction torque-thrust sensor was fixed to a vertical post, which was connected to a horizontal frame supported at channel top. The vertical post can be raised or lowered inside the water channel to vary the free surface proximity of turbine. During experimental run, data from torque-thrust sensor was continuously monitored and acquired on a desktop computer at high sampling rate of 500 samples/second for further analysis.

2.4   STEREOSCOPIC PARTICLE IMAGE VELOCIMETRY:

During present study, a high resolution two dimensional three component digital stereo-PIV [74-76] system was used for flow-field investigations to characterize wake structures, vortex structures, and flow in upper and lower bypass regions. Figure 2.4 shows a schematic of PIV system (TSI Inc.) used in the present study. The PIV system consists of three main components: (1) imaging subsystem which comprises laser, beam delivery system and light optics, (2) image capture subsystem which comprises of CCD camera, camera interface, and a synchronizer-master control unit, and (3) Analysis and Display subsystem. For PIV measurements, the flow medium (water) was seeded with 13µm diameter hollow glass spheres (Potter Industries-SH400S20) that were illuminated with a 100mJ pulse, 100Hz, 532nm wavelength dual Nd:YAG laser. The light sheet optics consist of a cylindrical lens which diverges the light in one direction and a spherical lens which waists the laser light into a thin sheet with ~2mm thickness at the waist. The image capture subsystem consisted of two high-resolution digital cameras in an angular displacement configuration as shown in Figure 2.4. The Scheimpflug condition is satisfied with Scheimpflug tilt-axis mounts by adjusting lenses and camera bodies. A synchronizer unit communicating with the host computer through INSIGHT4G software, controls the timings of laser pulses for illumination and camera triggers for image captures.
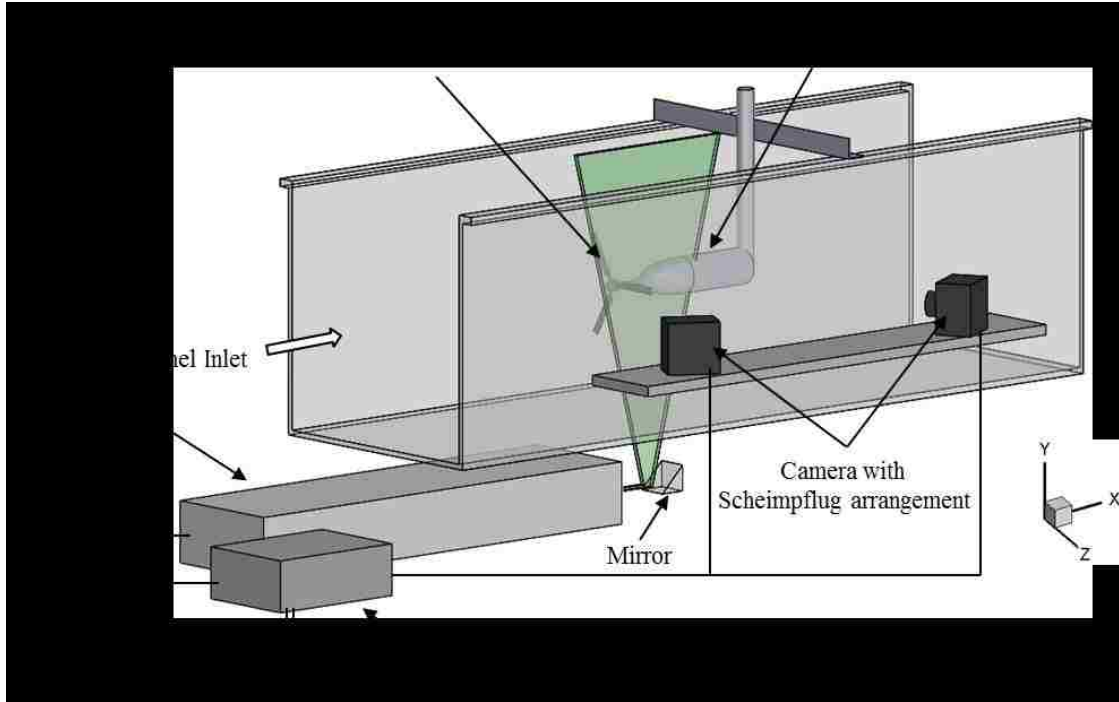
Figure 2.4: Three dimensional model of experimental set up for stereo-PIV measurements

An in-situ calibration was performed with a dual plane target to determine the mapping functions between the image planes and actual measurement plane in the flow. The mapping function used is taken to be a multidimensional polynomial, which is third order for the X- and Y-directions parallel to the laser sheet plane, and first order for the Z-direction normal to the laser sheet plane. A multi-pass frame-to-frame cross-correlation technique was employed to obtain 2D displacements in each image plane of the two cameras. A recursive Niquist grid involving initial spot dimensions of 64 pixels $\times$ 64 pixels and final spot dimensions of 32 pixels $\times$ 32 pixels was employed for this purpose leading to 4.5×4.5 mm^2 interrogation region size. An effective overlap of 50% of the interrogation windows is employed in the PIV image processing. The 3D flow velocity vectors were then reconstructed by using the mapping functions obtained by the in-situ calibration procedure and the 2D displacements from each camera. Free-run PIV measurements were performed where a series of 2000 images were taken to determine the ensemble-averaged statistics of

flow quantities such as mean velocity, Reynolds stress, and turbulent kinetic energy at various turbine operating conditions. In addition to free-run PIV, a phase locked PIV measurements were carried out to study transient phenomena like wake development and propagation, tip and hub vortices formation, and propagation and, to understand the dynamic interaction of wake with bypass flow regions. A Hall Effect sensor is connected to the turbine shaft to detect blade location during its rotation cycle. A trigger signal is sent to the synchronizer unit when a preselected turbine blade reaches horizontal position during its rotation cycle. This initiates the PIV process of laser illumination and camera captures. A total of 500 frames of instantaneous measurements were carried out to determine phase-averaged flow statistics in the wake and bypass regions of the turbine. Data from SPIV flow visualization was then used to identify the flow structures in the near-wake region of MHkT to understand the mechanism governing the performance variation.

2.5 BLOCKAGE CORRECTIONS FOR EXPERIMENTAL DATA

Measured experimental data was corrected to take into account the effect of flow acceleration around the turbine due to restriction offered by turbine to the channel flow (blockage). The blockage correction methodology used during current work is derived based on application of linear momentum theory. Two different blockage corrections schemes were developed: first for a constant volume boundary domain which is representative of a closed wind tunnel or closed-top water channel. The second blockage correction scheme is for flow in an open surface water channel which takes into account the effect of free surface. A concise formulation of both these methods is presented below.

2.5.1 Blockage Correction Technique for Closed-Top Water Channel

This method models the flow domain (two dimensional) as a parallel sided tube (confined flow) – representative of a turbine operating in a wind tunnel or a water channel with a closed top or in a water channel but away from free surface (Figure 2.5).
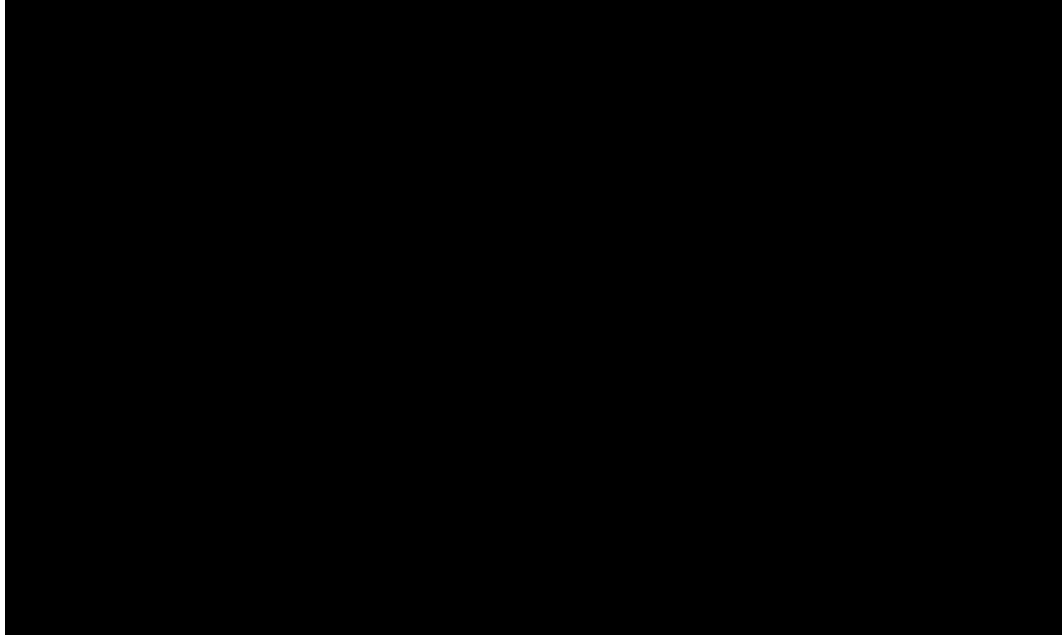
Figure 2.5: Blockage correction formulations with actuator disc theory for MHkT operating in a bounded (closed-top water channel) environment

The model is based on a linear momentum actuator disc theory and uses conservation of mass and momentum to arrive at flow velocities in various regions of tunnel. Flow domain consists of a stream tube that passes through the edge of an actuator disc (representing turbine) and expands behind the turbine rotation plane forming a wake region. The rest of the flow is called as bypass flow, in which flow acceleration takes place. Consider an actuator disc of an area A_t in a channel of cross-sectional area A_c as shown in Figure 2.5. Blockage ratio is then defined as: $B = A_c/A_t = {}^1/_{R_B}$. Consider five sections along the length of channel: 1-1 far upstream the turbine, 2-2 and 3-3 immediately before and after

the turbine, 4-4 in the far wake and 5-5 far downstream the turbine, where mixing has already occurred and velocity is uniform across the depth of channel. Section 4-4 is characterized by a uniform pressure, but varying velocity. Let T be the thrust force from the actuator disc on the fluid and X be a reaction between turbine flow and bypass flow. Subscripts t and b denotes turbine flow and bypass flow. Let α and β denote flow coefficient in turbine flow region and bypass flow region respectively, i.e. ratio of local flow velocity to tunnel flow velocity. Applying conservation of momentum between sections 1-1 and 4-4:

$$F_{shear} - T = \rho q_{4t} U_{4t} - \rho q_{1t} U_{1t} + \rho q_{4b} U_{4b} - \rho q_{1b} U_{1b} \tag{2.4}$$

$$pAR_B - p_4 AR_B - T = \rho A U^2 \alpha_2 (\alpha_4 - 1) + \rho A U^2 (R_B - \alpha_2) \left[\frac{(R_B - \alpha_2)}{R_B - \alpha_2 / \alpha_4} - 1 \right] \tag{2.5}$$

Now making use of Bernoulli's principle in bypass region and across the turbine,

$$p_4 - p = \frac{1}{2} \rho U^2 \left(1 - \beta_4^2\right) \tag{2.6}$$

$$T = \frac{1}{2} \rho A U^2 \left(\beta_4^2 - \alpha_4^2\right) \tag{2.7}$$

The thrust coefficient can be defined as the ratio of thrust force to dynamic force imparted by fluid on the turbine.

$$C_T = \frac{T}{\frac{1}{2} \rho A U^2} = \left(\beta_4^2 - \alpha_4^2\right) \tag{2.8}$$

Using equations (2.6) and (2.7) in (2.4) and after simplification, the following relation can be obtained between turbine flows at section 2-2 and 4-4.

$$\alpha_2 = \frac{(1 + \alpha_4)}{(1 + B) + \sqrt{(1 - B)^2 + B\left(1 - \dfrac{1}{\alpha_4}\right)^2}} \tag{2.9}$$

The flow velocity in the bypass flow can be related to the turbine flow velocities by:

$$U_{4b} = U \left| \frac{R_B - \alpha_2}{R_B - \dfrac{\alpha_2}{\alpha_4}} \right| = U \beta_4 \tag{2.10}$$

Equations (2.8), (2.9) and (2.10) can be solved simultaneously to find α_2, α_4 and β_4 for a given value of C_T. The equivalent open water velocity (U_∞, in absence of blockage) can then be obtained by relating thrust coefficient and turbine flow coefficient at section 2-2 as:

$$\frac{U_1}{U_\infty} = \frac{\alpha_2}{\alpha_2^2 + \dfrac{C_T}{4}} \tag{2.11}$$

Equation (2.11) assumes that the turbine in open water and lab tunnel operates under identical conditions of (i) turbine disc flow velocity (U_2), (ii) rotation speed (RPM), (iii) and thrust force (T). Equations (2.8) through (2.10) are then used to modify blocked condition quantities $C_{p_{measured}}$, $C_{T_{measured}}$ and $TSR_{measured}$ to obtain unblocked metrics namely $C_{p_{corrected}}$, $C_{T_{corrected}}$ and $TSR_{corrected}$ respectively using Equations (2.12) through (2.14).

$$C_{P_{Corrected}} = C_{P_{Measured}} \left(\frac{U_1}{U_\infty}\right)^3 \tag{2.12}$$

$$C_{T_{Corrected}} = C_{T_{Measured}} \left(\frac{U_1}{U_\infty}\right)^2 \tag{2.13}$$

$$TSR_{Corrected} = TSR_{Measured} \left(\frac{U_1}{U_\infty} \right) \qquad (2.14)$$

Equations 2.12-28 were used to quantify increase in flow velocity and power coefficient due to blockage that varied with flow velocity, RPM and tip clearance distance as illustrated in subsequent sections.

2.5.2 Blockage Correction Technique for Open Surface Channel

The blockage correction methodology developed in the earlier section is applicable to closed-top channel or for the turbine operating away from a free surface. For a turbine operating in the vicinity of a free surface (Figure 2.6), wake re-energization and expansion process is affected by free surface drop behind the turbine [25, 56, 57]. Hence it is necessary to incorporate the effect of free surface in the blockage correction methodology discussed in section 2.6.1.
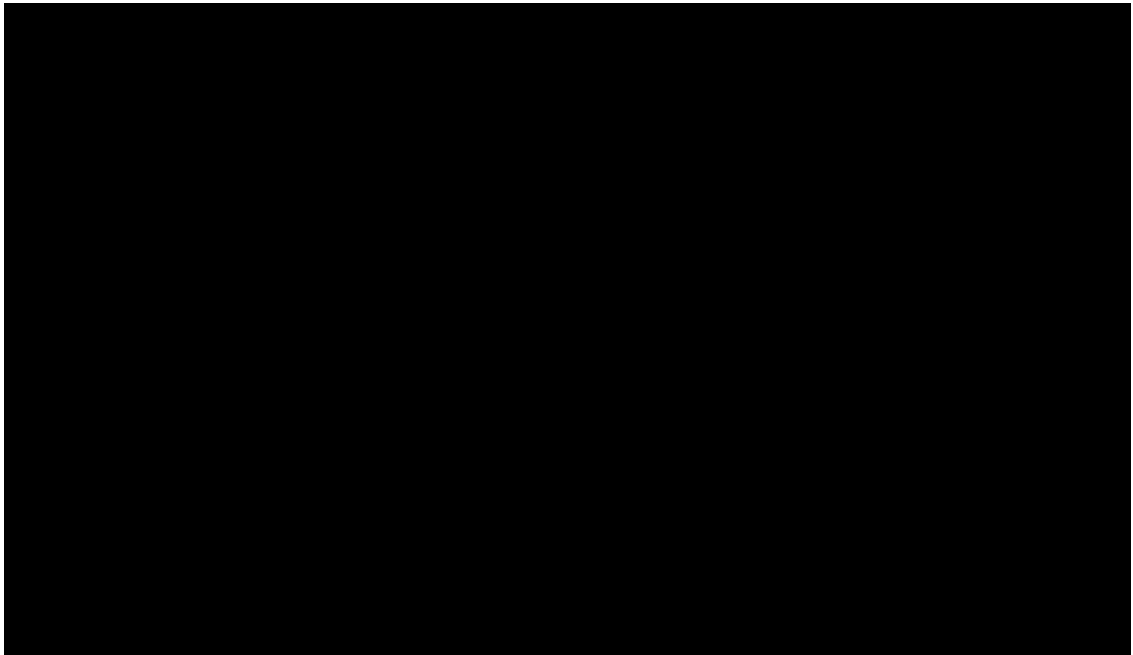
Figure 2.6: Blockage correction formulations with actuator disc theory for MHkT operating in an open surface water channel environment

This was achieved by modeling the Froude number in the blockage correction formulation. Froude number (Fr) defines the relation between characteristics flow velocity, and gravitational flow velocity $\left(Fr = U/\sqrt{gh}\right)$, where g is gravitational acceleration (m/s²), U is channel velocity (m/s), and h is water channel depth (m) upstream the turbine. The pressure head at various channel sections can be expressed in terms of hydrostatic pressure. Applying the Bernoulli's equation to bypass flow, between sections 1-1 and 2-2 and sections 3-3 and 4-4 we get:

$$h_{2t} - h_{3t} = \frac{u^2}{2g}\left(\beta_4^{\,2} - \alpha_4^{\,2}\right) = \frac{T}{\rho g A} \tag{2.15}$$

Where h_{2t} and h_{3t} are water heights at sections 2-2 and 3-3. And momentum conservation across the turbine gives:

$$F_{shear} - T = \rho q_{4t} U_{4t} - \rho q_{1t} U_{1t} + \rho q_{4b} U_{4b} - \rho q_{1b} U_{1b} \tag{2.16}$$

$$\frac{1}{2}g\left(h^2 - h_4^{\,2}\right) - \mathrm{B}b\frac{u^2}{2g}\left(\beta_4^{\,2} - \alpha_4^{\,2}\right) = U^2 h B \alpha_2 \left(\alpha_4 - 1\right) + U^2 h \left(1 - B\alpha_2\right)\left(\beta_4 - 1\right) \tag{2.17}$$

where, b is the channel width. The water height at section 4-4 can be determined by applying continuity equations to bypass and turbine flow:

$$h_4 = \frac{A_{t4}}{b} + \frac{A_{b4}}{b} = \frac{Bh\alpha_2}{\alpha_2} + h\frac{\left(1 - B\alpha_2\right)}{\beta_4} \tag{2.18}$$

Applying the Bernoulli's equation to bypass flow and after some manipulations, h_4 and β_4 can be eliminated from (2.17), (2.18) and following relation between turbine flow

coefficients and bypass flow coefficient can be derived:

$$\alpha_2 = \frac{2\left(\beta_4 + \alpha_4\right) - \dfrac{\left(\beta_4 - 1\right)^3}{B\beta_4\left(\beta_4 - \alpha_4\right)}}{4 + \dfrac{\left(\beta_4^{\,2} - 1\right)}{\alpha_4\beta_4}} \tag{2.19}$$

Equation (2.17) can be rewritten using (2.19) and definition of the Froude number as follows:

$$\frac{Fr^2\beta_4^{\,4}}{2} + 2\alpha_4 Fr^2\beta_4^{\,3} - \left(-2 - 2B + Fr^2\right)\beta_4^{\,2} - \left(4\alpha_4 + 2\alpha_4 Fr^2 - 4\right)\beta_4 + \left(\frac{Fr^2}{2} + 4\alpha_4 - 2B\alpha_4^{\,2} - 2\right) = 0$$

$$\tag{2.20}$$

The thrust coefficient is then related to flow velocities as:

$$C_T = \frac{T}{\dfrac{1}{2}\rho A U^2} = \left(\beta_4^{\,2} - \alpha_4^{\,2}\right) \tag{2.21}$$

Equations (2.18), (2.19), and (2.20) can be simultaneously solved for known values of B, Fr and C_T to calculate equivalent free-stream velocity using equation (2.11).

2.6 ERROR AND UNCERTAINTY ANALYSIS

2.6.1 Uncertainty Analysis for Experimental data

Errors in the calculations of torque and thrust coefficients were due to errors associated with measurements of: flow velocity, rotational velocity, thrust forces, and torque. For the water channel used for current experimental investigations, according to manufactures specifications (Engineering Laboratory Design, USA), the flow velocity can be can be controlled within an accuracy of $\pm\,2\%$. The accuracy of stepper motor for RPM specification was within $\pm\,1\%$ of input value which was confirmed with Hall Effect sensor

measurements. Further, the torque/thrust sensor was accurate to within $\pm$ 1% for current measurement range (torque $<$ 0.4N.m, thrust $<$ 35N). A single sample uncertainty analysis for U, RPM, thrust and torque based on Kline and McClintock [77], showed maximum uncertainty of 1% on *TSR* and $<$3% on C_T and C_p calculations.

2.6.2 Uncertainty Analysis for stereoscopic PIV measurements

Uncertainties in the measurement of velocity field from SPIV visualization technique are mainly due to random errors caused by cross-correlation uncertainty and systematic errors caused by peak locking and spatial resolution [78-81]. The procedure for determination of these errors and its application to current experimental investigations is discussed next.

2.6.3 Random Errors:

Instantaneous velocity field obtained from PIV measurements is affected by random errors which are mainly related to uncertainty in identifying particle position and determining its displacement. This can depend on light sheet intensity, particle size and density, algorithm used for particle identification and displacement calculation, and velocity gradients in flow. During PIV analysis, the particle position is identified by its centroid location. Inaccuracies in locating the particle centroid lead to errors in velocity vector magnitude and direction. If d_τ is particle image diameter, the r.m.s. error ($\sigma_{\Delta X}$) associated with locating the particle center is given by $d_\tau c_\tau$, where c_τ is a centroid constant (~0.05-0.07) whose value depends on type of interrogation method, peak location technique and irregularities of particle images [80, 81]. The particle image diameter can be determined as: $d_\tau = \left[M_0[1.5\delta_z\lambda_l + d_p{}^2]\right]^{1/2}$, where, δ_z is depth of field $\cong 4\left(1+\right.$

$\left. 1\middle/ M_0\right)^2 f^{\#2}\lambda_l$, d_p is particle diameter (~$12\mu m$), and M_0 is image magnification. The r.m.s.

error in velocity can then be determined as $\sigma_u = {}^{\sigma_{\Delta x}}\!\big/\!{}_{(M_0\Delta t)}$ which defines the minimum

resolvable velocity fluctuation. For current study, the random error in velocity was found

to be less than 1% for effective blade tip velocity (at channel velocity at 0.8m/s and

rotational speed of 180RPM).

2.6.4 Systematic Errors:

Systematic errors are the errors due to limitations on the measurement system and can

be related to calibration, optical distortion, particle slip, and size of particle relative to pixel.

Errors associated with calibration can be minimized by a careful calibration procedure

using appropriate tools. Current study uses a dual plane target which aids in precise

positioning of laser sheet. The error due to relative sizes of particle image and pixel is

called pixel locking or peak locking error and becomes important when the particle image

is smaller compared to the pixel size. This error is quantified in terms of ratio of size of

particle (d_τ) to pixel pitch (d_r). To reduce the total error (random and bias errors) particle

to pixel size ratio $d_\tau/d_r \approx 2$ is recommended [80]. The total error is dominated by random

error below d_τ/d_r value of 1 and by bias error above d_τ/d_r value of 1. For the experiments

presented in this study, the computed d_τ/d_r was approximately 1.2. The other cause of

systematic error is due to spatial resolution which depends on size of interrogation area for

PIV study. The smaller the interrogation window size, the higher the resolution. During

current PIV study a multi-pass algorithm was used with initial spot size of 64×64 and final

spot size of 32×32 pixles that lead to interrogation window size of 4.8mm (30% of blade

chord-length). The computed systematic error for current PIV measurements is ~2% for effective blade tip velocity (at channel velocity at 0.8m/s and rotational speed of 180RPM).

2.6.5 Out of plane velocity errors

In addition to in-plane random and systematic errors discussed in earlier sections, the stereoscopic measurements are also subjected to out-of-plane errors due to stereoscopic-angular arrangement of cameras. The magnitude of this error is inversely proportional to the tangent of half-stereo angle (α) and is given by: $\sigma_{\Delta z}/\sigma_{\Delta x} = (\tan(\alpha))^{-1}$, where, $\sigma_{\Delta z}$ and $\sigma_{\Delta x}$ are out-of-plane and in-plane r.m.s. displacement errors respectively [82]. During present study, the stereo-cameras were arranged such that stereo-half-angle α=~12°, which lead to out of plane ratio of 4.5.

2.7 Convergence Study

2.7.1 Convergence study for performance measurements

During experimental study for performance characterization of MHkT, torque and thrust data was obtained from a submerged thrust-torque sensor mounted in-line with the turbine. Data was acquired and averaged over a total duration of 60 seconds for each run at a sampling rate of 500 samples per second. To check the convergence of data, averaged thrust and torque are plotted against cumulative time in Figure 2.7. Averaged values of thrust and torque start converging at approximately 40 seconds as depicted in Figure 2.7.
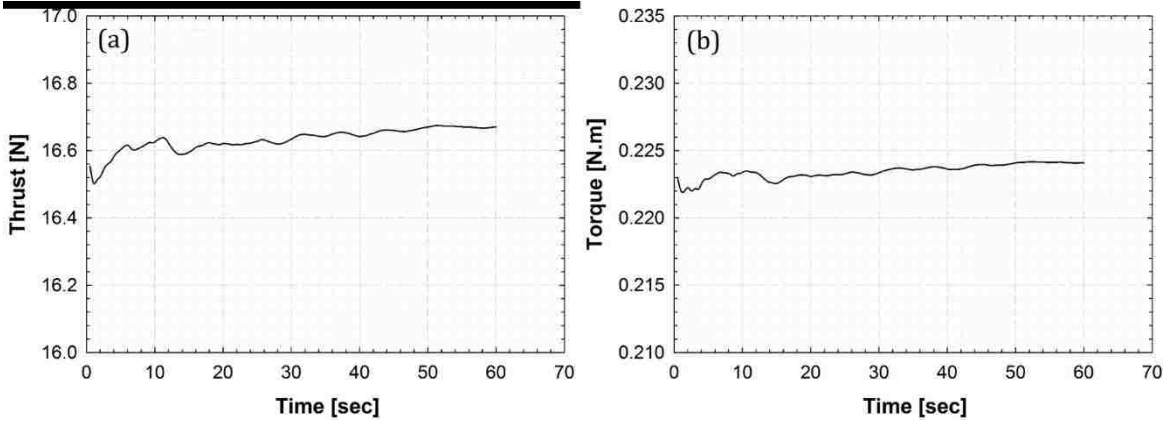
Figure 2.7: Convergence of experimental data from (a) thrust and (b) torque measurements

2.7.2 Convergence study for PIV measurements

The uncertainty of random errors decrease with increasing number of realizations due to statistical convergence. The random error in displacement measurement is inversely proportional to square-root of number realizations [78]. During current study, time averaging is performed over 2000 realizations (>80 turbine rotations). Table#2.1 shows the effect of a number of realizations on the convergence of standard deviations of stream-wise (*U*), span-wise (*W*), and vertical velocities (*V*) and shows statistical convergence around 1500 realizations.

Table 2.1: Convergence study for ensemble averaged SPIV measurements

Number of Realizations	Mean			Standard deviation		
	U	V	W	U	V	W
500	0.716	0.001	0.010	0.096	0.032	0.090
1000	0.713	0.001	0.010	0.097	0.031	0.090
1500	0.713	0.001	0.010	0.098	0.031	0.090
2000	0.713	0.001	0.010	0.098	0.031	0.090

Figure 2.8 plots convergence of phase averaged data – standard deviation of flow velocities with number of PIV realizations, where accumulated averages are plotted against the number of realizations which shows convergence around 250 realizations.
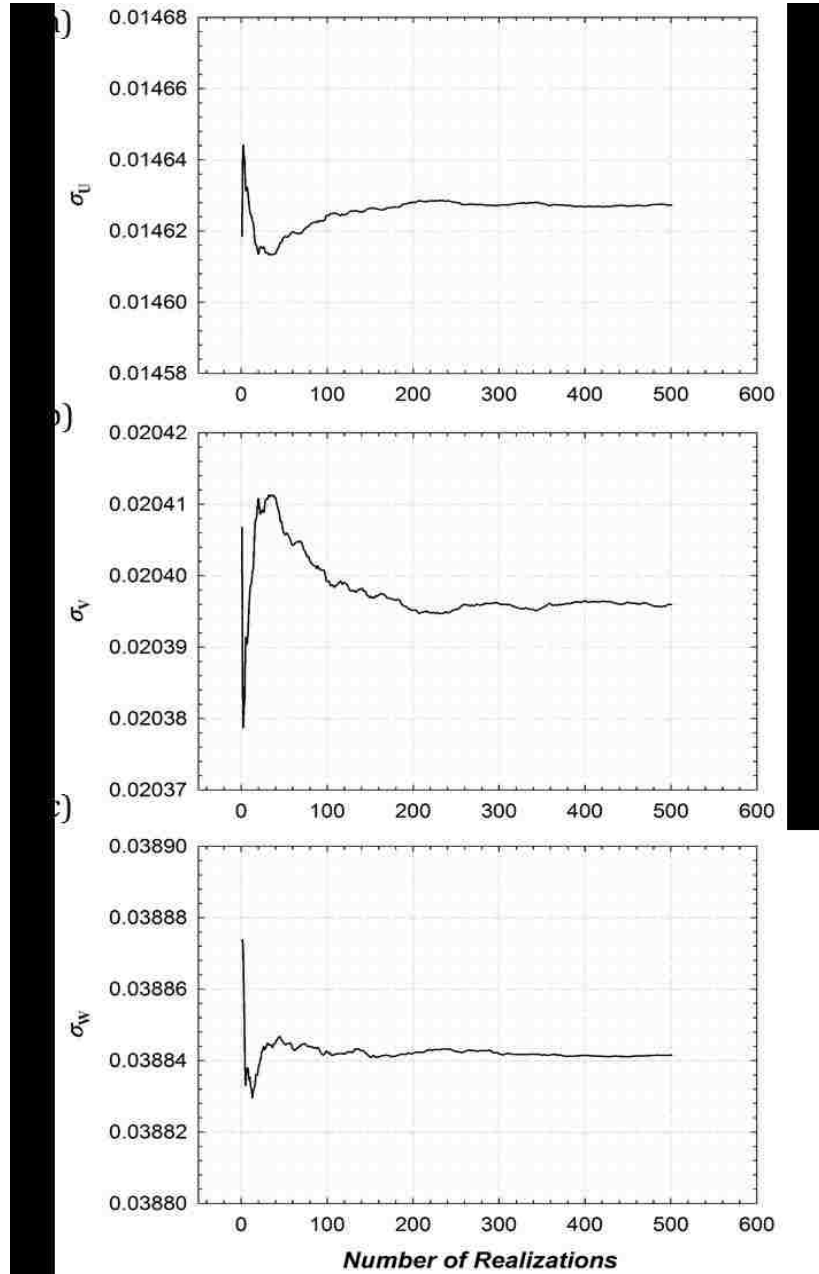
Figure 2.8: Convergence of phase averaged statistics: standard deviation of *U*, *V*, and *W* at a point (1.3*R*, 1.3*R*) in domain

46

CHAPTER 3*

A COUPLED HYDRO-STRUCTURAL DESIGN OPTIMIZATION FOR HYDROKINETIC TURBINES

3.1 BACKGROUND

Hydrokinetic turbines (HKTs) are a class of low head energy conversion devices which convert kinetic energy of flowing water in rivers, tides and ocean waves into mechanical work that is then converted to electrical power by suitable power-take off devices [1, 2]. The operating principle of HKTs are similar to wind turbines which are lift/drag devices as compared to conventional hydro-turbines which operate under large heads (>10 m) [3, 4]. Traditionally, hydropower has accounted for the bulk of the renewable energy production in the United States. The total electricity use in the U.S. in 2011 was 3856 TWh/yr with ~9% of that output coming from renewables; traditional hydroelectric or micro-hydro facilities contributing ~35% of the total renewable energy production [5]. However, growth of conventional hydropower plants is constrained by the number of available natural sites, large capital (initial) investment, extensive pay-back time and environmental concerns [6, 7]. In lieu of this, marine and hydrokinetic systems offer many advantages as these are portable systems with small initial set-up costs that do not require large infrastructure and can be quickly deployed [1, 2, 6, 8, 9]. A study conducted by Electric Power Research Institute (EPRI) for U.S. rivers, estimated the total technically recoverable hydrokinetic power at 120 TWh/yr (~ 3% of the total electricity use) with the Lower Mississippi region contributing nearly 48% and Alaska region constituting ~17% of the total resource estimate [10]. Another study conducted by EPRI evaluated many, but not all tidal energy sites in U.S. and estimated 250 TWh/yr of tidal energy (~ 6% of the total electricity use) with 94% of the available energy in Alaska and the remaining 6% in continental United states (mostly in Washington and Maine) [11].

HKTs are lift/drag devices similar to wind turbines, and their performance is governed by several non-dimensional quantities: (i) the tip-speed ratio ($TSR : \lambda = \dfrac{R\Omega}{U}$) which is defined as ratio of blade tip speed to fluid speed (U) (where R is turbine radius) and Ω is the rpm); (ii) solidity ($\sigma = \dfrac{N_B c}{2\pi R}$) that is defined as the ratio of the product of the blade chord length (c) and the number of blades (N_B) to the turbine circumference; and, (iii) the chord Reynolds number ($Re = \rho U c / \mu$), where ρ and μ are the density and viscosity of the fluid medium. Over the last decade, the flow-dynamics of wind turbines and HKTs have been investigated using computational fluid dynamics (CFD) [4, 23, 24] and laboratory scale experiments [25-29]. Blade-element-momentum (BEM) analysis which forms the backbone of wind turbine rotor design can also be used for HKTs design [30]. Apart from BEM, low-order CFD tools like vortex and panel methods can be used for hydrodynamic analysis of these devices [31-34]. In addition, computationally expensive higher-order techniques that involve solving Reynolds-averaged-Navier-Stokes equations (RANS) and large eddy simulations (LES) with turbulence models have been successfully used for hydrodynamic analysis of HKTs [4, 24, 28, 35-39]. Consul *et al.* [4] performed a two dimensional CFD analysis to understand the influence of number of blades on performance of cross flow turbines and found improved performance with a higher number of blades. Hwang *et al.* [40] investigated the effect of variation of *TSR* , chord length, number of blades and the shape of hydrofoil on performance of a variable pitch vertical axis water turbine using both experiments and numerical calculations.. Duquette and co-workers [23, 24] performed experiments and 2-D numerical analysis to study the effect of number of blades and solidity on the performance of a horizontal axis wind turbine. Their

analysis concluded that the range of *TSR* for maximum C_p depends strongly on solidity and weakly on the number of blades. This indicates the chord length plays an important role in defining the optimum *TSR* range which leads to maximizing the turbine performance. Mukherji *et al.* [35] performed three-dimensional steady-state CFD to understand the effect of *TSR*, solidity, blade pitch and number of blades on performance of HKTs and reported a strong influence of *TSR* on performance coefficient for various turbine geometries. Further, increase in turbine solidity and blade numbers were reported to maximize the C_p that was observed at lower *TSR*. Batten *et al.* [39] used a coupled actuator disc-RANS based model to predict the performance and loads on a tidal turbine and obtained up to 94% agreement between numerical and experimental velocity variation measured along the centerline of the wake. LES simulations performed by Churchfield *et al.* [38] reported presence of lateral asymmetric wake behind the turbine which was a result of interaction between inlet shear flow and wake rotation. Myers and Bahaj [25-27] experimentally investigated the flow field and wake recovery behind marine current turbines using mesh disk simulators and found that recovery depends on proximity to water surface, sea bed roughness (which governs vertical velocity profile and turbulent kinetic energy of flow) and to a lesser extent on rotor thrust. Neary *et al.*[29] performed experiments on an axial flow hydrokinetic turbine in a large open channel to measure velocity and turbulence quantities behind the turbine using an acoustic Doppler velocimeter and a pulse coherent acoustic Doppler profiler techniques. A flow recovery of 80% was reported at ten diameters downstream the rotor plane. Stallard [83] performed experiments with an array of turbines to investigate turbine interactions and the influence of bounding surfaces (free surface and bed) on wake structure behind tidal turbines.

A large majority of the available literature on HKTs focuses on the hydrodynamics and blade optimization for improving the hydrodynamic performance and does not consider fluid structure interaction analysis. The interaction of fluid flow with the turbine structure is an important aspect of design for HKTs due to a denser working medium. This coupled fluid structure interaction (FSI) problem can be solved traditionally by two different approaches: (a) a monolithic approach in which governing equations for the structure and flow field are solved simultaneously using a single solver; and, (b) a partitioned approach in which two distinct solvers are used to independently solve two sets of governing equations described in §2 [33, 41, 42]. Young [43] performed FSI analysis on carbon fiber composite blades for a marine propeller by combining boundary element and finite element methods, and validated his computational results with experimental studies. Young *et al.*[33] performed a coupled boundary element- finite element (FE) hydro-elastic transient analysis of tidal/ marine current turbines and compared results with tow- tank experiments. He *et al.* [44] performed a hydro-elastic optimization of a composite marine propeller in a non-uniform wake using CFD-FEM coupled analysis. Compared to the initial blade design, the final design with optimized ply angle and stacking sequence was reported to have 70.6% reduction in vibratory loads. Selig and Coverstone-Carroll [45] used a genetic algorithm (GA) for optimizing annual energy production (AEP) and cost of energy of low-lift airfoils for stall regulated wind turbines and found that AEP is more sensitive to rotor radius than the peak power. Belesis [46] presented GA for constrained optimization of stall regulated wind turbine and found it to be superior to classical optimization methods. GA implementation was reported to have 10% gain in the energy production for different sized stall regulated wind turbines. Fuglsang and Madsen [47]

performed multi-disciplinary optimization on stall regulated horizontal axis wind turbine considering fatigue, maximum load and AEP. They used sequential linear programming and method of feasible directions for optimizations. Operating parameters like *TSR*, blade pitch as well as blade geometry were found to have a significant effect on performance as well as structural strength of the turbines.

To the knowledge of the authors, the current work presents the first coupled fluid structure interaction analysis for a hydrokinetic turbine for maximizing its hydrodynamic performance and minimizing hydrodynamic stresses on a stall regulated, fixed pitch, horizontal axis hydrokinetic turbine through a coupled hydro-structural analysis and GA based optimization technique. The analysis is performed for two different blades: a constant chord, zero twist design; and, a variable chord, twisted design. Figure 3. 1 shows a flow chart for the design approach that has been adopted in this paper. As a starting point, a hydrodynamic analysis was carried out using BEM theory to study the effect of various operating parameters on the forces and torque developed on turbine blades for a constant chord turbine. During the preliminary design process when a detailed flow field solution is not available, stresses in the turbine blade are computed based on forces obtained from BEM. The turbine blade was modeled as a cantilever beam fixed at the hub; stresses were calculated based on blade section area. The hydro-structural optimization was carried out for a constant chord blade turbine using GA in a MATLAB optimization toolbox. A Pareto optimal solution set obtained from GA was used as an input to the coupled FSI analysis. To check the fidelity of BEM and the optimized design, the results of lower order BEM model for a constant chord blade design are compared with a detailed three-dimensional coupled CFD-FEA analysis. The CFD domain is coupled with the structural domain using

52

an arbitrary Lagrangian-Eulerian scheme and FEA is performed to find deflection and stresses in the turbine components. The results of structural analysis are then used to modify the turbine geometry and design space for hydro-structural optimization, imposing limits on operating parameters and size. Further, to improve the structural strength of the turbine blade a chord and twist distribution is added to the turbine blade. A multi-objective (hydro-structural) optimization was performed for this variable chord twisted blade geometry to maximize hydrodynamic performance and minimize structural stresses in turbine blade. Higher flow velocities (>3.5m/s) and proximity to water surface were found to cause cavitation on turbine blades [33]. The current analysis assumes a flow speed of 2m/s and that the turbine was submerged sufficiently in water and away from free water surface to provide a cavitation free environment for turbine operation. The HKT design presented in this paper has three blades made from a hydrofoil shape and connected at the turbine hub similar to a typical horizontal axis wind turbine. HKTs are lift-drag devices and operate on a similar working principle as the wind turbines; however, a denser working medium (water which is almost 800 times denser than the air) poses additional challenges as the flow Reynolds number and the associated hydrodynamics for these turbines are different than that for conventional wind turbines. A CFD analysis and validation is performed to address the effect of change of the working fluid (viscosity and density) that affect flow parameters like flow separation and stall delay, which in turn affect the performance. A denser working fluid results in higher power density per unit swept area which induces a higher stress state in the turbine blades. The investigation of this stress field is one of the primary objectives of the current fluid-structure interaction analysis.
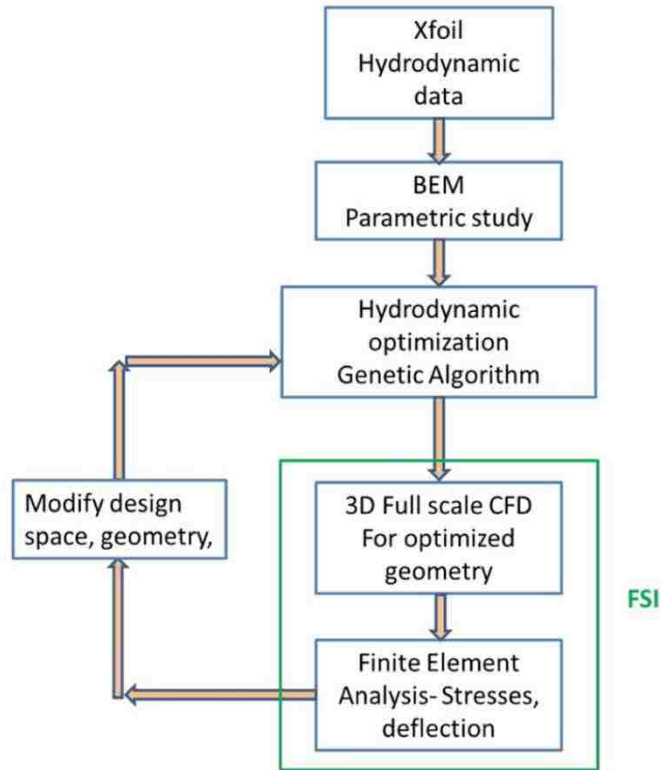
Figure 3.1: Hydro-structural optimization and design method for HKTs.

3.2 THEORY AND MATHEMATICAL MODEL

3.2.1 BEM Theory

BEM theory, originally attributed to Betz [65-67] and Glauert [30] is a combination of blade element theory and momentum theory. According to the blade element theory, forces on a turbine blade can be obtained by dividing the blade into a number of hydrodynamically independent elements [68]. Hydrodynamic forces on these elements are calculated based on local flow conditions using two dimensional lift-drag data. The forces on each element are then summed together to find total force on the turbine blade. The other part of BEM, known as momentum theory, assumes that the work done by the fluid on the turbine blade creates pressure (or momentum) loss across the rotor plane. Induced velocities in axial and tangential direction can be calculated from this momentum loss;

54

which in turn affects the forces on turbine blade. BEM combines blade element and momentum theories, and solves coupled equations in an iterative manner to determine fluid forces (thrust and torque) and induced velocities near the rotor [68]. Aerodynamic data: lift coefficients (C_L) and drag coefficients (C_d) for the SG6043 hydrofoil that were adopted for our HKT blades are obtained from Xfoil [69]. These coefficients were then used to calculate forces on blade element in directions normal and tangential to the rotor plane. Xfoil calculates lift and drag coefficients for a given hydrofoil by combining a linear-vorticity stream function panel method [84] and a viscous solution method. A surface transpiration model is used to couple a viscous solution (for boundary layer and wake) with an incompressible potential flow solution (for the flow domain away from the turbine surface). Hydrodynamic data obtained from Xfoil is corrected according to [23, 24] as:

$$C_d = C_{d,\text{Re}_{\text{Ref}}} \left(\frac{\text{Re}_{\text{Ref}}}{\text{Re}} \right)^{0.2} \qquad (3.1)$$

which suggests that the drag coefficient scales inversely with the Reynolds number. The drag coefficient, C_d in Equation 3.1, is the actual drag coefficient (based on Re), $C_{d,\text{Re}_{\text{Ref}}}$ is the drag coefficient based on Re_{Ref} which is the reference Reynolds number (2.4×10^5) used during BEM analysis. The lift coefficient is assumed to be unchanged with Reynolds number [24]. This correction is valid for a Reynolds number range ($10^5<Re<10^7$) which covers the current operating range ($1\times10^5<Re<5\times10^5$). The Reynolds number reported in the present work is based on the free stream flow speed (U) and the blade mean chord-length (c_m). The Re based on mean chord lengths of 0.05m and 0.25m are ~ 1×10^5 and ~5×10^5 respectively.

For our analysis, the original BEM theory of Betz [65, 66] and Glauert [30] was modified to take into account the effect of hub, tip and the Reynolds number dependence for hydrodynamic data correction. Prandtl's tip loss correction factor (F_{Tip}) was incorporated in the algorithm to account for losses due to fluid flow from pressure side to suction side at blade tip, while the hub loss (F_{Hub}) correction factor was also incorporated to account for losses caused by swirling flow due to presence of hub as:

$$F_{Tip} = \frac{2}{\pi} \cos^{-1}\left(\exp\left(\frac{B(r-R)}{2r\sin(\phi)}\right)\right) \quad ; \quad F_{Hub} = \frac{2}{\pi} \cos^{-1}\left(\exp\left(\frac{B(r_{hub}-r)}{2r_{hub}\sin(\phi)}\right)\right) \tag{3.2}$$

where, r is the radius at the blade element [m], r_{hub} is the hub radius [m], and ϕ is the angle of relative flow [radians].

The effects of correction factors for tip and hub losses are combined into single factor F $(= F_{tip} \times F_{hub})$ that is used to determine net thrust (T) and torque (Q) from turbine:

$$T = \int_{r_{hub}}^{R} F\rho U^2 4a(1-a)\pi r dr \quad ; \quad Q = \int_{r_{hub}}^{R} 4Fa'(1-a)\rho U \pi r^3 \Omega dr \tag{3.3}$$

where, ρ is the water density [kg/m^3]. The axial induction factor (a) is defined as a fractional decrease in water velocity between the free stream and the rotor plane. The angular induction factor (a') is defined as one half the ratio of the angular velocity of the wake to the angular velocity of the rotor $\left(a' = \dfrac{\omega}{2\Omega}\right)$.

Preliminary structural analysis is based on an assumption that the turbine blade can be modeled as a cantilever beam, supported at blade root, and flap-wise bending moment can be found from thrust forces acting on blade. Flap-wise bending stresses in the turbine blade depend on the thrust force, and are determined according to Equation 3.5.

$$M_{\beta} = \frac{1}{B} \int_0^R r\,dT \quad ; \qquad \text{where,} \qquad dT = \left(\frac{1}{2} \rho \pi\, C_T\, U^2\, 2\,r\,dr \right)$$

On integration:

$$M_{\beta} = \frac{2}{3} \frac{T}{B} R \tag{3.4}$$

$$\sigma_{\beta,\max} = \frac{M_{\beta}\, c}{I_b} \tag{3.5}$$

where, I_b is the area moment of inertia of blade cross-section (airfoil shape) [m^4], M_{β} is the flap-wise bending moment [N.m], $\sigma_{\beta,\max}$ the maximum flap-wise stress [N/m^2], and, C_T is the thrust coefficient that was assumed as 8/9 for an ideal rotor [68].

3.2.2 FSI-Governing equations

The FSI problem involves the fluid domain and structural domain interacting with each other at the fluid-structure interface. The load transfer at the interface is done using arbitrary Lagrangian-Eulerian (ALE) formulation [33, 41, 42, 70]. This section briefly summarizes the governing equations for the fluid and structural solvers [70, 85]. The subscript (*f*) denotes quantities related to the fluid domain and the subscript (*s*) denotes structural domain quantities. The fluid-structure interface is the common boundary between the two domains where data the transfer takes place.

3.2.2.1 Computational Fluid Dynamics:

A three-dimensional CFD analysis was performed in ANSYS CFX using a multiple reference frames technique [86, 87]. A rotating reference frame was incorporated to take into account the effect of turbine rotation by transforming an unsteady flow in an inertial (stationary) frame to a steady flow in a non-inertial (moving) frame using equations below [33, 42, 70, 88]:

$$\nabla \cdot \vec{U}_r = 0 \tag{3.6}$$

$$\left[\frac{\partial}{\partial t}(\rho \vec{U}) + \nabla \cdot (\rho \vec{U}_r \vec{U}) + \rho(\vec{\Omega} \times \vec{U}_r + \vec{\Omega} \times \vec{\Omega} \times \vec{r}) \right] = -\nabla p + \nabla \cdot \tau_f$$

(3.7)

where $\vec{U}_r$ $(= \vec{U} - \vec{\Omega} \times \vec{r})$ is the relative velocity viewed from a rotating reference frame, $\vec{\Omega}$ is the rotational speed of the turbine, $\rho(\vec{\Omega} \times \vec{U}_r)$ is the Coriolis force, $\rho(\vec{\Omega} \times \vec{\Omega} \times r)$ is the centrifugal force, τ_f is viscous stress tensor, and ∇p is the pressure gradient across the turbine. The viscous stress tensor (τ_f) is defined as:

$$\tau_f = \mu_{eff} \left[(\nabla \vec{U} + \nabla \vec{U}^T) - \frac{2}{3} \nabla \cdot \vec{U} I \right] \tag{3.8}$$

where U is the absolute fluid velocity and I is the identity tensor. The effective viscosity (μ_{eff}) is the sum of the molecular viscosity (μ) and turbulent viscosity (μ_t); μ_t being calculated from a representative turbulence model. A k-ω SST (Shear Stress Transport) turbulence model was chosen, due to its accuracy, for adverse pressure gradient flows as the current case [19, 89, 90]. The computational domain consists of an inner rotating sub-domain of size $1.1R \times 0.65$, and an outer stationary sub-domain of size $6R \times 22$. Figure 3.2 shows the location of turbine within the computational domain. The turbine rotational plane is located $4R$ away from the inlet, and the fluid domain extends $18R$ behind the turbine rotational plane to capture the near wake and far wake effects. The inlet boundary condition was applied on the east face of the domain with uniform axial (free-stream) velocity (U) of 2m/s with V and $W=0$, and turbulence intensity of 10%. A high resolution (bounded second-order upwind biased) discretization scheme was used for advection and turbulence. The

convergence criteria for RMS residuals were set to 10^{-6} for continuity, momentum and turbulence quantities.
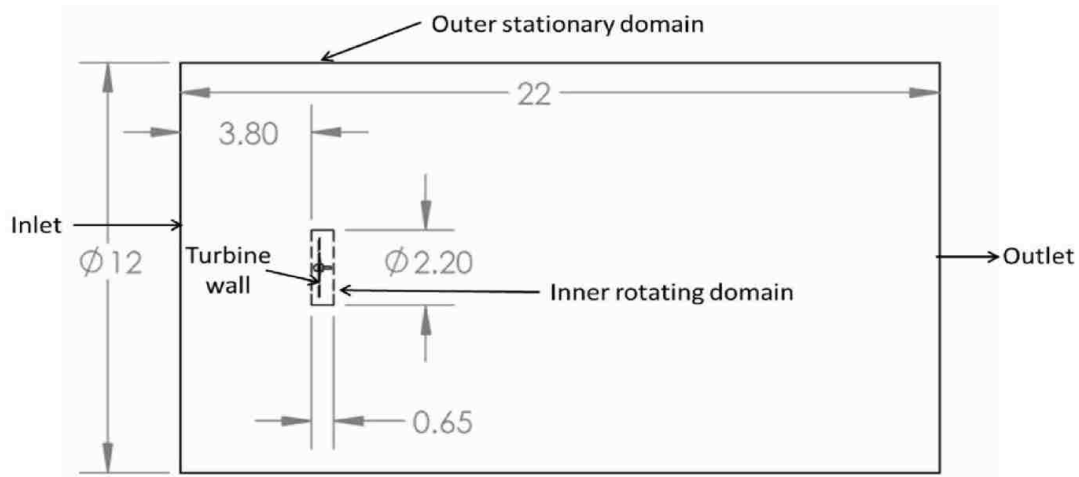
Figure 3.2 : Computation domain, used for CFD analysis (All dimensions are expressed in terms of turbine radius, *R*)

The simulation domain was initialized with the initial velocity of $U = 2$m/s. The CFD simulations presented in this paper are steady state calculations performed using a multiple reference frames technique; details about this technique can be found elsewhere [25]. which was validated and published in [25]. A rotating reference frame was incorporated to take into account the effect of the turbine rotation by transforming an unsteady flow in an inertial (stationary) frame, to a steady flow in a non-inertial (moving) frame using equations 3.6 through 3.8. The CFD study consisted of HKTs rotating at various rotational speeds 40RPM to 135RPM, which corresponds to the *TSR* range of 2 to 7. The mesh used for current CFD study is an unstructured mesh with very fine prism layers near the turbine wall. A grid independence study was carried out to study the effect of the number of elements on the CFD analysis. Mesh size was varied from a coarser mesh of 3.5 million to a finer mesh of 10 million elements and flow variables were monitored. As the mesh size increases, turbine power increases and stabilizes around 7.8 million elements. The percent

change in output power from 7.8 million element grid to the next coarser grid (6.6 million cells) was 1.3%. Hence, a mesh with 7.8 million elements was found optimal from the accuracy and the computational expense standpoint and used for current CFD study. In addition to the global mesh size study, a convergence study on the global converged mesh was performed to understand the effect of $y+$ value on the turbine power and thrust prediction. This study consisted of locally refining the near wall prism layers to reduce the $y+$ value. For the global converged mesh, the thrust and power values started to converge around the $y+$ value of 100. Hence considering the computational expense and accuracy, the final computational grids used during the current CFD study consisted of the meshes with $y+$ value of less than 100 for the converged performance characteristics. The height of the first prism layer on the turbine wall was set such that the grid elements adjacent to the turbine wall were within the logarithmic region of boundary layer with a $y+$ values between 30 and 100. A $y+$ value is a non-dimensional parameter related to mesh size which defines distance of first mesh node from the wall. Lower the $y+$, better the boundary layer flow resolved near the wall [71]. Convergence criteria for the continuity and momentum equations were set to 10^{-6} absolute and higher order numerics were used for turbulence modeling.

3.2.2.2 Structural dynamics equations:

The conservation of momentum equation of a solid continuum in a Lagrangian framework can be expressed as:

$$\rho_s \frac{\partial^2 \delta_s}{\partial t^2} - \nabla . \tau_s = f_s \tag{3.9}$$

where ρ_s represents structural density, f_s represents body force vector per unit volume on the structure, δ_s represents structural displacement field and τ_s is a symmetric Cauchy

60

stress tensor. In the present analysis, the fluid flow equations are solved to find the resultant forces on interface and then stresses are calculated by solving the structural equations. Thus, the kinematic condition for no slip interface can be rewritten as:

$$\delta_f = \delta_s \tag{3.10}$$

where δ_f is the fluid displacement. This forms the displacement boundary condition for fluid-structure interface. The dynamic condition for the fluid-structure interface requires that the fluid and structural stresses be in equilibrium:

$$n_f . \tau_f = -n_s . \tau_s \tag{3.11}$$

where, n is a unit normal vector pointing outward from the respective domains. The Dirichlet-Neumann formulation of FSI presented in equations 3.10 and 3.11 implies that the fluid flow equations are solved for the fluid-structure interface velocity, and stresses are imposed on fluid structure boundary of solid domain [33, 42, 70]. Figure 3.3 shows the mesh used for FEA which consists of around 1×10^5 elements.

Figure 3.3: Finite Element mesh used for structural solver.

In an effort to understand the effect of blade root section on the turbine stresses, two different blade geometries were modeled (Figure 3.4). The main difference in these geometries is at the root section where the blade mates with turbine hub; this section is circular for geometry-I (Figure 3.4a) while it is parabolic for geometry-II (Figure 3.4b).

61
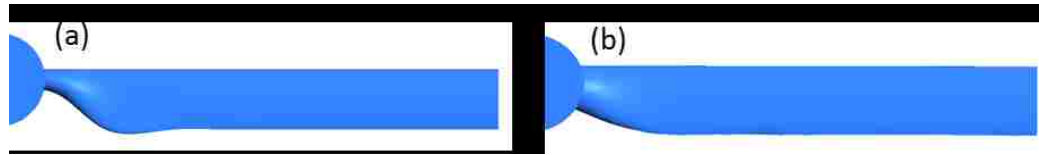
Figure 3.4: Blade shapes used for FSI analysis: (a) circular blade root, (b) parabolic blade root

3.3 RESULTS

3.3.1 BEM Validation

The BEM code was validated with NREL phase III combined experimental rotor (CER) results [91], primarily due to absence of detailed experimental data for HKTs. The NREL CER rotor is a 5.03m radius stall regulated downwind turbine with a rated power of 20kW that has varying chord and twisted blades. This turbine uses S809 airfoil from blade root to tip with a chord and twist distribution along blade span [91]. Experimental data is available [91] for two and three bladed turbine configurations, at constant rotational speeds of 72 and 83 RPM at various blade pitch angles. A BEM analysis was carried out for a rotational speed of 72 RPM for the three bladed turbine over a range of blade pitch angles (0 to 7°) and *TSR* (0 to 8). Figure 3.5 compares C_p from BEM analysis with the NREL data, which shows a good match up to *TSR* of 5. At high *TSR* values, BEM analysis deviates from the experimental data which can be attributed to a non-uniform blade loading [92] and accelerated span-wise flow effects that are not taken into account in one-dimensional momentum analysis. The BEM analysis does not consider the hydrodynamic interaction between the adjacent blade elements. Further, a large out of plane deflections at higher *TSR* introduces errors in hydrodynamics modelling as BEM, which essentially assumes that the momentum is balanced in a plane parallel to the rotor.
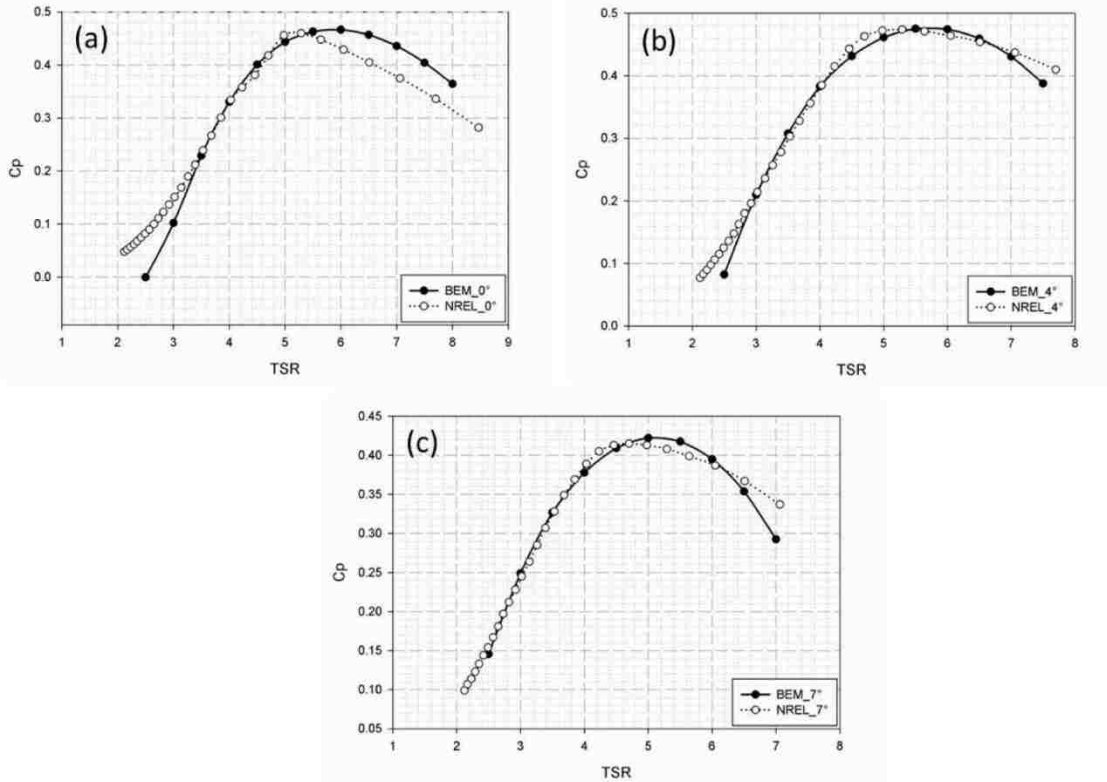
Figure 3.5: Validation of BEM with NREL experiments: a) 0° blade pitch, (b) 4° blade pitch, (c) 7° blade pitch

Figure 3.6a and 3.6b compares the axial induction factors (*a*) along the blade span at 6.7m/s and 11.2m/s wind speeds respectively. The BEM analysis results follow a similar trend as the NREL experimental results, but in general, the axial induction factors computed from BEM are smaller than those obtained from the experimental data. Figure 3.6c plots the thrust forces exerted on a turbine blade as a function of wind speed. The results of BEM are comparable with the experimental data till wind speed of 14m/s, but at higher speeds, 1D BEM analysis deviates from the experimental data due to high flap-wise loading and out of plane deformation which cannot be captured accurately by the momentum theory of BEM method.
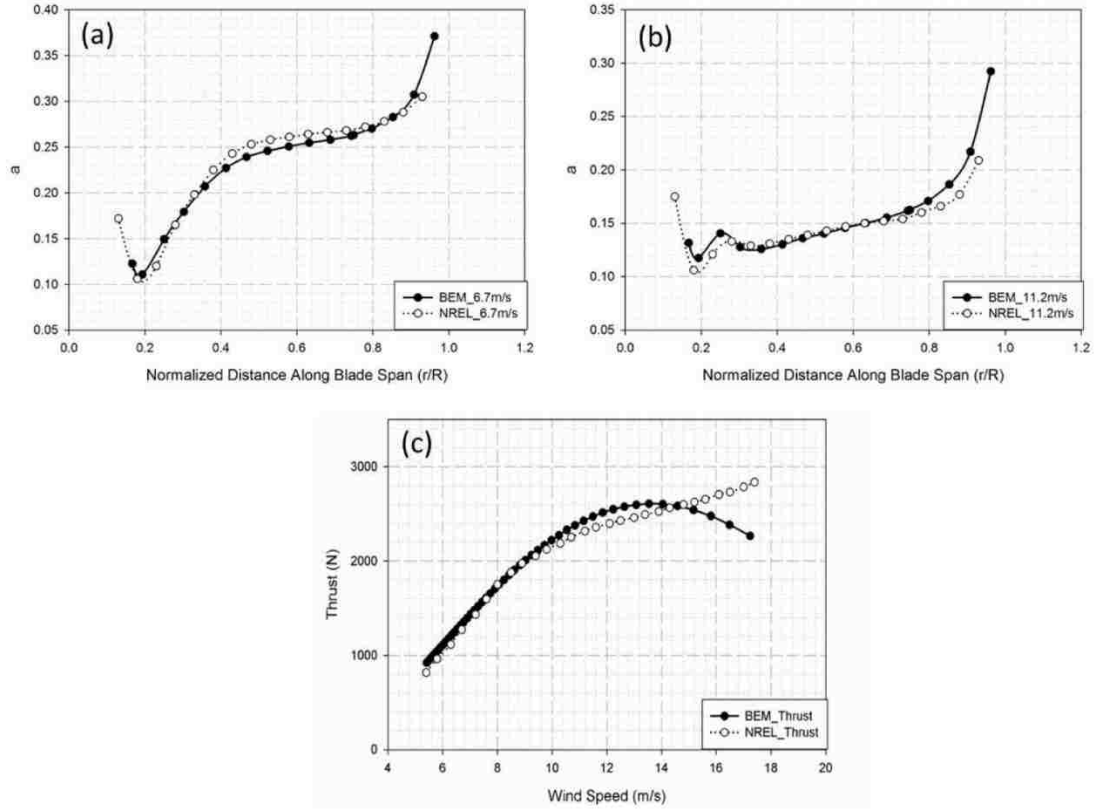
Figure 3.6: Comparison of BEM analysis with NREL experimental data: a) Axial induction factor for U=6.7m/s, b) Axial induction factor for U=11.2m/s, (c) Thrust forces

3.3.2 Analysis for a constant chord zero twist blade turbine

3.3.2.1 BEM parametric study

After validating the mathematical model, a parametric study based on the BEM theory with the necessary corrections (Prandtl's tip loss correction, hub loss correction, corrections for the Reynolds number effect on hydrodynamic data) was performed for a model three-bladed constant chord turbine (R=1m). A SG6043 profile was chosen from root to tip as it gives a high C_L /C_d value over the current operating range of the Reynolds numbers (1×10^5<Re<5×10^5). Table 3.1 summarizes various parameters studied during the current analysis. The BEM analysis is performed to understand the effect of chord length, blade pitch (θ_{po}) and *TSR* on the performance of the turbine. The turbine blade was divided

into 20 blade elements and the BEM analysis was performed to find the thrust forces and the torque developed on the turbine blades according to Equation 3.3.

Table 3.1: Design variables for BEM parametric study of Hydrokinetic Turbines

Design Variable	Value/Range
Number of blades (B)	3
Turbine radius (R)	1 m
Hub radius (r_{hub})	0.085 m
Number of blade elements (N)	20
Water velocity (U)	2 m/s
TSR	2-12
Chord length (c)	0.015-0.18 m
Blade pitch angle (θ_{po})	0-18°

The water velocity used for this analysis was 2 m/s which is the upper limit of observed river water velocity for large sinuous canaliform rivers like the Mississippi and Missouri rivers [93]. The design *TSR* is varied from 2 to 12, blade pitch angle from 0° to 18° and chord length from 0.015 to 0.18m. Figure 3.7 shows the effect of blade pitch, *TSR* and chord on the performance coefficient. As the chord length is increased from 0.03 to 0.12m as plotted in Figures 3.7a-c; the bell shaped curve of C_p plotted against *TSR* moves towards the origin, which indicates that higher the chord length, the lower the *TSR* for optimum performance. Also, for a given chord length, the lower the *TSR*, the higher the blade pitch for maximum performance. A higher θ_{po} means higher angle of attack of incoming fluid which results in higher lift forces (hence torque) on turbine blades. This results in lower rotational speeds and hence lower *TSR*s for optimum hydrodynamic performance with
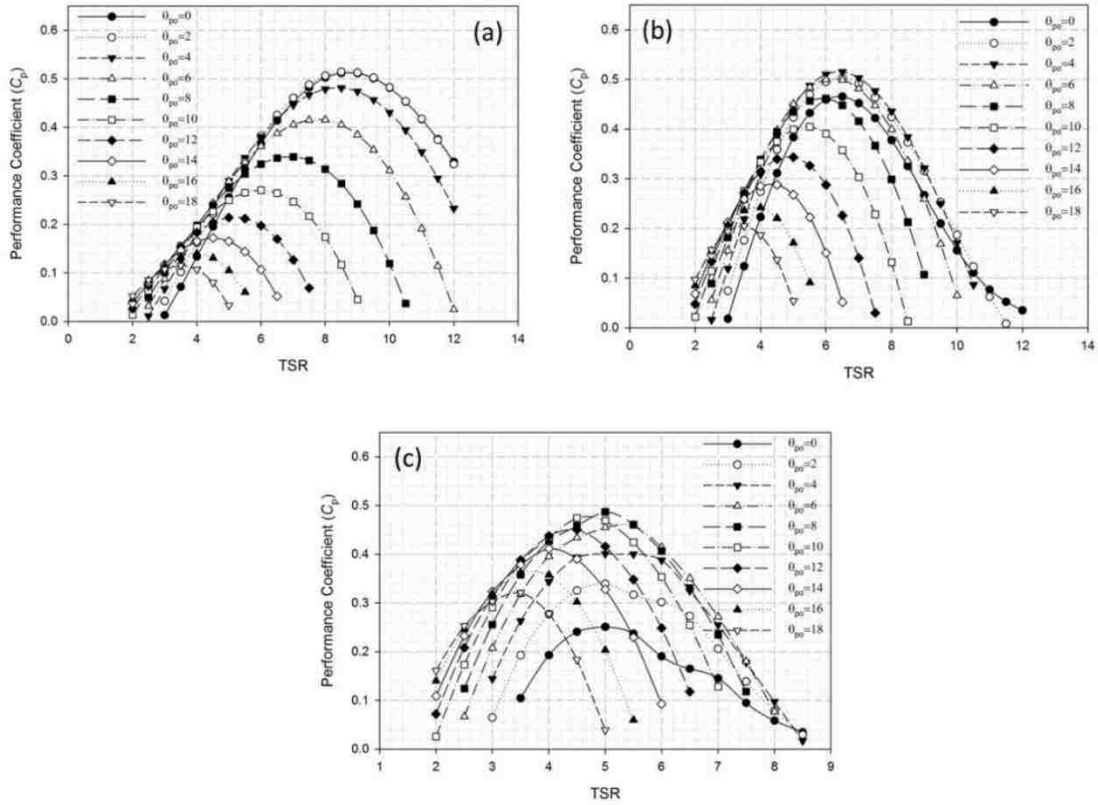
Figure 3.7: Effect of TSR and blade pitch angle on turbine performance at various chord lengths: (a) 0.03m chord, (b) 0.06m chord, and (c) 0.12m chord

increasing θ_{po} values. For higher chord length blades (0.06m and 0.12m), an increase in θ_{po} results in higher C_p till a critical θ_{po} is reached for corresponding chord lengths. For c =0.06m chord blade, maximum C_p is observed at $\theta_{po} = 4°$ (*TSR* =6.5), and for c =0.12m, maximum C_p is observed at $\theta_{po} = 8°$ (*TSR* =5) (Figure 3.7). This can be attributed to higher lift forces acting on blade surface with increasing angle of attack till it reaches a stall angle after which a reduced performance is observed. For the low solidity blade (c=0.03m), maximum performance was observed at θ_{po} =0°, and *TSR* =8.7. An increase in θ_{po} resulted in lowering the *TSR* for maximum C_p similar to 0.06m and 0.12m chord blades, but this was accompanied by a reduction in maximum achievable C_p as well. Thus, for a low

solidity blade, an increase in angle of attack did not produce higher power but only resulted in lowering the operational *TSR* range.

Figure 3.8 shows the effect of chord length, *TSR* and blade pitch on stresses developed in turbine blades. This analysis assumes blades to be fixed at the rotor hub as cantilever beams and stresses are computed based on the thrust force exerted on rotating blades due to flowing fluid. From Figure 3.8, it is evident that the chord length and hence blade thickness has a significant role in reducing the stresses and improving the strength of the turbine blades. For a given chord length, stresses in a turbine blade depends not only on the total thrust force, but also its distribution along the blade span. Such a distribution is a function of blade *TSR*, pitch angle, blade airfoil and blade root geometry. As expected, the stresses are higher at higher *TSR* and lower pitch angle values due to higher rotational speeds (high *TSR*s) and higher drag forces due to larger projected blade area exposed to flow (low blade pitch angles). For a chord length of 0.03m, the stresses in turbine blade continue to increase with *TSR* for all blade pitch angles. Due to a smaller chord length (hence thinner blade), the flap-wise bending stresses are very high for all *TSR* values, thus making this design structurally unsafe. As the chord length increases from 0.03m to 0.06m and 0.12m, the turbine blade becomes structurally more stable. At these higher chord lengths, with increasing *TSR*, stresses first increase and then decrease after a critical *TSR* for each blade pitch angle is reached. Moreover, it was observed that the blade pitch angle for maximum stress is different for different chord-lengths: for c =0.03m, the maximum stress was observed at θ_{po} = 14°, for c =0.06m at θ_{po} = 4° and for c =0.12m at θ_{po} = 6°. This illustrates the complex nature of stress and its dependence on *TSR* and c, and θ_{po}. Our parametric study, based solely on the hydrodynamic analysis, suggests that, lower values
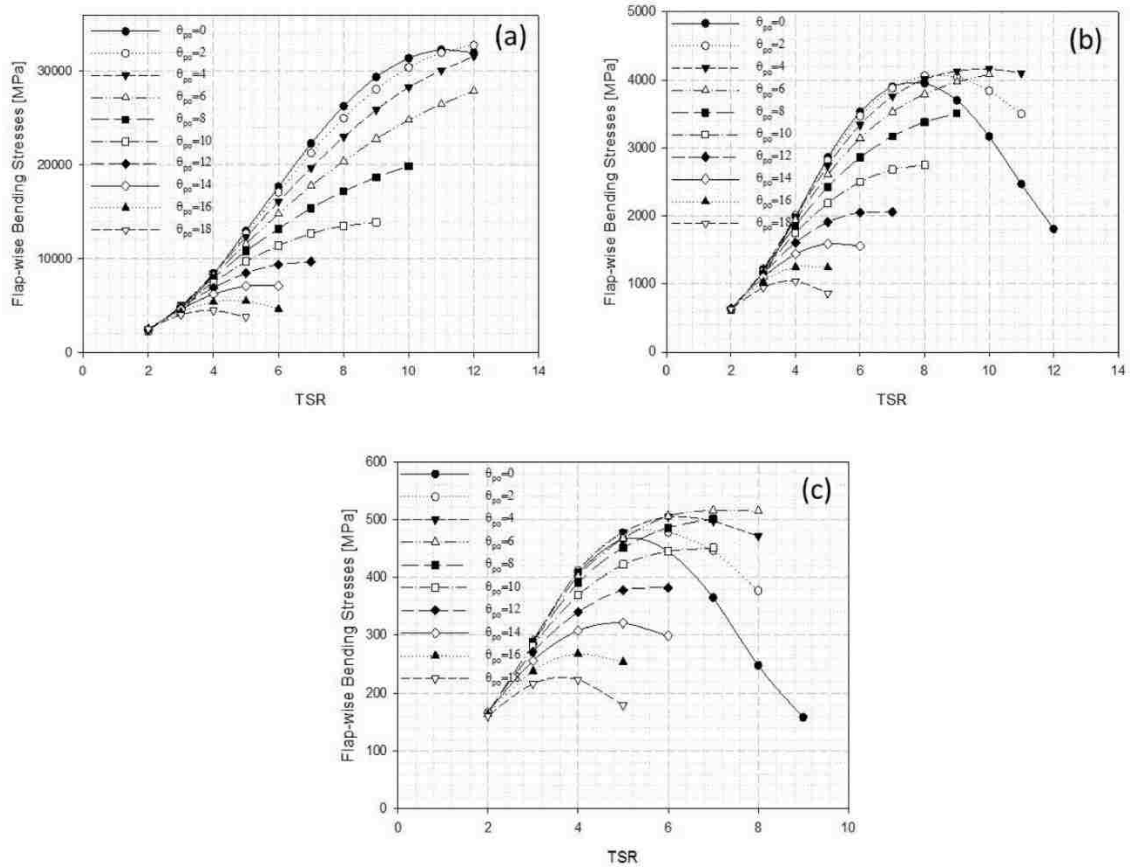
Figure 3.8: Effect of design variables on flap-wise bending stresses: (a) 0.03m chord, (b) 0.06m chord, and (c) 0.12m chord

of blade pitch angles and chord lengths maximize the coefficient of performance, while the structural analysis suggests that higher blade pitch angles and lower *TSR* are required for the structural stability of turbine. A trade-off between efficiency and structural strength is thus important for an efficient HKTs design that was achieved using multi-objective optimization with GA. The results from parametric study were used to specify bounds on the chord length, *TSR* and blade pitch angle for optimization.

3.3.2.2 Multi-objective Optimization: Genetic Algorithm

GA is a heuristic search and optimization technique which converges to a global minimum by searching over a population of possible solutions. Unlike traditional

optimization methods like gradient search and simplex methods, GA requires information about fitness function only and not its derivatives [94]. Figure 3.9 illustrates a flow diagram of the procedure adopted in this work. GA is based on a natural selection process that mimics biological evolution and iteratively modifies a population of individual solutions [95, 96]. Individuals from the current population are used as parents to produce the children for the next generation. Over successive generations, the population *evolves* toward an optimal solution. The output from GA is a set of multiple possible solutions (Pareto optimal solution set), so designer has a choice to choose the best feasible solution as per his requirements. A multi-objective optimization was developed using MATLAB. The problem consists of finding a set of decision variables: blade pitch, *TSR* and chord length which optimizes C_p and thrust forces. The objective function $F(x)$ is defined as:

$$F(x) = \left[f_1(x), f_2(x) \right]$$

where $f_1(x) = - C_p(\theta_{po}, TSR, c), \quad f_2(x) = + T(\theta_{po}, TSR, c)$ \hfill (3.12)

GA algorithm is designed to minimize both $f_1(x)$ and $f_2(x)$; the negative sign on C_p and positive sign on T ensure that both hydrodynamic and structural performances are maximized. The design space selected for the current study is such that the *TSR* is varied from [2, 6], blade pitch angle from [8°, 16°] and chord length from [0.08m, 0.18m]. The experience gained from a wind turbine literature is used to specify the *TSR* range for the parametric study [92, 97]. For a wind turbine, which is a lift-drag device similar to HKTs, the *TSR* for maximum C_p ranges from [6, 10]. For HKTs, the average river water speed is ~2 m/s, while the average rated operating wind speed for wind turbine is ~13m/s. Since water is almost 800 times denser than air, HKTs should be designed and optimized such that the operational range of *TSR* is below that of the conventional wind powered machines.
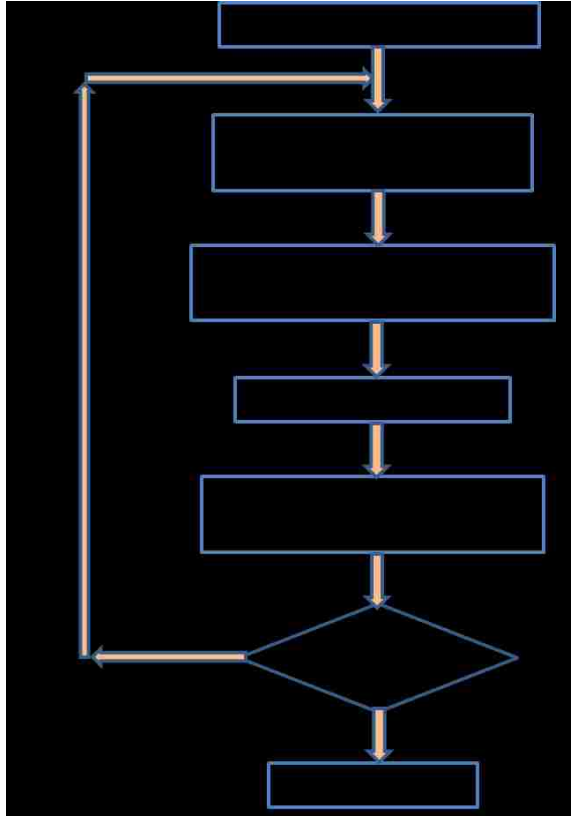
Figure 3.9: Flowchart for Genetic Algorithm based Multi-objective Optimization

Hence, the design the *TSR* space for this study is chosen as [2, 6]. The SG6043 hydrofoil used for the current study has a stall angle around 14°-16° over the operational range of flow Reynolds number ($1\times10^5 < Re < 5\times10^5$). Hence, a pitch angle range of [8°, 16°] is expected to cover all possible optimal operating blade pitch angles for optimizing C_p. The maximum chord length was restricted to 0.18 m which corresponds to R/c of 0.56 ($\sigma = 0.086$). The higher the chord length, the larger the blade area undergoing thrust loading, and the higher the inertia, which is detrimental to the turbine life. Further, an increase in chord length does not improve the performance significantly, but only lowers the *TSR* for maximum performance [24, 35]. The results of GA optimization are shown in Figure 3.10 which plots a Pareto curve obtained from GA algorithm.
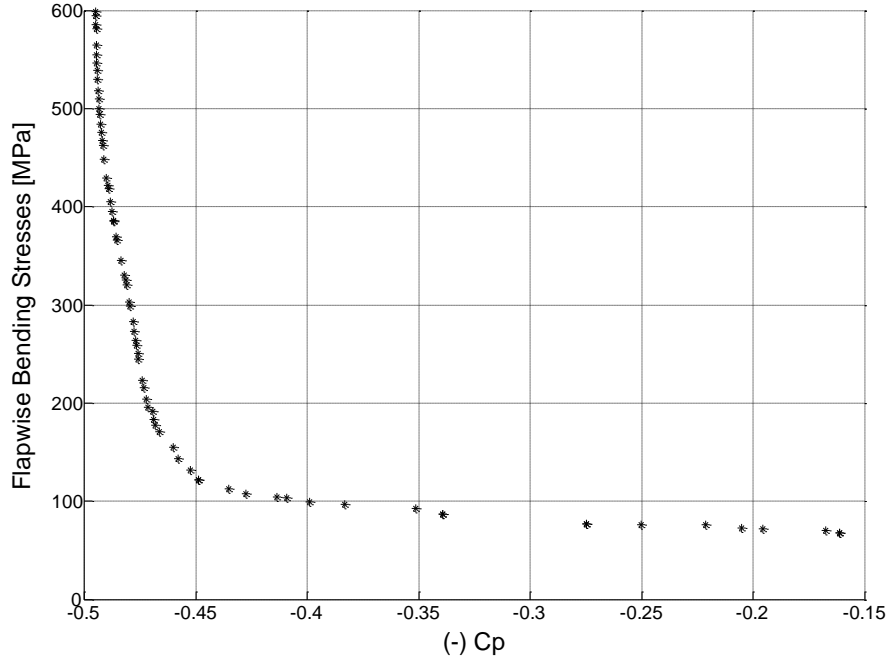
Figure 3.10: Pareto optimal curve from GA multi-objective optimization

The multi-objective optimization based on GA algorithm minimizes the structural stresses and a negative value of C_p as defined in our objective function. Each point on this curve represents a feasible optimized solution ($-C_p$, stress) with optimal design variables (chord-length, *TSR* and blade pitch angle). It was observed that, the higher the C_p, the higher the stresses, hence, a higher C_p can be attained for stronger blade material with high allowable stresses. Table 3.2 presents sample solutions from Pareto optimal solutions space. The stresses presented in Table 3.2 are flap-wise bending stresses in turbine blades, calculated based on thrust forces and blade size at the root and determined according to Equation 3.5. Incorporation of this simple analytical form for stresses in BEM analysis, made it possible to perform a multi-objective optimization analysis. The turbine performance improves with increasing *TSR* and decreasing chord-length, but at the cost of higher stresses. With increasing *TSR*, a decrease in blade pitch angle was observed for maximum performance which is consistent with BEM parametric study. A detailed coupled CFD-FEA analysis

71

was performed later to validate the results of optimization and check the fidelity of our lower order BEM technique and is described in next subsection.

Table 3.2: Optimal solutions obtained from GA multi-objective optimization for a constant chord blade

Sr. #	Blade Pitch (°)	*TSR*	Chord (m)	*Cp*	Stress (MPa)
1	14.32	3.48	0.18	0.44	108
2	12.57	4.22	0.18	0.45	129
3	11.69	4.4	0.17	0.46	145
4	10.39	3.72	0.16	0.47	177
5	10.33	4.58	0.15	0.47	210
6	10.18	4.61	0.15	0.48	243
7	9.58	4.76	0.14	0.48	276
8	9.15	4.78	0.14	0.48	300

3.3.2.3 FSI analysis

A fluid structure interaction analysis is carried out using a partitioned one-way coupling. CFD analysis was performed in ANSYS CFX, where fluid domain equations were solved in a rotating reference frame technique to find torque and thrust forces on turbine blades. The fluid solver is coupled with the structural solver and fluid forces obtained from CFD are then transferred to the structural domain at fluid structure interface. Finite element analysis was carried out in ANSYS Mechanical. Figure 3.3 shows the mesh used for FEA which consists of around 1×10^5 elements. More than 99.5% of nodes were mapped at the fluid structure interface for all cases. The blade material used for FE analysis was a structural steel with density (ρ_s)=7850kg/m^3 ; Yield strength (σ_{yt})=280MPa and Ultimate strength (σ_{ut})=460MPa.

Table 3.3 compares the results of CFD analysis to forces and Cp obtained from BEM calculations. The data is presented for 10°, 10.39°, 12°, 13.5° and 14.4° blade pitch angle cases at different *TSR* and chord lengths, which are Pareto optimal solutions from GA.

Table 3.3: Summary of FSI and BEM analysis

Geo met ry	Variables			CFD		FEA				BEM		
	θ_{po} (°)	c (m)	*TSR*	Cp	T (N)	σ_y (Mpa)	σ_v (Mpa)	δ_y (cm)	µstrain	Cp	Thrust (N)	σ_y (Mpa)
I	10	0.12	4	0.45	4753	282	364	4.7	1890	0.42	4832	372
I	10	0.12	3	0.36	3835	240	312	3.9	1616	0.29	3613	278
I	12	0.12	4	0.42	4241	298	340	4.5	1762	0.43	4403	339
II	10.39	0.16	3.72	0.47	5449	215	210	2.4	1050	0.4	5211	179
II	10.39	0.16	4.56	0.46	5678	209	208	2.3	1046	0.47	5823	189
II	13.5	0.14	3.12	0.35	3627	253	332	2.5	1663	0.36	3881	188
II	14.4	0.14	3.52	0.38	3817	263	345	2.7	1725	0.39	4121	200
III	10.39	0.16	3.72	0.47	5254	196	200	1.7	1009	0.4	5211	179

where, σ_y = flap-wise bending stresses, σ_v = von-Mises Stress, δ_y = streamwise deflection

The coefficient of performance and force values obtained from CFD analysis are comparable to those obtained from BEM analysis. It was found that even though the torque and thrust forces from BEM analysis were in agreement with our CFD analysis, stress values deviate from those determined with detailed FEA. The pressure field on the turbine blades (and hence the stress field) is complex due to combination of thrust, centrifugal and Coriolis forces acting on the blades. These forces were not precisely addressed in a BEM based theory. The stresses in turbine blades depend not only on the magnitude of thrust forces on the blade but also on its distribution along the blade span, and CFD analysis determines the detailed pressure/force field on blades. This distribution along the spanwise direction is transferred to the structural solver for stress calculations as opposed to thrust forces calculated on distributed blade elements in BEM analysis. Table 3.3 compares the

stresses obtained from FEA with those from BEM analysis. For c=0.12 and θ_{po}=10°, increase in the *TSR* from 3 to 4 results in increased C_p at the cost of higher stresses. For higher chord length (c=0.16m), the *TSR* was observed not to have a significant effect on C_p. With increased *TSR*, though the thrust force on blade increases, the thicker blade section results in lower stress values which can be seen in Table 3.3. Comparison of case 1 to case 3 in Table 3.3 shows that an increase in θ_{po} from 10° to 12° for the same *TSR* and c values resulted in reduction in performance coefficient with almost similar stress values. Figure 3.11 plots thrust and torque distribution over the blade span obtained from BEM and CFD analysis for a 10.39° pitch, 3.72 *TSR* and 0.16m chord blade turbine case. For the near tip and near hub region, the BEM analysis deviates from CFD results as it does not take into account the effects of three dimensional flow and vortices formed at these regions. Furthermore, this corresponds to a deviation in stress predicted from BEM compared to FSI analysis. It should be noted that the stresses determined from BEM are based on area moment of inertia of blade hydrofoil cross-section near blade root, and does not take into account the effect of the geometry of the blade, particularly at the blade root where blade cross-section changes form airfoil to a circular shape (Figure 3.4).
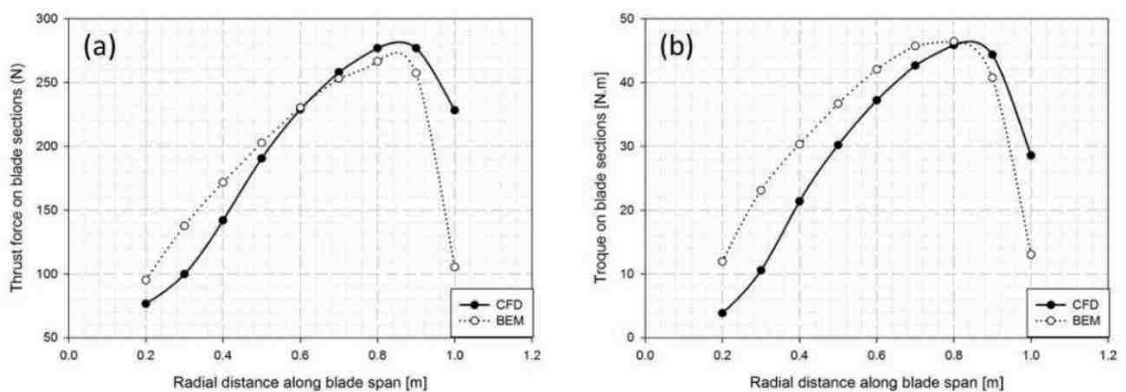
Figure 3.11: Comparison of BEM with CFD for 10.39° pitch, 3.72TSR and 0.16m chord blade HKT (a) Thrust force and (b) torque distribution along the blade span.

The results from CFD analysis for similar turbines operating under same operating conditions but different blade root sections supports this hypothesis. Figure 3.4a shows the blade geometry-I used for cases 1-3 in Table 3.3; and for all other cases 4-8, geometry-II similar to Figure 3.4b was used. The main difference in the geometry is at the root section where the blade mates with the turbine hub; this section is circular for geometry-I while it is parabolic for geometry-II. The parabolic section of geometry II was found to be structurally stronger than the circular cross-section of geometry-I resulting in lower flap-wise stresses when compared to stresses obtained from BEM. It was also observed that maximum von-Mises stress occurs at the transition region where the blade cross-section changes from airfoil to parabolic/circular. Figure 3.12a shows the von-Mises stress distribution on the turbine for case 4 (θ_{po}=10.39°, c=0.16m, TSR =3.72) in Table 3.3 which clearly shows maximum stress of 211MPa in the transition region. Figure 3.12b-d shows span-wise distribution of von-Mises stresses on the pressure side of the blade at 25%, 50% and 75% of chord measured from trailing edge, where maximum stress is observed near the leading edge side of blade. Table 3.3 also summarizes strains and deflection of the turbine blades at various optimal operating conditions obtained from GA optimization analysis. Coefficient of performance as high as 0.47 can be obtained with stream-wise blade deflection of 2.4cm (2.4% of R) and 1050 microstrains (cases 4 and 5 in Table 3.3). Case# 8 illustrates the effect of the size of the blade root section on the induced stresses in turbine blade. The operating conditions and blade geometry of case 8 (geometry-III) were exactly similar to case 4, but the minor diameter in the transition region was increased by 20% which resulted in 5% reduction in stresses without affecting the hydrodynamic performance of the turbine.
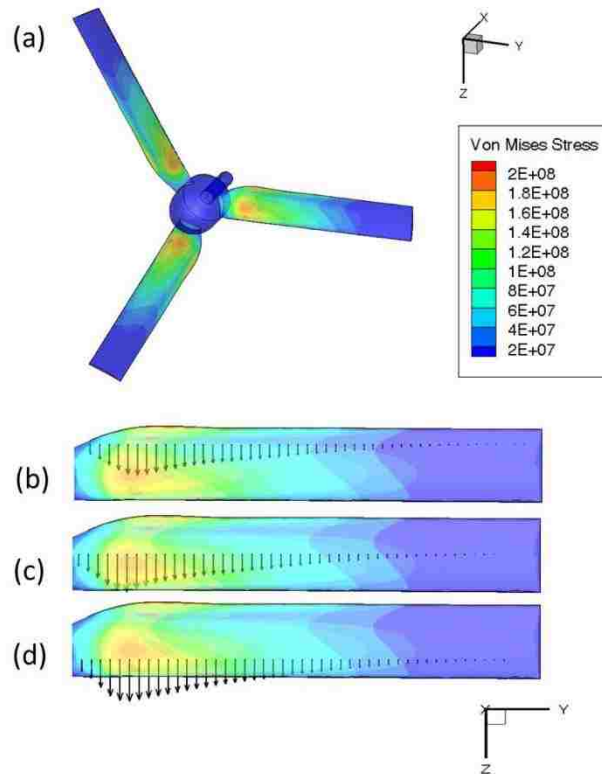
Figure 3.12: von-Mises stress distribution for 10.39° pitch, 3.72*TSR* and 0.16m chord blades HKT: (a) Contour plots of von-Mises stress on complete turbine; Vectors of von-Mises stress at (b) 25% chord, (c) 50% chord, and, (d) 75% chord, all measured from trailing edge

Figure 3.13 plots the streamlines of velocity in a stationary reference frame on the upwind and downwind side of the turbine blade (for case#4 in Table 3.3) which shows a swirling effect near the hub responsible for hub loss effect. Further the suction side of the blade shows the presence of a laminar separation bubble and flow reattachment. This was due to the fact which SG6043 hydrofoil that was used for current analysis exhibits a laminar separation bubble formation at a Reynolds number of $\sim 1 \times 10^5$ [23, 67, 98].
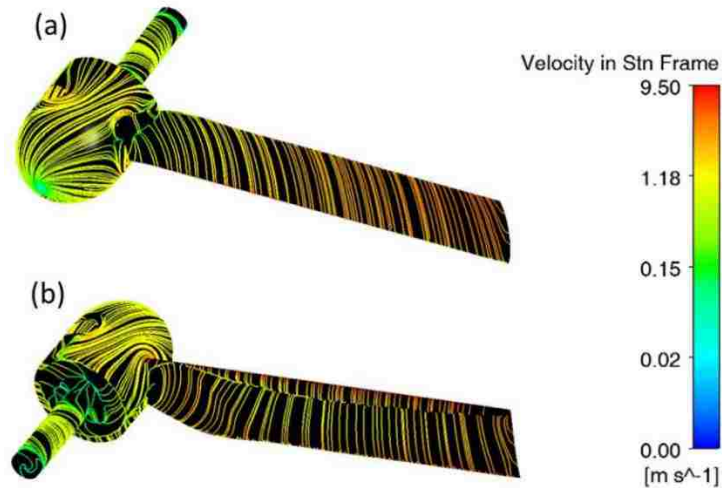
Figure 3.13: Streamlines of velocity in stationary reference frame on (a) upwind side and (b) downwind side of the turbine blade

The operating Reynolds number for this case (case#4 in Table 3.3) is $\sim 3\times10^5$, which is higher than the laminar separation bubble, Reynolds number for SG6043. The flow reattachment behind the laminar separation bubble, and finally, turbulent separation occurs at this high Reynolds number. This results in a delayed separation to higher stall angles and increased lift forces on turbine blades. The effects of these phenomena on the turbine performance and loading were not addressed in BEM analysis, but precisely captured in three-dimensional CFD analysis. Figure 3.14 plots contours of total pressure in a stationary frame of reference at various span-wise locations (0.2R, 0.45R, 0.75R and 0.99R) which shows variation of angle of attack along the blade span, highest being near the blade root (Figure 3.14a), and decreasing progressively towards blade tip (Figure 3.14d). This angle of attack is indicative of lift and drag forces generated by the blade at various sections and can be used as an effective tool for defining blade twist along the blade span to maximize turbine performance and reduce structural loads.

77
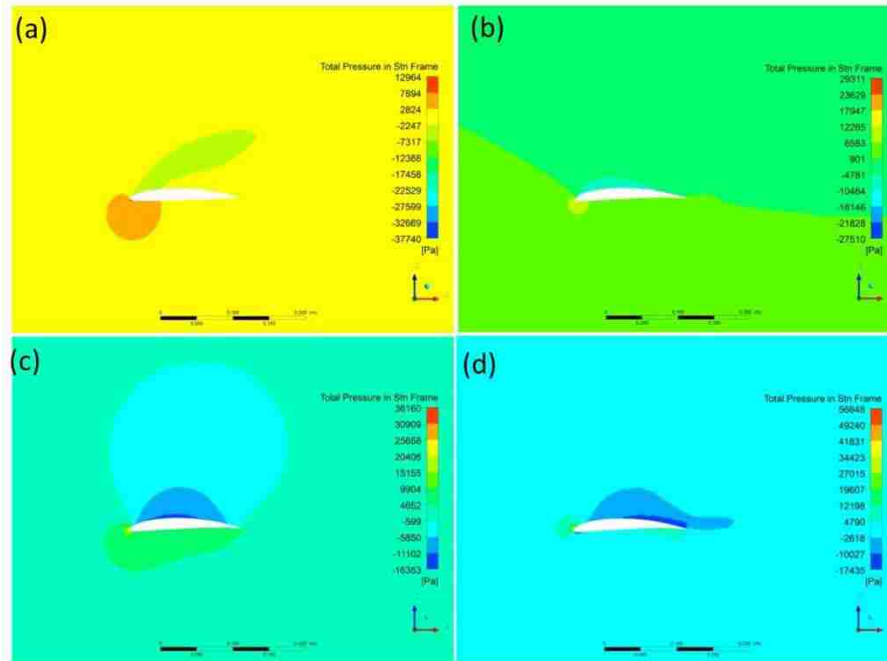
Figure 3.14: Contours of total pressure in stationary frame on planes at (a) 0.2R, (b) 0.45R, (c) 0.75R, (d) 0.99R blade span

Figure 3.15 shows contours of non-dimensional total pressure ($P_{\text{total}}/\rho U^2$) in a stationary reference frame on upwind and downwind side of the turbine blade. The part of the turbine blade near the tip experiences higher non-dimensional total pressure on the pressure side of the blade and lower non-dimensional total pressure on the suction side of the blade compared to the rest of the blade.
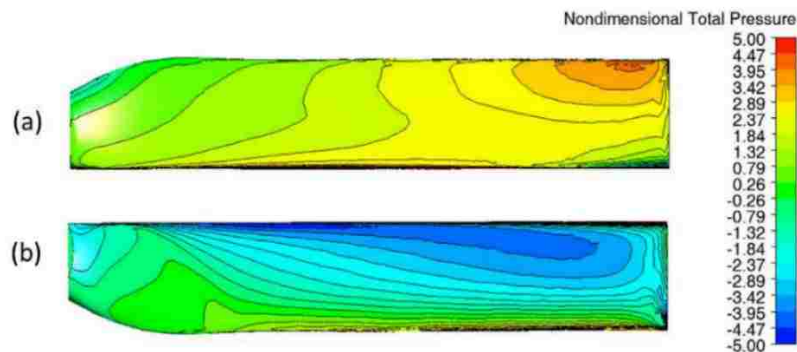
Figure 3.15: Contours of non-dimensional total pressure $P_{Total}\big/\rho U^2$ in stationary reference frame on (a) Upwind side and (b) Downwind side of the turbine blade

A higher ΔP across the blade section is indicative of higher structural loading. This uneven loading not only reduces the turbine performance, but is also detrimental to the turbine life. To reduce the structural loading on the turbine blade and achieve more uniform loading, a multi-objective optimization was carried out by applying twist and chord distribution to the blade geometry, and is discussed next.

3.3.3 Analysis for a Varying Chord and Twisted Blade Turbine

3.3.3.1 Hydrodynamic optimization and parametric study

Higher stress values were observed near the blade root section for an optimized constant chord blade turbine. In addition, CFD analysis for optimized constant chord design indicated a possibility of improvement in hydrodynamic and structural performance of turbine. Hydrodynamic optimization was thus carried out to study the effect of chord and twist distribution on the turbine performance. The optimization was performed considering the effect of wake rotation for different design (rotational) speeds [99]. The design speeds chosen for this analysis were 75RPM (Design_N75), 100RPM (Design_N100) and 125RPM (Design_N125) which corresponds to a design *TSR* of 3.93, 5.24 and 6.55 respectively. All these designs assume a water velocity of 2 m/s and a design blade pitch angle (θ_{po}) of 0°. Figure 3.16a shows the chord length variation along the blade span. For all three designs, the chord length is higher near the hub and progressively decreases towards the blade tip. Figure 3.16b compares the twist distribution along the blade span for all three designs.
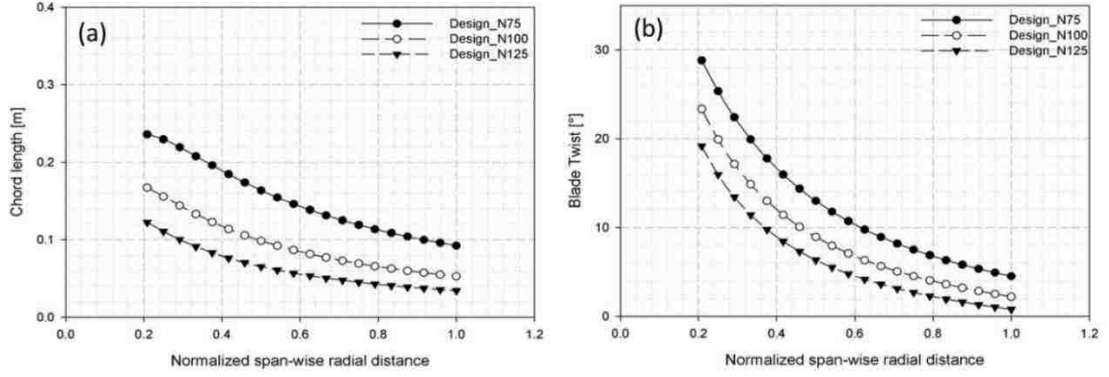
Figure 3.16: Comparison of various blade designs showing (a) chord distribution, and (b) twist distribution along blade span

For optimum performance, the blade twist (θ_t) at any blade section depends on local tip speed ratio (*TSR- λ*), which in turn depends on the design tip speed ratio (*TSR- λ_d*), and radial distance (*r*) of the blade element from the axis of rotation. The design for faster rotating turbine (Design_N125) has lower twist angles and smaller chord length along the blade span compared to other designs, due to a lower angle of relative wind. Equations 3.13-15 illustrate the dependence of ϕ and θ_t on λ_d, r, *R*, the blade pitch angle and the angle of attack (α).

$$\lambda_d = \frac{R\Omega}{U} \; ; \qquad \lambda = \frac{r}{R}\lambda_d \qquad (3.13)$$

$$\theta_t = \tan^{-1}\left(\frac{2}{3\lambda_r}\right) \qquad (3.14)$$

$$\phi = \theta_{po} + \theta_t + \alpha \qquad (3.15)$$

Figure 3.17a shows the effect of *TSR* on C_p at various blade pitch angles for Design_N75. This blade was designed for rotational speed of 75 rpm (*TSR* =3.93), blade pitch angle of 0°, and attains maximum performance of 0.54 at these design values. A reduction in performance is observed with increasing blade pitch angles. Further,

80

increasing a blade pitch angle reduces the *TSR* for maximum performance. Figure 3.17b

plots C_p against *TSR* for various blade pitch angles of Design_N100. This blade is designed

for RPM of 100 (*TSR* =5.24) and blade pitch angle of 0°, and gives C_p of 0.56 at these

design conditions. Similar to Design_N75, this blade configuration also shows reduction

in performance as the blade pitch deviates from the design value of 0°. Figure 3.17c shows

the effect of *TSR* and blade pitch angle on C_p of design for 125RPM. A reduction in

performance is observed as we move away from design RPM of 125 (*TSR* =6.55) and blade

pitch of 0°. The Design_N125 was observed to be less susceptible to the variation in design

values, and performs better over a wider range of *TSR* and blade pitch angles.
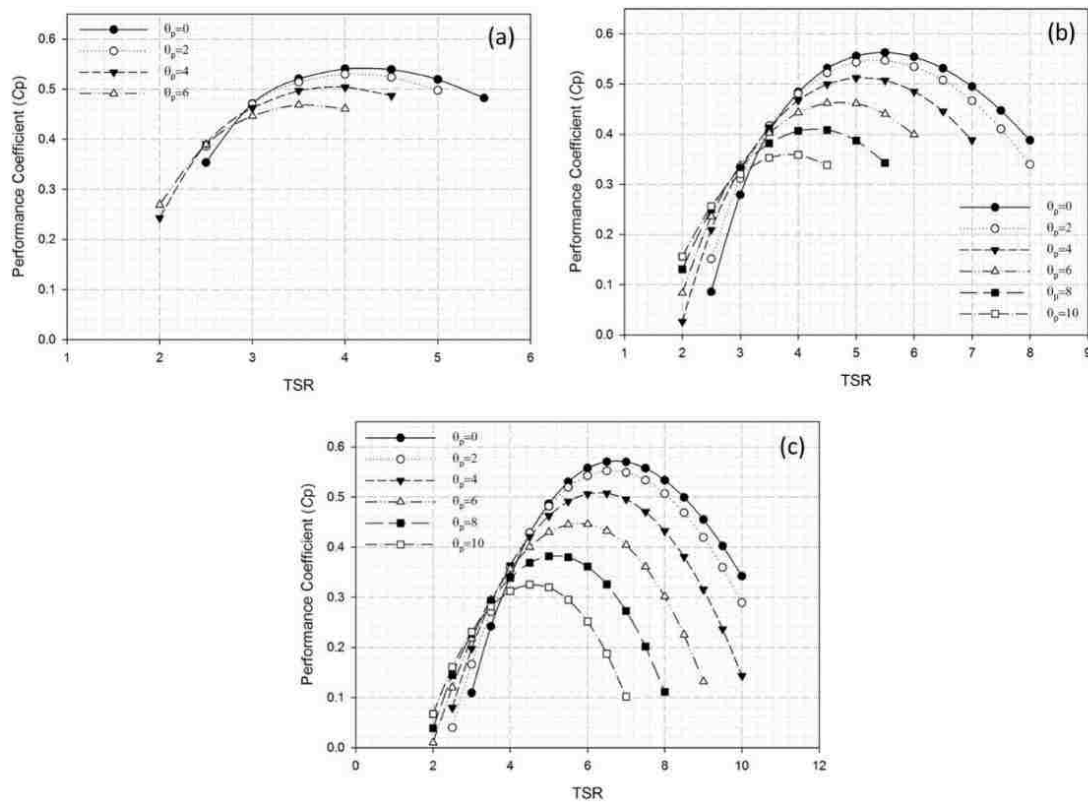
Figure 3.17: Figure 3.3.18: Effect of *TSR* (λ) and blade pitch angle on performance
coefficient for (a) Design_N75, (b) Design_N100, and (c) Design_N125

3.3.3.2 Multi-objective Optimization with GA

It can be noted that, the chord and twist distribution for all three hydrodynamically optimized designs follow a similar trend (Figure 3.16a,b). Hence, the curve fits to the chord and twist distribution of Design_N100 were used for the multi-objective hydro-structural optimization. The near hub chord-lengths were varied in the range [0.16m, 0.10m], and near tip chord-lengths in the range [0.05m, 0.03m] for GA optimization. As these designs were hydrodynamically optimized for the blade pitch of 0°, for GA multi-objective optimization, the design space for the blade pitch was set to [-3°, 3°] and TSR to [2, 7] to cover the design TSRs of all three designs. Table 3.4 presents representative Pareto optimal solutions, obtained from GA for variable chord, twisted blade geometry. As compared to a constant chord design (Table 3.2), this design yields higher C_p and lower stresses in the turbine blades.

Table 3.4: Pareto optimal solutions from GA for variable chord twisted blade

Sr #	Pitch [°]	*TSR*	Cp	**Flap-wise Bending stress [Mpa]**
1	1.46	3.68	0.39	103.5
2	1.48	3.91	0.42	111.6
3	1.52	4.22	0.45	121.4
4	1.44	4.55	0.48	131.7
5	0.87	4.82	0.51	140.8
6	1.05	5.21	0.52	148.8
7	0.07	5.4	0.53	158.6
8	0.02	5.72	0.54	165.2
9	-0.48	5.42	0.54	161.4
10	-0.92	5.87	0.54	174
11	-1.15	5.99	0.55	199

The C_p is improved from 0.47 (for constant chord blade design) to 0.55 (for variable chord, twisted blade design) with flap-wise bending stresses below 200MPa. This can be attributed to a more uniform blade loading, by virtue of providing a variable chord and twist distribution to the blade. Moreover, during CFD analysis for a constant chord blade, it was observed that the larger near tip area of a constant chord design was responsible for higher thrust force, which resulted in higher bending moment and hence higher stresses in the turbine blade. A variable chord, twisted blade design results in reduced stresses and improved hydrodynamic performance, due to higher blade twist near the hub region and smaller chord-length (hence blade area) near the blade tip. Thus, a variable chord, twisted blade design performs better than a constant chord blade from both a hydrodynamic and structural sense.

3.4 CONCLUSION

A multi-objective hydro-structural optimization was presented for both constant chord, zero twist blade turbine, and variable chord, twisted blade turbine designs. GA based on BEM proved to be a fast and efficient tool for hydro-structural optimization of HKTs. The results of optimization for a constant chord, zero twist blade design were supported with detailed CFD and FE analysis. Compared to the CFD analysis, the thrust and torque loading calculated from BEM, are under-predicted near the blade tip and over-predicted elsewhere. But, the integral performance parameters (total thrust and torque), calculated from BEM agree well with the CFD analysis. The total thrust forces obtained from the BEM analysis were comparable to the FSI analysis within ~7% variation. Thus, the BEM analysis offered a quick, reliable tool for multi-objective optimization, which would have been virtually impossible with CFD analysis, due to higher computational time involved. Though the

BEM analysis was able to predict the total thrust and torque loading on a turbine, it could not capture the variation of these forces along the blade span, due to inherent simplifications of the BEM theory. On the other hand, coupled CFD-FE analysis precisely determined this force distribution along the blade span and also considered the effect of the blade root thickness. This resulted in larger deviation (up to 30%) between stress compared to forces calculated from BEM and FSI analysis. A variable chord, twisted blade turbine was found to improve structural performance of a turbine without compromising any of the hydrodynamic efficiency. Three different blade designs were presented for different rotational speeds, and optimization was performed for variable chord, twisted blade design for hydro-structural performance improvement. The significant findings from our analysis are summarized below:

- Lower values of blade pitch angles and chord lengths maximize the hydrodynamic performance, while for the structural stability of a turbine, a higher blade pitch angle and lower *TSR* are required

- A hydro-structural optimization for a constant chord blade turbine yielded a C_p of 0.47 with flap-wise bending stresses of ~210MPa.

- For a constant chord blade design, a higher ΔP was observed across the blade section near the tip, as compared to rest of the blade that leads to a non-uniform blade loading and is considered to be detrimental to turbine life. This also implies a higher contribution of near tip part of the blade towards thrust and torque loading.

- Turbine blade geometries with variable chord and twist distribution along the blade span, resulted in the entire blade surface contributing uniformly to thrust and torque loading, thus, improving hydro-structural performance of turbine.

- Hydro-structural optimization with a variable chord twisted blade turbine resulted in C_p of 0.55 (a 17% improvement compared to a constant chord design) with flap-wise bending stresses below 200MPa.

CHAPTER 4*

PERFORMANCE CHARACTERIZATION AND PLACEMENT OF A MARINE HYDROKINETIC TURBINE IN A TIDAL CHANNEL UNDER BOUNDARY PROXIMITY AND BLOCKAGE EFFECTS

4.1 BACKGROUND

Unlike wind turbines, marine hydrokinetic turbines (MHkT) operate in a bounded flow environment where the flow is constrained between the free surface and the channel (river/sea) bed. In many cases, the channel depth for commercial scale MHkT installation is between $1.5D$ to $3D$ (where D is the turbine diameter), which leads to a blockage ratio (B=ratio of turbine area to channel area) greater than 0.1 [12]. Under such circumstances, the turbine is subjected to effects of solid blockage that modifies the flow-field around the turbine, and hence, affects its performance [13-15]. In addition, the rotational motion of the blades creates a low pressure, low velocity *wake* region behind the turbine; the rotating wake presents an additional restriction to the flow called wake blockage. Collectively, these two blockage effects result in accelerated flow near the rotor plane which in turn yields a higher performance compared to a turbine operating in an unblocked environment [16-18]. Quantifying the wake recovery distance behind a MHkT is thus important for designing optimum locations for multiple devices in a farm environment. Although the problem appears to be similar to wind-farm design; important differences exist primarily due to the bounded flow environment which alters the mechanism of wake recovery. This invalidates usage of wind-farm models in which wake restoration takes place by absorbing energy from the atmospheric boundary layer which can be treated as an infinite ambient reservoir [19]. For MHkT, where a limited water depth is available, the wake is tightly restricted between the channel bottom wall and the free surface which limits free expansion in directions perpendicular to the bounding surfaces. Installation also plays a pivotal role; MHkT can either be bottom mounted on a pier, anchored to the channel bed, or can be supported from a floating platform moored to the channel bed [20]. In both cases, they are

subjected to effects of boundary proximity of either the deformable free surface or the channel bed. Proximity of a turbine to the free surface presents additional complexity to flow structures, and hence, affects the turbine performance. The deformable free surface allows the water level to drop behind the turbine rotational plane [21]. Though the solid blockage is constant, the drop in free surface height and its deformation behind the turbine with the associated wake modifications are expected to influence the flow-field, and hence, turbine performance; the effects may vary significantly due to changes in effective flow conditions, operating *TSR* (ratio of blade flow speed to flow speed), Reynolds number (*Re*=ratio of inertial forces to viscous forces) and Froude number (*Fr*=ratio of characteristic flow velocity to gravitational wave velocity). The severity of this effect is expected to be a function of various parameters, including, but not limited to, blade shape (airfoil shape, chord and twist distribution), blade pitch angle, *TSR*, free surface proximity, channel wall proximity, and solid blockage itself.

An extensive literature review on wind-turbines was undertaken due to similarity in the working principle with MHkT. Several experimental studies have been carried out for wind turbines, in both unblocked and blocked flow environments, to investigate the effects of tip speed ratio, Reynolds number, blade profile, and velocity gradient that may exist across the rotor plane and turbulent wind characteristics [5, 19, 48-50]. However, the results are not directly applicable as the MHkT operates in a flow medium which is fundamentally different from wind turbines; denser working fluid leads to higher structural stresses on turbine blades [33, 51]. In addition, the MHkT operating at higher rotational speeds and high angle of attack in a near free surface environment may get subjected to cavitation effects [33]. Several experimental studies have also been performed to quantify

blockage effects on turbine performance. The majority of the early experimental work was done either in wind-tunnels or water channels with the aim of validation and verification of simple physics based models of such flows [5, 13, 48]. Chen and Liou [5] experimentally investigated effects of tunnel blockage on turbine performance. The blockage effect was quantified in terms of the blockage factor by measuring tunnel flow velocity with and without turbine. The blockage factor was found to be strongly related to solid blockage, *TSR*, and blade pitch angle. Higher blockage effects were observed at higher solid blockage and higher *TSR* values. McTavish *et al.* [14] studied effect of blockage on initial wake expansion for different sized rotors in a water channel, using a dye visualization technique. Higher blockage was found to narrow down the wake expansion and modify the vortex pairing behind the turbine. Several studies have also been performed to analyze free surface effect on marine current turbines; however, the majority of these studies used a porous disc to replicate the turbine rotor. Myers & Bahaj [55] carried out experiments with mesh disks to study the effect of disk proximity to sea bed/water surface on wake structures behind porous disks. Varying the disk proximity to sea/bed and water surface was found to affect wake structure and its recovery duration. Bahaj *et al.* [56] performed an analytical and experimental study to investigate the effect of surface proximity on turbine performance. Their experiments in a cavitation tunnel and tow tank showed reduction in turbine power with decreasing blade tip-free surface clearance. Experimental investigations by Birjandi *et al.*, [57] with a vertical axis hydrokinetic turbine, reported improved performance with increasing free surface proximity. The presence of a turbine in a tidal channel not only affects the downstream flow, but also the flow upstream of the turbine. Experimental and computational investigations of Medici *et al.* [48] show influence of blockage on flow up

to three turbine diameters upstream of the rotor plane. Near upstream flow showed three dimensional flow structures, indicating the effect of turbine geometry on incoming flow, similar to near wake flow.

Analytical models for characterizing the turbine performance are based on the application of the linear momentum theory. Garrett and Cummins [61] applied the linear momentum theory for flow constrained between two rigid surfaces, and found an increase in turbine power with increasing blockage ratio. Houlsby *et al.* [21] used the linear momentum theory to analyze a pressure constrained, parallel-sided tube scenario, with an extension to open channel flow. A quartic equation was presented relating flow Froude number, blockage ratio, and flow speeds in the wake and bypass region behind the turbine. A similar analysis was presented by Whelan *et al.* [21] yielding a quartic equation relating the above quantities. Analytical predictions were comparable with experimental data for the mesh disc simulator and two bladed rotor in wind tunnel, and water channel for different blockage conditions. Lartiga and Crawford [52] used an actuator disc modelling with blockage corrections to predict the performance of a tidal turbine in a blocked environment. Flow field data from PIV measurements and CFD simulations were used to account for the blockage effect. Analytical predictions were in good agreement at a lower blockage ratio but showed significant deviations at higher blockage ratios. Computational study by Sun [53] with porous discs, reported localized flow acceleration in the region between the wake and channel bottom. Free surface drop behind the mesh disc was observed to affect wake characteristics and turbine performance as well. Consul *et al.* [15] investigated the effect of blockage and free surface deformation on performance of a marine cross-flow turbine for different blockages, and free surface boundary conditions using two-dimensional CFD

90

modelling. The deformable free surface boundary condition lead to 6.7% performance improvement compared to closed top condition, due to higher effective blockage caused by free surface deformation. The Froude number (over the range studied: 0.08 to 0.13) was reported to have very small effect on power coefficient, but significantly affected the free surface drop. Recently, Bai *et al.* [62] performed numerical simulations using an immersed boundary method to predict marine current turbine performance under free surface flow conditions, and validated it with experimental data. No significant free surface deformation was reported with the turbine operating with the blade tip immersed $\sim 1 \times R$ below the free surface, where R denotes the turbine radius. Computational study by Zhou and Wang [63] investigated the effect of the Froude number, turbine diameter, and depth of immersion on a free surface wave induced by a tidal turbine and its effect on turbine performance. But, the computational study was not able to conclude on the effect of depth of immersion on turbine performance. Lee *et al.* [100] used BEM and CFD based models for performance prediction of a horizontal axis tidal turbine. A new design was suggested with raked tip blades for better cavitation and acoustic performance. Though there is an increasing body of work focusing on experiments, computations and analytical models to quantify blockage and free-surface effects on performance, the majority of the experimental and computational studies model turbine as a porous mesh disc, and analytical models are limited to actuator disc modelling [27, 53, 55, 56].

To the knowledge of authors, there is no quantitative computational or experimental study exploring the effect of blockage and wake-bypass flow interaction, aiming to determine optimum depth of immersion for MHkT installations. We report results of computational and experimental investigations to quantify the effect of blockage and

boundary proximity on the performance of a three bladed MHkT. Experimental

investigations are augmented by a flow field characterization with steady and transient

computational fluid dynamics study. Three dimensional CFD with rotating reference frame

technique was used to quantify the effect of the Reynolds number and the blockage ratio

on turbine performance characteristics. Transient CFD calculations for wake and free

surface flow characterization take into account buoyancy effects and free surface effects

using a volume of fluid (VOF) approach [64]. Experiments were carried out in an open

surface water channel with a constant chord, zero twist hydrokinetic turbine under various

operating conditions. Flow speed, rotational speed and turbine submerged depth were

varied during the experiment to study their effects on turbine performance. Flow speed was

varied from 0.5m/s to 0.73m/s to achieve different Froude numbers [0.20, 0.27, 0.3].

Further, to investigate the effect of surface proximity, the turbine submerged depth was

varied so that the blade tip to free surface clearance (h_U) is between 0.01m - 0.22m.
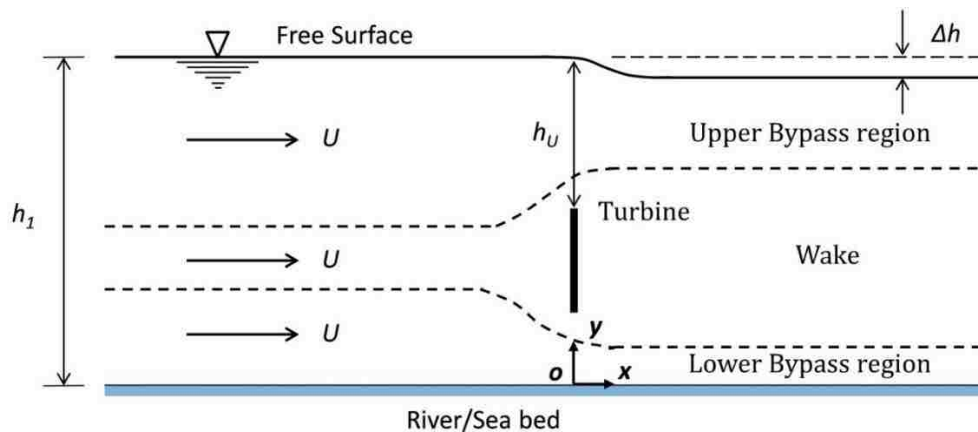
Figure 4.1: Schematic of flow around MHkT in shallow river/tidal channel showing wake, upper bypass and lower bypass regions.

This lead to turbine tip clearance ratios (δh_U) of 0.03 to 0.73 (see Figure 4.1), which

represents the ratio of the water height above the turbine rotation disc (h_U) up to free

surface to the turbine diameter (*D*).Current experimental and computational investigations will enhance our limited understanding of flow-field around MHkT in its natural environment. Further, experimental investigations will provide useful means to quantify the effect of boundary proximity on MHkT performance thereby facilitating MHkT site selection and deployment process.

4.2 COMPUTATIONAL FLUID DYNAMICS

To understand the flow-field around a marine hydrokinetic turbine operating under various Reynolds number and boundary proximity conditions, a three dimensional CFD analysis was carried out using both steady state and transient solver schemes. Steady state analysis was carried out using multiple reference frame approach in CFX. More details about this technique can be found in [35, 51, 88]. A moving mesh technique was adapted for transient simulations for which inner domain containing the, turbine rotates at specified angular velocity during each time step until convergence for continuity and momentum equations is reached. The flow domain consisted of 3.5 million hybrid cells with prism layers on the turbine surface for boundary layer resolution (Figure 4.2).
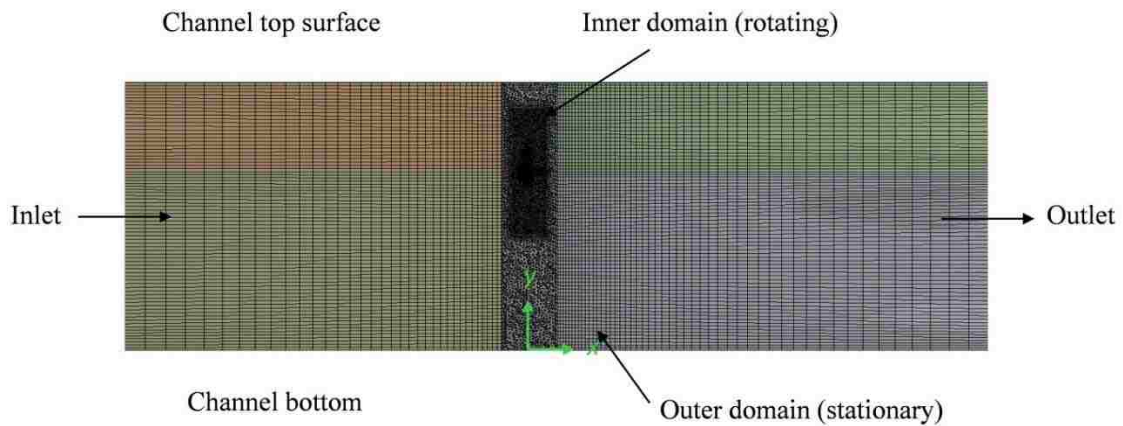
Figure 4.2: Computational mesh used for CFD study

93

A grid convergence study was carried out by varying the mesh size from 1.5×10^6 cells to 4×10^6 cells and a mesh with 3.5 million cells was found to be optimum from computational and accuracy standpoint which resulted in less than a 5% variation in torque compared to a finer mesh of 4×10^6 cells. The mesh used for fluid domain is such that average y^+ (which defines distance of first mesh node from the wall) is 2.2 with y^+ ranging between ($0.1 \leq y^+ \leq 9$) for the highest flow speed and RPM case, i.e. $U = 0.9$m/s, $TSR = 8$ that corresponds to tip speed velocity of 7.26m/s. Reynolds averaged Navier-Stokes (RANS) equations were solved using the κ-ω SST turbulence model for which, $y^+ \leq 10$ is acceptable for predicting boundary layer separation effects [71, 72]. Figure 4.2 shows schematic of fluid domain used during computations reported in this paper. The simulation domain was modeled to an actual water channel test section of size 0.61m × 0.61m and 1.98m long. A uniform velocity of 0.5m/s was specified at the inlet. The channel outlet was specified outlet boundary condition with relative pressure of zero. The reference pressure for simulations was set to atmospheric pressure. The channel walls were modeled as no-slip walls and channel top is modeled as entrainment with zero relative opening pressure. With entrainment option at channel top surface, the flow direction is not specified, but the flow solver locally calculates the flow direction based on flow velocity field. Buoyancy effects were modeled during transient simulations, but were neglected for steady state analysis. The tunnel bottom was specified as a reference for gravity and hydrostatic pressure calculations along the channel depth. Transient simulations were carried out for flow velocity of 0.5m/s and rotational speed of 200RPM, which corresponds to *TSR* (ratio of blade tip speed to flow speed) of 5.85. Time step was selected, such that the turbine rotated 2° during each time step which lead to an average CFL (Courant–

Friedrichs–Lewy condition) number of less than 5. A CFL number defines a necessary condition for numerical stability of a hyperbolic partial equation. The restriction on a CFL number depends on type of solver (discretization scheme) used for CFD analysis. For the explicit solver, CFL<1 provides good convergence, while for implicit solver higher values of CFL are acceptable. Current CFD analysis was performed with an implicit solver within CFX for which CFL<5 was acceptable from numerical stability and expense standpoint [73]. Further, to ascertain the convergence with respect to time step size, an independence study was performed by varying time step size such that the turbine blade rotated 5°, 3°, 2° and 1° per time step. The difference between calculated power coefficients with respect to 2° case was 11%, 7%, 0% and 1.5% respectively. Thus, a time step that corresponds to 2° rotation was chosen for current analysis considering numerical stability, accuracy and computational expenses. The fluid domain was initialized with a flow velocity of 0.5m/s and turbulence intensity of 5% throughout the domain. In addition, the hydrostatic pressure at every point (and time step) in the domain was determined from density, volume fraction and hydrostatic head at that instant of time using a user defined function. The turbulence boundary conditions at inlet and outlet were specified as turbulence intensity of 5% and turbulent viscosity ratio of 10%. The convergence criteria for r.m.s. residuals of continuity, momentum, and turbulence quantities were set to 10^{-5}. During transient simulation, initial free surface height at the channel outlet is specified as 95% of the inlet height (5% free surface drop). This assumption was based on the blade element momentum calculations, incorporating a quartic equation relating blockage ratio, Froude number, bypass flow and wake flow for current turbine prototype and operating conditions [21, 50]. In addition, during experimentation, the free surface height at the channel exit was found to be

dependent on flow speed, rotational speed and depth of immersion that varied from 1% to 5% of channel depth. Since the value of the free-surface drop is not known, *a priori*, a value of 5% obtained from BEM predictions which also corresponds to the maximum drop measured during experimentation was used in all simulations. The dynamic variation of free surface height along the channel length (and width) is determined during transient simulations using the VOF formulations. Free surface simulations were carried out in ANSYS CFX 15.0 using multiphase modeling with homogeneous model which uses VOF approach, and is based on the concept of fluid volume fraction. A common flow field, temperature and turbulence field is shared by all fluids and for a given transport process, transported properties (except volume fraction) are assumed to be same for all phases [35]. The VOF model as developed by Hirt and Nichols [64] is based on the Eulerian approach (volume-tracking) where fluid flows through a fixed mesh. The VOF method assumes that each control volume contains only one phase (water, air or interface between the two in this case), and solves only one set of momentum equation for all phases (Equation 4.1)

$$\frac{\partial}{\partial t}\left(\rho u_j\right) + \frac{\partial}{\partial x_i}\left(\rho u_i u_j\right) = -\frac{\partial P}{\partial x_j} + \frac{\partial}{\partial x_j}\mu\left(\frac{\partial u_i}{\partial x_j} + \frac{\partial u_j}{\partial x_i}\right) + \rho g_j + F_j \qquad (4.1)$$

where, u represents fluid velocity components, P is fluid pressure, μ represents effective fluid viscosity, ρ is fluid density, g is acceleration due to gravity, and F represents body forces. In this approach, actual interface is not tracked, but in fact, is reconstructed from other flow field properties like volume fraction. A step function (α) is used to define presence or absence of water within the computational domain. A value of 1 defines presence of water and value of zero defines presence of air within the control volume. The control volumes for which α are neither zero nor one represent the interface region between

96

water and air. The tracking of the interface between the fluids is accomplished by solving the volume fraction continuity equation for one of the phases (q^{th} phase in Equation 4.2).

$$\frac{1}{\rho_q}\left[\frac{\partial}{\partial t}\left(\alpha_q\rho_q\right)+\nabla\cdot\left(\alpha_q\rho_q\vec{v}_q\right)=\sum_{p=1}^{n}\dot{m}_{pq}-\dot{m}_{qp}\right] \qquad (4.2)$$

where, $\dot{m}_{qp}$ is the mass transfer from phase q to phase p and $\dot{m}_{pq}$ is mass transfer from phase p to phase q. It was assumed that the interface between the two phases remain distinct and well defined so that air does not get entrained into water.

4.3 FACILITY, EXPERIMENTAL SET-UP AND MODEL PROTOTYPE

All experiments were carried out in an open surface recirculating water channel at Lehigh University with a test cross-section size of 0.61m × 0.61m and length of 1.98m (Engineering Laboratory Design, USA). This facility is equipped with a 25HP single stage axial flow propeller pump with maximum discharge of 5590 gallons per minute. The propeller pump RPM and hence the test section flow velocity is controlled and regulated through a transistor inverter type, variable frequency controller (Toshiba Model VFAS1-2185PM-HN). Flow velocity can be varied from 0.03m/s to 0.94m/s and can be measured within an accuracy of ± 2%. The flow quality is such that the turbulence intensity is maintained to a value of less than 1%.

4.3.1 Turbine prototype

The model prototype used for current study is a three bladed, 0.14m radius (*R*), zero twist, constant chord (0.01676m) blade turbine made from corrosion resistant aluminum alloy (Figure 4.3). Turbine blades are formed from SG6043 airfoil on a five-axis CNC machine. Turbine blades are held together inside a two-part hub, and their orientation can

be changed to adjust blade pitch to the desired angle. To limit the number of independent variable to minimum, all experimental runs were performed with the turbine blades oriented at 10° blade pitch. The turbine prototype, when operated in our facility leads to an area based blockage ratio of 16.5%.
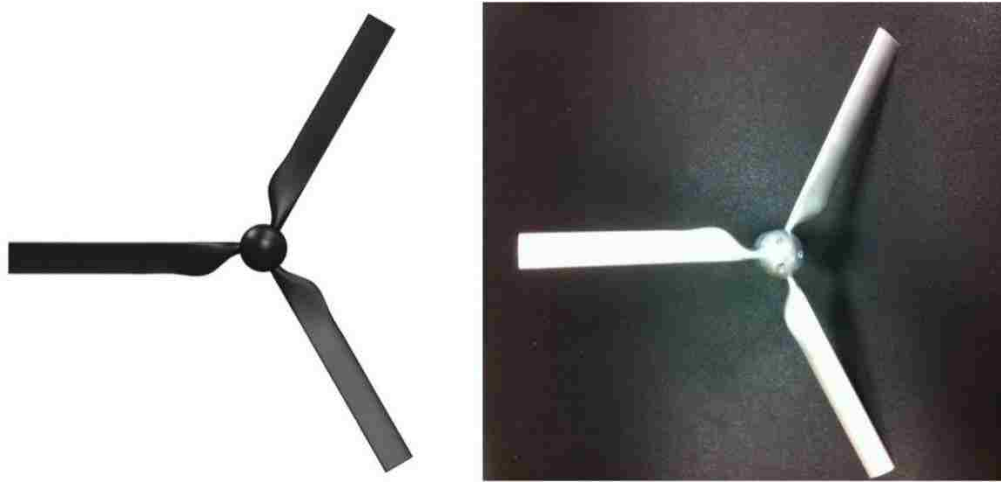
Figure 4.3: CAD model and photograph of turbine prototype used for current study [R=0.14m]

4.3.2 Experimental setup

The experimental setup (see Figure 4.4) consisted of a lab scale model hydrokinetic turbine attached to a horizontal shaft, driven by a stepper motor which maintains a precise rotational velocity through a micro-stepping driver and controller mechanism. The stepper motor used for current study was NEMA23 series, 24VDC motor with resolution of 1600 micro-steps per revolutions. The stepper motor was connected to the turbine shaft through a flexible coupling. The motor and flexible coupling were enclosed inside a watertight acrylic cylinder, which was then connected to a thrust torque sensor (Model # TFF400, Futek Inc.). The acrylic cylinder was continuously pressured/purged to avoid water leakage into the system.

1 – Turbine, 2 – Flexible Coupling, 3 – Motor, 4 – Thrust-Torque Sensor, 5 – Support Structure, 6 – To Motor Controller, 7 – To Data Logging

Figure 4.4: Schematic of experimental set-up [R=0.14m]

Finally, the reaction torque-thrust sensor was fixed to a vertical post, which was connected to a horizontal frame supported at channel top. The vertical post can be raised/lowered inside the water channel to vary the free surface proximity of the turbine. During the experimental run, data from torque-thrust sensor was continuously monitored and acquired on a desktop computer at a high sampling rate of 500 samples/second for further analysis. According to the manufactures specifications, the torque/thrust sensor was accurate to within ± 1% for the current measurement range, which was also confirmed by in-house calibration. A single sample uncertainty analysis for U, RPM, and torque, based on Kline and McClintock [77] showed maximum uncertainty of 1% on the *TSR* and 3% on the C_p calculations.

4.4 RESULTS AND DISCUSSION

Results from experimental and computational investigations, carried out on a constant chord, untwisted three bladed MHkT are discussed. Experiments were carried out with the turbine operating at various flow velocities and immersion depths over a range of *TSR* values. Experimental data is compared with CFD results for three flow velocities (0.5m/s 0.73m/s, and 0.9m/s) for validation purpose. Upon validation, the CFD technique was extended to investigate the effect of blockage ratio and flow velocity on turbine performance. CFD analysis is carried out for various sized flow domains to model different blockage conditions. The effect of the Reynolds number on the turbine performance was investigated by subjecting the turbine to flows with various inflow velocity conditions at domain inlet. Experimental runs in addition to the validation cases were performed with the turbine operating at various depths of immersions to analyze the effect of boundary proximity (deformable free surface and non-erodible channel bottom wall) on the turbine performance in an attempt to determine an optimum submersion depth that corresponds to a maximum power coefficient for the turbine.

4.4.1 Validation of CFD technique

Figure 4.5 presents a comparison between experimental data and steady state CFD predictions for various flow velocities. During experimentation, the turbine was submerged such that its axis was at the central height of channel and turbine performance was measured at flow velocities of 0.5m/s, 0.73m/s, and 0.9m/s over a range of *TSR* values which correspond to turbine diameter based Reynolds number of 1.4×10^5, 2.0×10^5, and 2.5×10^5 respectively. For a *TSR* of 5, these flow speeds correspond to Reynolds numbers

of 4.1×10^4, 6×10^4, and 7.4×10^4 respectively based on chord length and flow velocity at the blade tip.
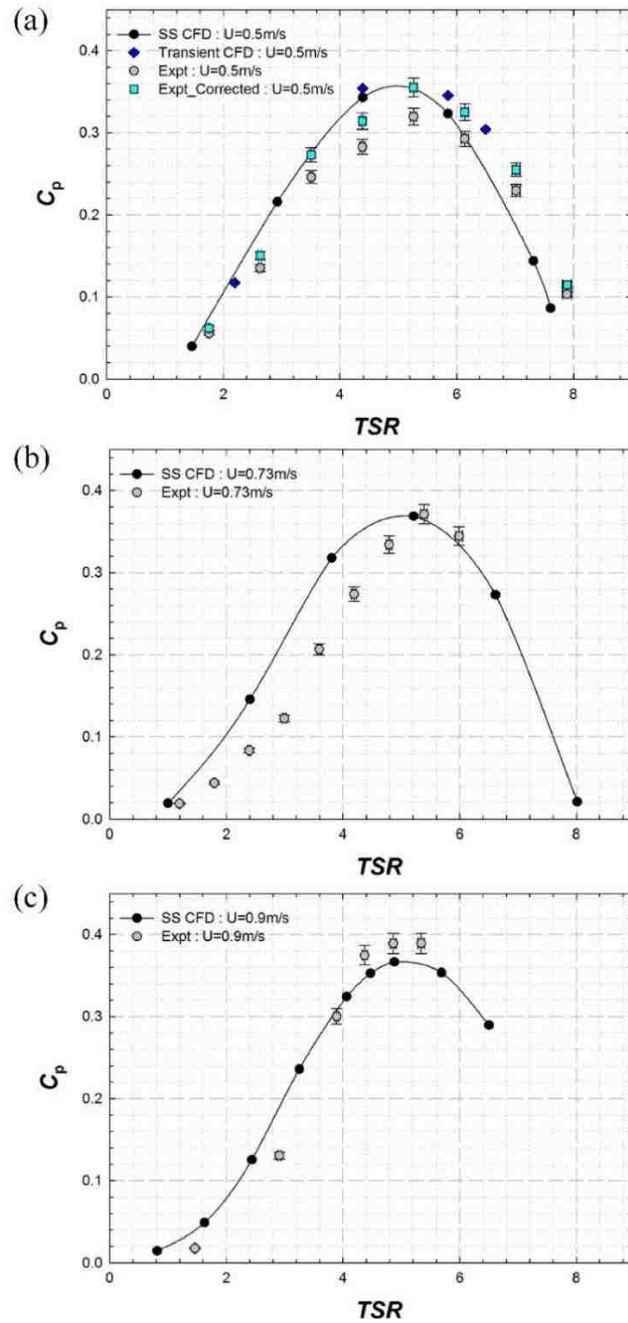
Figure 4.5: Comparison of experimental data with steady state (SS) CFD results for (a) *U* = 0.5m/s, (b) *U* = 0.73m/s and (c) *U* = 0.9m/s (vertical and horizontal error bars represent uncertainty in C_p and *TSR* measurements respectively), blue diamonds in Figure (a) represent predictions from transient CFD.

The Froude number based on total channel depth (upstream the turbine) for these flow velocities were 0.2, 0.3, and 0.37 respectively. For each flow speed, the rotational speed was varied from 30 to 300 revolutions per minute (RPM) and torque values were recorded from a submerged torque-thrust sensor at a sampling rate of 500 samples per second.

As the flow speed increases from 0.5m/s to 0.73m/s, so does the turbine performance. This can be attributed to higher lift forces on turbine blades due to increase in Reynolds number (based on chord and effective velocity at blade tip) form 4.1×10^4, to 6×10^4. However, increasing flow velocity (U) from 0.73m/s to 0.9 m/s did not cause any appreciable change in C_p vs. *TSR* curve (compare Figure 4.5b and c) suggesting that turbine performance is weakly sensitive to Reynolds number effect beyond U=0.73m/s for the range of Reynolds numbers considered in the current study.

Another aspect of improvement in performance with flow velocity is related to increase in Froude number which defines the relation between relative flow velocity and gravitational flow speed. Higher the flow velocity compared to gravitational flow speed (which is a function of channel depth), higher the Froude number. This change in Reynolds and Froude number is associated with flow field modification in near downstream and near upstream regions of turbine and hence affects the turbine performance.

For flow velocity of 0.5m/s, in addition to actual measured experimental data, a corrected curve is added considering assumed system efficiency of 10% to account for losses due to friction and torque transmission form turbine to reaction torque sensor. From Figure 4.5, it follows that CFD tend to over-predict the performance at lower *TSR* values, but at higher rotational speeds (when blockage effects are high, as discussed in §4.3) experimental data shows higher C_p compared to CFD prediction. Further, it is to be noted

that, CFD and experimental data curves for C_p vs. *TSR* for all flow velocities cross each-other at rotational speed around 200 to 250RPM (*TSR* range of 4 - 6). The deviation in performance prediction can be attributed to absence of free surface and buoyancy modeling during steady state CFD analysis which modifies the flow field (and provides additional blockage), and hence, the turbine performance. In addition, the implication of blockage effects is not only to increase the turbine performance, but also to shift the entire C_p vs. *TSR* curve (for experimental data) away from the origin (in east-north direction), thereby shifting the optimum performance to higher *TSR* value as can be seen in Figure 4.5. The severity of this effect varies with flow speed and rotational speed as will be illustrated in Figures 4.8 and 10, in the later part of this manuscript. These effects were modelled during transient CFD analysis as presented in §4.4.2. A flow speed of $U = 0.5$m/s and *TSR* value of 5.85 was chosen for transient simulations, around which a good match was observed between CFD predictions and experimental data. The diamonds on Figure 4.5a present C_p predictions from transient CFD that show higher values compared to steady CFD and show better agreement with corrected experimental data. In spite of the inability to model buoyancy and free surface effects, steady state CFD presented a computationally efficient approach for turbine performance characteristics prediction. It is to be noted that, the computational domain and turbine model are 1:1 replica of actual water channel and turbine prototype. This results in similar blockage effects for data-sets from both experiments and CFD modelling. Hence during CFD validation, blockage corrections were not applied to the experimental data. The effect of blockage on turbine performance is investigated separately and is reported in § 4.4.3.

4.4.2 Effect of Reynolds number on turbine performance characteristics

Though it is customary to express turbine performance characteristics in terms of non-dimensional parameters -TSR and C_p, one has to be cognizant of the fact that TSR does not represent actual flow velocity, but is a ratio of blade tip velocity to flow velocity. Turbine blades are often made from airfoil sections whose lift and drag characteristics are strongly dependent on the operating Reynolds number, and hence, flow velocity. A turbine when placed in tidal/river channel will be subjected to varying flow speeds, hence, it is important to understand the effect of the Reynolds number on its performance characteristics over a wide range of flow velocities. During the present study, a steady state CFD with rotating reference technique [35, 51, 88], validated with experimental data was used to understand the effect of the operating Reynolds number on turbine performance. CFD simulations were carried out for a lab scale prototype operating in a water channel sized fluid domain at flow velocities ranging from 0.1m/s to 0.9 m/s. The results of variation of performance characteristics with flow velocity are presented in Figure 4.6. With increasing flow velocity from 0.1m/s, an improvement in turbine performance was observed with C_p vs. TSR curve reaching higher maxima and spreading over wider TSR range. The improvement trend continued until flow velocity reached 0.7m/s above which no appreciable improvement was noticed. This corresponds to chord based Reynolds number of 1.2×10^4 and diameter based Reynolds number of 2.0×10^5 beyond which C_p vs TSR curve became insensitive to Reynolds number changes at high TSR values ($TSR>5$), but was weakly sensitive to Reynolds number changes at low TSR values.
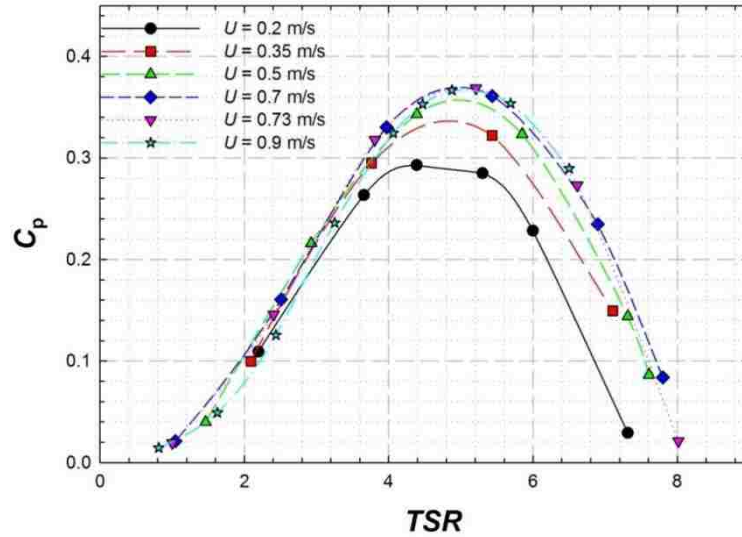
Figure 4.6: Effect of flow velocity on turbine performance characteristics

4.4.3   Effect of blockage on turbine performance characteristics

The steady state CFD technique was used to investigate the effect of blockage on turbine performance characteristics. The turbine geometry used for CFD analysis was a three bladed lab prototype of 0.14m radius. Fluid domains of different cross-section sizes were created to achieve various (solid) blockage ratios in the range [0.042, 0.42]. The largest domain corresponds to the test section of 1.22m$\times$ 1.22m and the smallest test section size corresponds to 0.38m$\times$ 0.38m. All other test sections have a width of 0.61m, but height varying from 0.3m to 1.22m to achieve various blockage ratios. All simulations were carried out with a channel inlet flow velocity of 0.5m/s. Figure 4.7 shows a variation of turbine performance with *TSR* at various blockage ratios. For blockage ratios below 10%, no significant variation of performance characteristics was observed, thus no blockage corrections are necessary. Increasing the blockage ratio beyond 10% resulted in consistently higher performance, with up to ~35% improvement in C_p for the case with 42% blockage when compared to the unblocked case. At lower *TSR* values (<4), the turbine

105

performance was found to be weakly dependent on blockage ratio. But with increasing *TSR*, performance curves started deviating from each other showing a stronger influence of blockage. Higher blockage ratios were found to increase torque on the turbine resulting in improved performance.
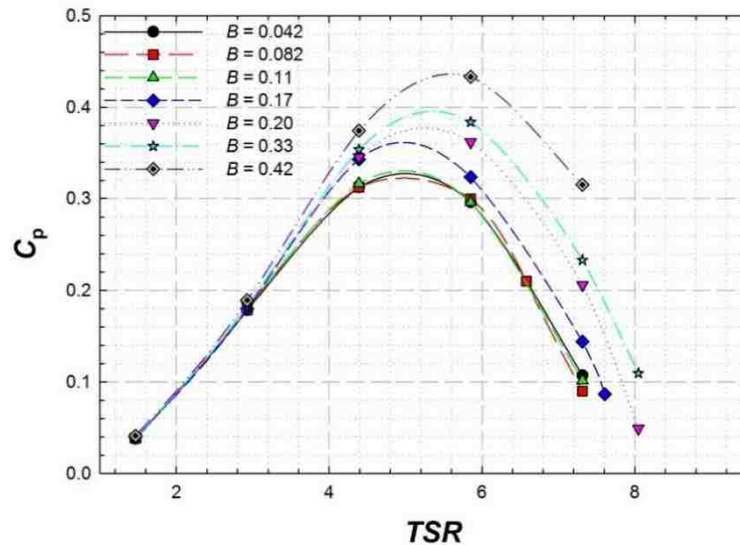
Figure 4.7: Effect of blockage ratio on turbine performance characteristics

The total blockage to which the turbine is subjected is a combination of solid blockage and wake blockage [16, 17] and changes with turbine rotational speed. Higher rotational speed represents a faster rotating wake resulting in stronger wake blockage effect. To get a better insight into the effect of turbine rotational speed on blockage effect, data set from steady CFD analysis are plotted in Figure 4.8a, such that the Y-axis represents the turbine performance and the X-axis represents solid blockage. Lines of constant *TSR* values: 1.46, 2.93, 4.39 and 5.85, are plotted and compared. At lower *TSR* value (1.46), blockage does not seem to have any effect on Cp. This is due to the fact that, at low rotational speeds, turbine blades experience a high relative angle of attack that causes flow separation on blades. An increase in blockage leads to larger effective flow velocity further increasing

the relative angle of attack. This worsens the flow separation on turbine blades, adversely affecting its performance. Thus, blockage induces competing phenomena of elevated velocity (which increases torque), and increased flow separation (which reduces torque). At low *TSR* values, the improvement in turbine performance due to elevated effective velocities is nullified by flow separation effects, and blockage does not cause any appreciable enhancement in the power coefficient as illustrated in Figure 4.7. Further, it is to be noted that, the untwisted blades used for current turbine prototype results in varying angles of attack along the blade span, maximum near the blade root and minimum at the blade tip. This will lead to span-wise flow variation with likelihood of flow separation (especially at low *TSR* values) at near-root sections (higher angle of attacks) without any flow separation for near-tip sections. These separated flow features can then propagate outwards along the blade span (Coriolis and centrifugal forces) towards the tip, destabilizing the entire blade boundary layer. As the *TSR* value increases from 1.46 to 2.93, the percentage change in C_p from lowest blockage ratio (0.042) to highest blockage ratio (0.42) increases to 6%. Higher *TSR* values lead to larger variation of C_p with blockage, with maximum improvement of ~52% observed at *TSR* of 5.85. An interesting behavior was observed for *TSR* 4.39 and 5.85 cases: at blockage ratios below 0.2, *TSR* 4.39 case consistently showed higher performance as compared to *TSR* 5.85 case, but above solid blockage of 0.2, inflexion was observed with *TSR* 5.85 case performing better than *TSR* 4.39 case. Higher *TSR* cases (not presented here) showed even higher fluctuations in C_p vs. blockage curve with more than three inflexion points. This can be attributed to interaction of stronger wake blockage (due to free surface deformation) with solid blockage at these high *TSR* that leads to a complex, coupled total blockage affecting turbine performance.

For a given flow speed and blockage ratio, an increase in rotational speed leads to faster

bypass flow, yielding higher C_p as plotted in Figure 4.8a.
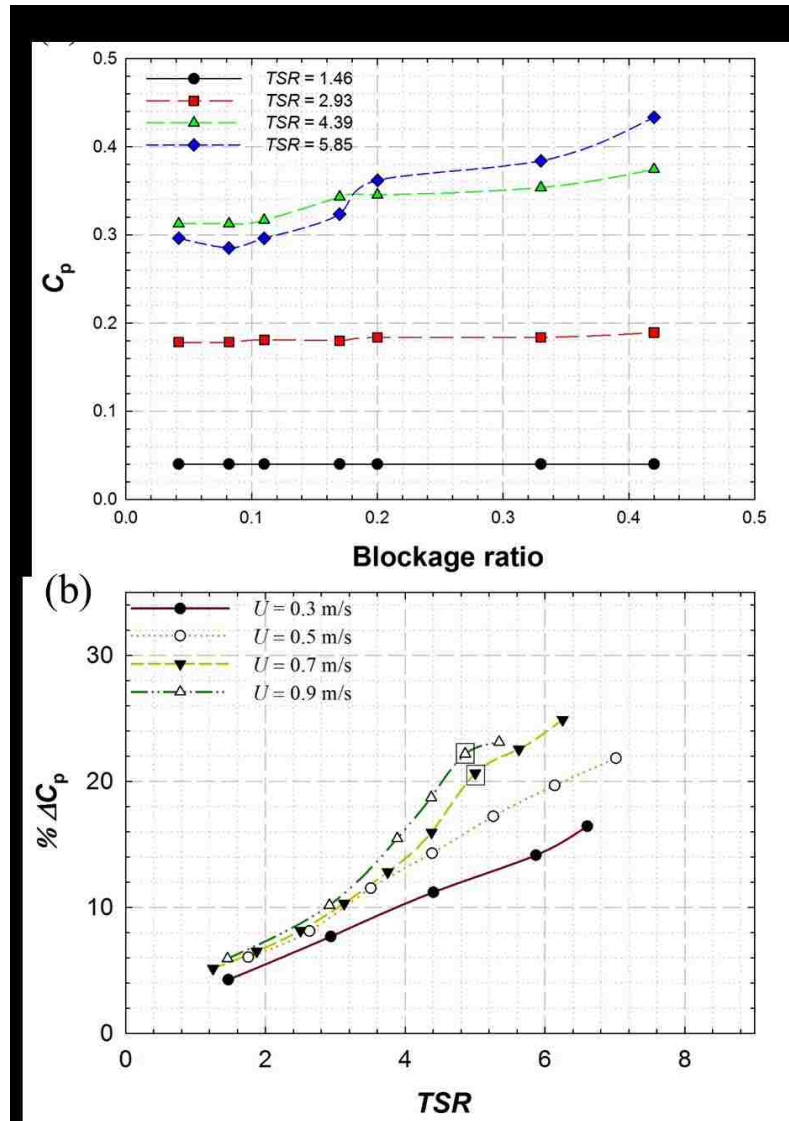
Figure 4.8: Influence of TSR on blockage effect. (a) Variation of power coefficient with blockage ratio at various *TSR* values: CFD study; (b) Effect of *TSR* on percentage increase in measured *C*p (with respect to unblocked case) at various flow velocities: Experimental data

However, for a given U and B, there exists a *TSR* at which a sudden jump in C_p is observed.

The location of this inflexion point depends on flow velocity, rotational speed and blockage

ratio. To confirm this hypothesis, additional experimental runs were performed with lab

prototype at higher flow velocities. Experimental data was then corrected according to the blockage correction proposed by Bajah *et al.* [13]. Figure 4.8b presents percentage change in power coefficient between corrected and measured (raw-experimental) data $\left[\% \Delta C_p = \left(C_{p\,Measured} - C_{p\,Corrected} \right) / C_{p\,Corrected} \times 100 \right]$. The data presented in Figure 4.8b is from experimental runs for lab prototype corresponding to a blockage ratio of 0.165. At this blockage ratio, no inflexion was observed for U=0.5m/s. However, for higher flow velocities of U=0.7m/s, the transition in C_p occurred at a *TSR* of ~5 while for U=0.9m/s, transition occurred early, at *TSR* of ~4.8. These points are marked by rectangles in Figure 4.8b. Thus the inflexion behavior depends on flow velocity, rotational speed and blockage ratio which govern the flow velocities in the bypass flow, and hence, blockage effects.

4.4.4   Effect of boundary proximity on the turbine performance

When a turbine operates in a shallow channel, as the present case, the flow in its proximity can be decomposed into two main components: (1) the flow passing through a stream-tube enclosing turbine rotation disc, which expands behind it forming a region commonly known as wake and, (2) a region called bypass region which is composed of the remaining flow channel. We further decompose this bypass region into two zones: a flow region between free surface and rotor disc, called *upper bypass* region and, a region that lies between solid channel wall and rotor disc plane called *lower bypass* region. Such a distinction is required, due to the very nature of widely different boundaries curtaining these regions. While the flow is tightly restricted by the channel solid wall from the bottom (which may be erodible or non-erodible), the upper free surface is deformable, and does not offer strong restriction to wake expansion and bypass flow restoration. To understand

the effect of boundary proximity (free surface and channel bottom wall) on turbine performance, experimental investigations were carried out by varying the tip clearance ratio (δh_U) from 0.03 to 0.73 (see Figures 4.1 and 4). At each of these submersion depths, the rotational speed was varied from 30-300 RPM, and torque values were recorded from a submerged torque-thrust sensor at a sampling rate of 500 samples per second. Experiments were repeated for three different flow speeds: 0.5m/s, 0.66m/s, and 0.73m/s to understand how Reynolds number variation affects the turbine performance in presence of boundary proximity effects. Table 4.1 presents details of experimental runs carried out during the current study.

Table 4.1: Flow variables and turbine depth of immersions investigated during current experimental study

Flow Velocity U [m/s]	Re_{Chord} (U_{tip}, TSR=5)	Re_{Diameter}	Froude number	Tip clearance ratio (δh_U)
0.5	4.1×10^4	1.37×10^5	0.2	
0.66	5.4×10^4	1.8×10^5	0.27	0.03, 0.20, 0.55, 0.73
0.73	6.0×10^4	2.0×10^5	0.3	

4.4.5   Results of experimental investigation for boundary proximity effects

Figure 4.9 presents results of experimental investigations where C_p is plotted against *TSR* for three different velocities: U=0.5m/s, 0.66m/s and 0.73m/s. This corresponds to the turbine diameter based Reynolds number of 1.37×10^5, 1.8×10^5, and 2.0×10^5 respectively, and blade chord based Reynolds number of 8.2×10^3, 10.8×10^3, and 12×10^3 respectively. For all cases, lowest performance was observed when the turbine was at largest depth in our facility (δh_U =0.34). With reduction in depth of immersion, improved performance was
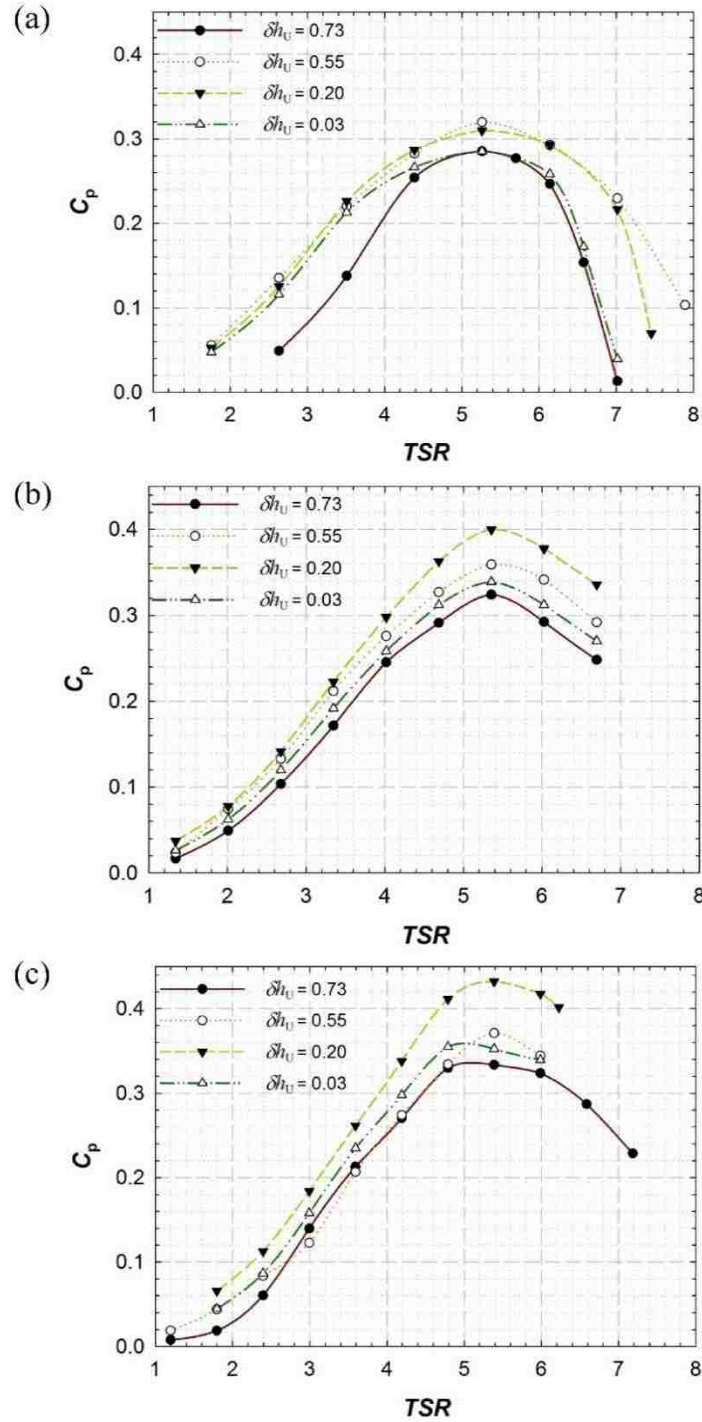
Figure 4.9: Effect of free surface proximity on turbine performance at different flow velocities (a) $U = 0.5$ m/s, (b) $U = 0.66$ m/s and (c) $U = 0.73$ m/s

observed until $\delta h_U = 0.20$ for all cases, except lower flow velocity of $U=0.5$m/s for which

both $\delta h_U = 0.20$ and $\delta h_U = 0.55$ resulted in similar maximum C_p values. Thus, flow with a

higher Froude number (and Reynolds number) was more susceptible to boundary proximity effects. An increase in flow speed was observed to improve the turbine performance with maximum performance achieved at a flow speed of 0.73m/s and δh_U =0.20. Moving the turbine away from channel bottom wall resulted in improved performance. This indicates that the close proximity of the channel wall affects the flow field behind the turbine, and restricts wake expansion and reduces the turbine performance. This trend continued until h_U reached around 10% of channel depth (δh_U =0.2) or 50% of turbine radius. Beyond this point, though the turbine was away from the solid channel wall, it was in close proximity of a free surface leading to significant free surface deformation behind the rotor plane which interacted with the turbine wake affecting its performance. This observation was also supported by transient CFD analysis results which are described in §4.4.2.

To identify the optimal depth of immersion for efficient turbine operation, experimental data for 0.5m/s, 0.66m/s and 0.73m/s cases is re-plotted in Figure 4.10 which presents power coefficient vs. tip clearance ratio curves at different *TSR* values. For the flow velocity of 0.5m/s, for all *TSR* values, the turbine was found to perform at consistently higher C_p values over a wider range of tip clearance ratios: δh_U 0.2 to 0.5 (Figure 4.10a). With increase in flow velocity (and corresponding rotational speed to maintain the *TSR*), optimum tip clearance depth (h_U) for turbine performance started to shift around 10% of the total channel depth (δh_U =0.2, which also corresponds to 50% of turbine radius). For both 0.66 and 0.73m/s flow velocities, maximum performance was observed when the tip clearance ratio was close to 20% (Figure 4.10b, c). Any depths, lower than that, induced strong free surface-wake interactions degrading the turbine performance. This indicates
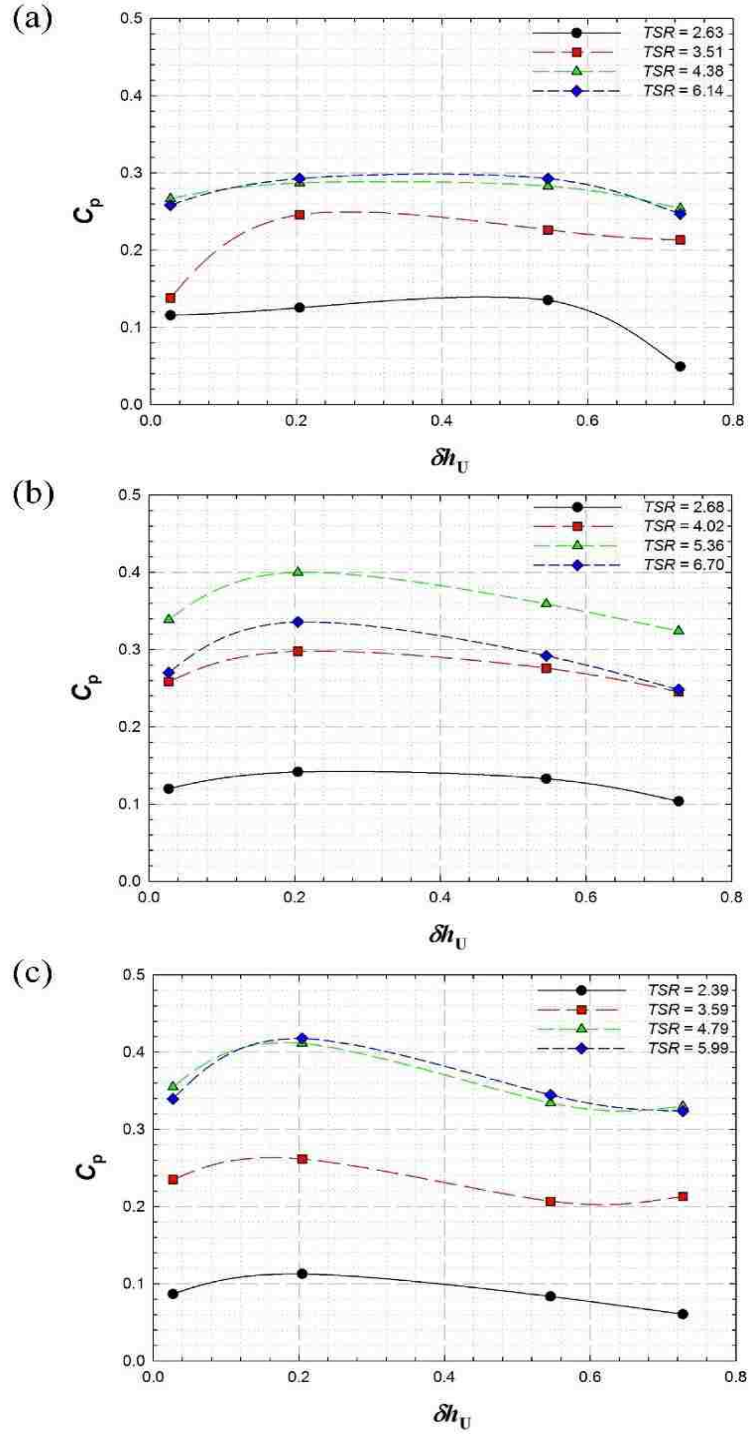
Figure 4.10: Effect of Reynolds number on turbine performance characteristics at various operating *TSR* values and tip clearance ratios: (a) *U*=0.5 m/s (Re_D =1.37$\times$10^5), (b) *U*=0.66 m/s (Re_D =1.8$\times$10^5), and (c) *U*=0.73 m/s (Re_D =2$\times$10^5), where, Re_D is Reynolds number based on turbine diameter

that the optimum installation depth for efficient MHkT operation should be such that, the turbine is submerged with rotor disc $0.5 \times R$ below the water surface and $>1 \times R$ above the channel bottom wall, where R denotes the turbine radius. Thus the optimum depth of water for MHkT installation should be greater than 3.5 times the turbine radius.

4.4.6   Results of Transient CFD to investigate boundary proximity effects

A transient CFD analysis was performed to characterize the flow-field under a free surface, blocked flow environment shows a presence of faster bypass regions and its dependence on boundary proximity. All simulations were run at a constant rotational speed of 200RPM and flow velocity of 0.5m/s (*TSR*=5.85). Four different cases were considered with tip clearance ratios (δh_U) of 0.73, 0.55, 0.20, and 0.03. Figure 4.11 plots contours of stream-wise superficial water velocity normalized by free-stream velocity (*U*=0.5m/s) on a vertical plane passing through the turbine rotational axis for different tip clearance ratios after 5 seconds, i.e. 16.67 rotations. For all cases, the wake region was observed to extend over the entire downstream channel length (~$8 \times R$). For higher depths of immersion (δh_U =0.73, 0.55), tip vortex structures were observed in both upper and lower bypass regions. But with decreasing δh_U (0.20 and below), the tip vortices start to interact with the free surface and dissipate before propagating downstream the turbine. A significant free surface drop was observed behind the turbine rotation plane with free surface penetrating into the wake region (Figure 4.11d). Figure 4.11 also plots contours of stream-wise superficial water velocity normalized by free-stream velocity (*U*=0.5m/s) on a horizontal plane, passing through the turbine rotational axis for different tip clearance ratios.
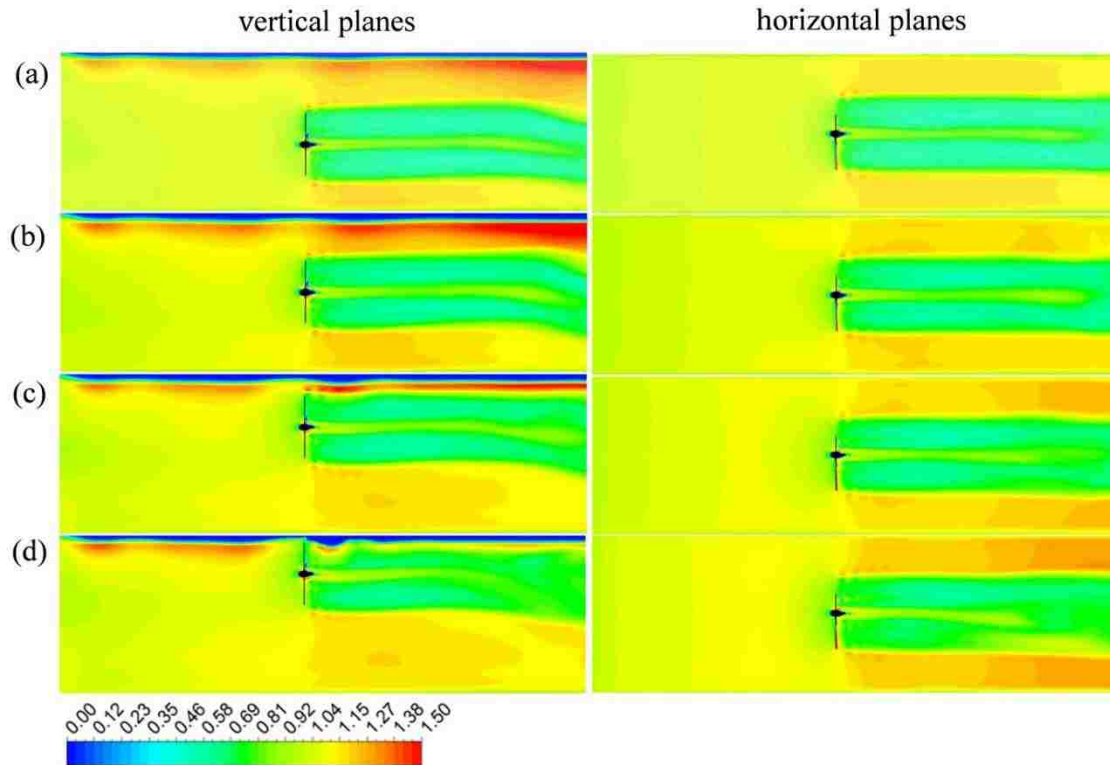
Figure 4.11: Normalized stream-wise superficial (water) velocities on centerline vertical (left column) and horizontal (right column) planes after t=5sec for δh_U of (a) 0.73. (b) 0.55, (c) 0.20 and (d) 0.03

The same color-map scale is used for both vertical and horizontal planes to elucidate the difference in velocity variations between these two planes. The upper bypass region shows significantly higher velocities compared to lower bypass and bypass regions on either sides of turbine in horizontal planes. The contour plots on horizontal planes, as opposed to the vertical planes (in Figure 4.11) show more symmetric wake and bypass region. Tip vortices and their merging with the main wake can be seen on either sides of turbine axis. Further, higher stream-wise flow velocities were observed for lower tip clearance ratio, which suggests a presence of faster bypass flow for lower depths of immersion.

Figure 4.11 also point out the effect of blockage and boundary proximity on flow upstream of the turbine. It is to be noted that for CFD simulations, the inlet velocity profile

was defined to be a uniform flow with stream-wise velocity of 0.5m/s. But as the flow approaches the turbine plane, the presence of the turbine was observed to modify the incoming flow as can be seen in Figure 4.11. Similar observations were reported by Medici [48] who observed modifications to flow approaching the turbine up to three diametrical distance upstream, which depended on turbine geometry, and operating conditions. Further the shape of the incoming velocity profile was different for different surface proximity cases which indicates the dependence of incoming velocity field on free surface proximity.

Figure 4.12 presents wake expansion and its interaction with the deformable free surface for tip clearance ratios of δh_U =0.73, 0.20 and 0.03. Contours of normalized instantaneous superficial stream-wise velocity after simulation time t = 5 seconds are plotted on various planes at downstream locations ranging from x=0.1R to x=5R. When the turbine was submerged deep inside the water channel (δh_U =0.73), no significant wake-free surface interaction was observed (Figure 4.12a). However, when the turbine was placed in very close proximity of the free surface (δh_U =0.03), significant free surface deformation was observed that interacted with wake and bypass flow resulting in modifications of downstream flow-structures. Such a close proximity of the turbine to the free surface not only resulted in faster upper bypass flow but also a skewed wake as depicted in Figure 4.12c. For δh_U =0.20, flow acceleration was observed in the upper bypass region without any significant interaction with the wake and lead to maximum turbine performance. For lower depths of immersions (δh_U =0.20 and 0.03), the free surface drop behind the turbine rotation plane provided additional obstruction to the wake propagation and restoration process.
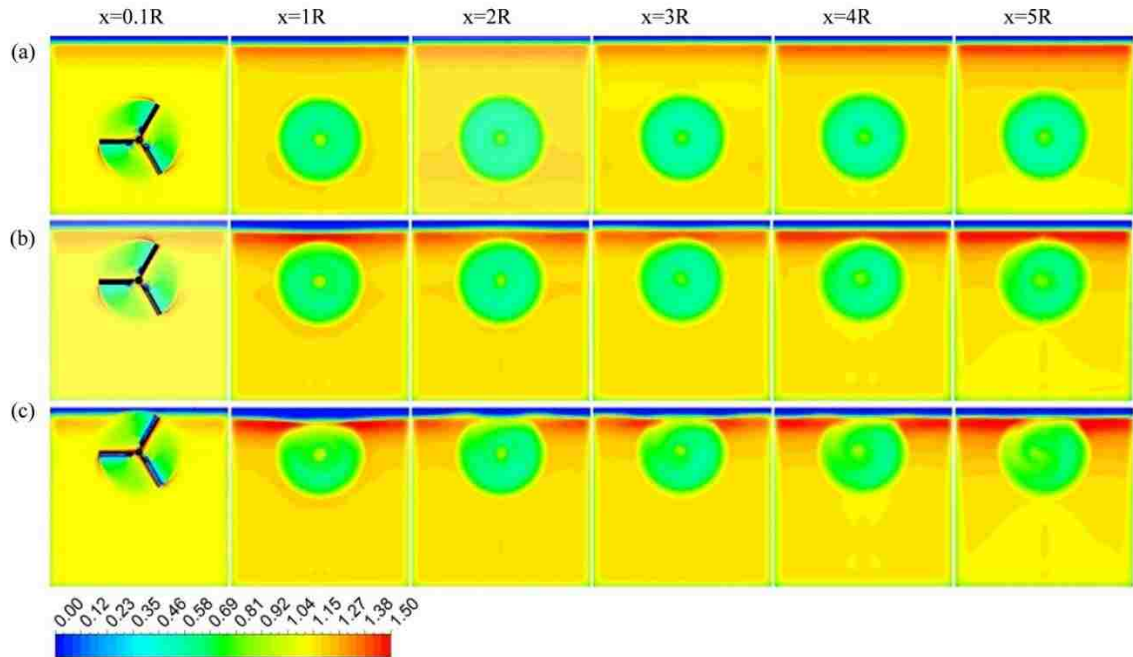
Figure 4.12: Contours of normalized superficial velocity showing bypass and wake propagation at five downstream locations for tip clearance ratios (δh_U) of: (a) 0.73 (b) 0.20 and (c) 0.03

This resulted in a slower moving wake and faster upper bypass region as depicted in Figures 4.11 and 12. For the $\delta h_U =0.03$ case, the wake is almost touching the free surface, so it appears (in Figure 4.4.11) that there is no upper bypass region in a vertical plane aligned with the turbine axis. However, Figure 4.12 which presents a more complete picture of the flow field shows flow acceleration in the upper bypass region (around the wake) for both $\delta h_U =0.2$ and $\delta h_U =0.03$. Thus a closer proximity of the turbine to a free surface retards wake propagation but accelerates the flow in the upper bypass region compared to the case of a deeply submerged turbine. The free surface deformation complements the wake blockage effect (hence total blockage) and yields higher performance for $\delta h_U =0.2$. But, at $\delta h_U =0.03$, the wake starts strongly interacting with the upper bypass region leading to a skewed wake and lower performance. It is to be noted

117

here, that for all the tip clearance ratios considered during present study, CFD analysis did not show a presence of any flow separation on turbine blades. This alludes to the fact that the free surface deformation is the primary mechanism for increased or reduced performance at close proximity.

Furthermore, Figure 4.11 also depicts the variation of free surface height along the length of the channel. The difference in heights (free surface drop) is more pronounced for the δh_U =0.03 case compared to the δh_U =0.73 case. This was also observed during experimental investigations which showed the presence of complex three dimensional structures and free surface drop behind turbine when it was operated in close proximity to a free surface. A free surface drop up to 5% to 10% of channel depth was observed around $1 \times R$ behind the turbine and this water surface drop was at its peak when the turbine was operated at closest proximity to a free surface. Figure 4.13 obtained from transient simulations, shows the free surface of the water channel colored by normalized drop (free surface drop/channel depth) for various depths of immersions. Maximum free surface drop was observed when the turbine was in closest proximity of a free surface (δh_U =0.03). Further, shape of the free surface drop curve was observed to be a function of depth of submersion. It is to be noted that contours in Figure 4.13a-d are colored by a normalized free surface drop ($\Delta h/h_1$), however the color-map scale for each case is chosen to elucidate the three dimensional structure of the free surface drop for respective cases. When the turbine was away from a free surface, the free surface drop curve was a two dimensional structure showing distinct bands before and after the turbine rotation plane. But with closer proximity to a free surface, these bands started to contract to a localized region. For δh_U =0.73 a free surface drop of up to 5% of the total channel depth was observed on the

118

downwind side of the turbine rotation plane. With decreasing depth of submersion, the free surface drop on the upwind side of the turbine started diminishing relative to a localized three dimensional structure behind the turbine rotation plane. For $\delta h_U = 0.03$, a free surface drop of up to 8% of the total channel depth was observed when the turbine was placed in close proximity of free surface.
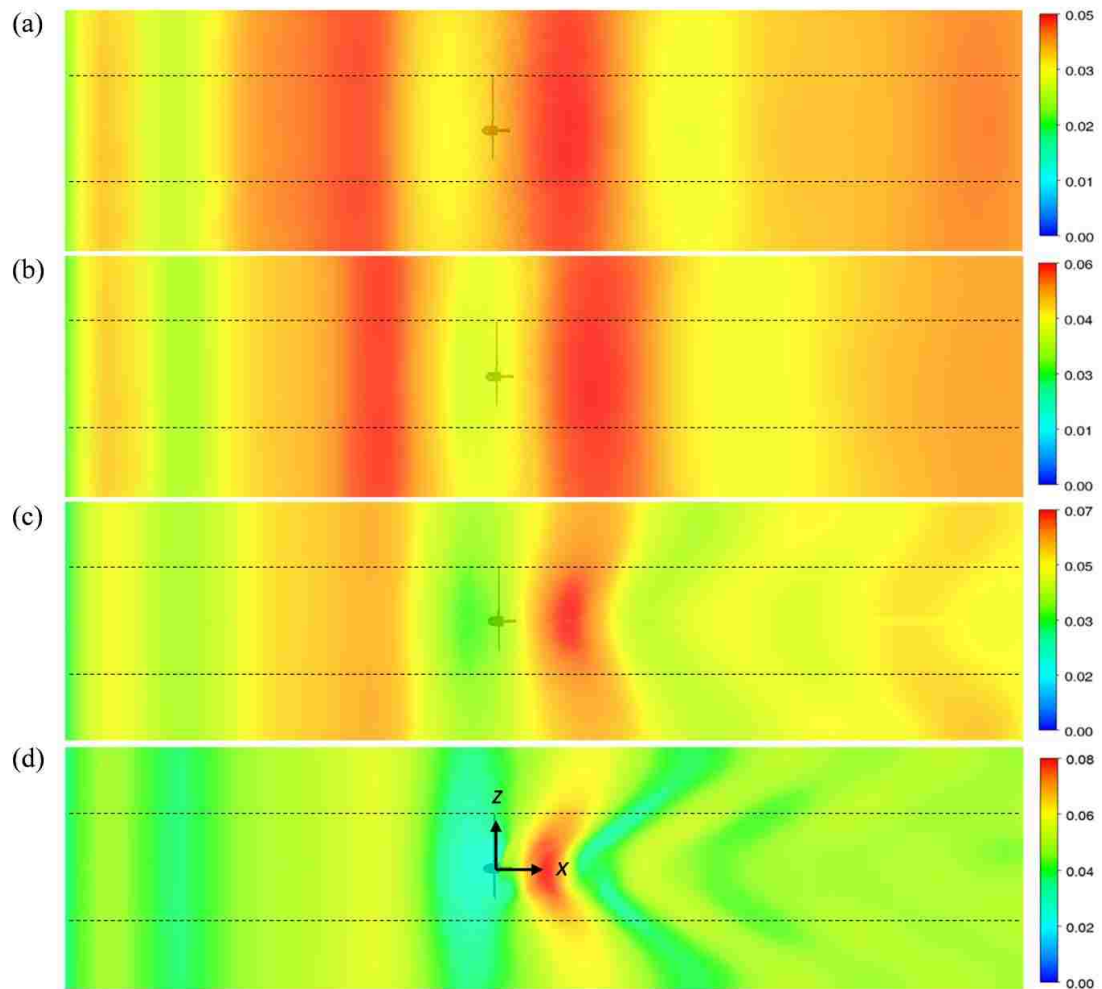
Figure 4.13: Contours of free surface colored by normalized free surface drop $\Delta h/h_1$ for tip clearance ratios (δh_U) of: (a) 0.73 (b) 0.55, (c) 0.20, and (d) 0.03. For relative location of the turbine, please refer to Figure 4.4.

4.5 CONCLUSION

The results of the experimental and computational analysis for blockage effects, the Reynolds number dependency and boundary proximity effects on flow-field and performance of a MHkT are presented. Experiments were carried out on a lab-scale MHkT at various flow velocities inside a 0.61m×0.61m test section, open surface recirculating water channel. The CFD predictions based on rotating reference frame technique were in agreement with experimental data. CFD study was further extended to understand the effect of the flow Reynolds number and blockage ratio on turbine performance characteristics. Increasing flow velocity resulted in improved performance until 0.7m/s beyond which a C_p vs. *TSR* curve was found to be insensitive to the Reynolds number change. Further, the effect of solid blockage on the turbine performance was analyzed by varying the size of fluid domain for lab prototype model. Blockage ratio below 10% did not show any appreciable effect on turbine performance characteristics. Increasing the solid blockage ratio from 10% to 42% resulted in widening the operating *TSR* range with up to ~35% improvement in the power coefficient. Higher *TSR* values were found to exhibit higher blockage effects (higher percentage increase in C_p compared to unblocked case) due to faster rotational speed that lead to stronger wake and faster bypass flow. Further, to understand effect of surface proximity on turbine performance and flow-field, experiments were carried out with the turbine at different depths of immersion. An improvement in performance was observed when the turbine axis was moved away from the channel bottom (channel bottom wall to blade tip clearance > turbine radius). This trend continued until the turbine was raised to a tip clearance of half radius distance below the free surface, after which reduced performance was observed. Beyond this height, appreciable free surface

drop was observed behind the turbine rotational plane restricting the wake expansion and propagation process resulting in reduced performance. A three dimensional transient CFD analysis (with VOF formulation) that was performed for wake and near-free surface flow characterization revealed the presence of three distinct flow regions behind the turbine: wake, upper bypass and lower bypass region. The flow structures in these regions were found to depend strongly on the proximity to the channel bottom and free surface. For lower tip clearance ratios, a significant drop (up to 5 to 10% of channel depth) in free surface was also observed behind the turbine, with complex three dimensional flow structures that lead to a skewed wake affecting its expansion and restoration process. Further, a reduction in performance was observed when the turbine was operated close to the channel bottom wall. This can be attributed to two facts: first, the boundary layer and associated viscous effects at the channel bottom wall that adversely affect the turbine performance, and second, the absence of additional blockage due to free surface deformation that manifests when a turbine operates in proximity of a free surface. Since both distances were varied simultaneously, it is not possible to pin down the cause to either of the cases described above. Free surface deformation and higher flow velocities in the upper bypass region (compared to lower bypass region) lead to an asymmetric wake behind the turbine. Transient CFD analysis at *TSR*=5.85, for all depths of immersion, studied during present work did not show any flow separation effects on turbine blades suggesting that, free surface deformation is the primary mechanism for increased or reduced performance of the turbine operating in a free surface proximity environment. In addition to the wake and bypass regions behind the turbine, the presence of turbine in flow channel was observed to affect flow upstream of the turbine as well. Our experimental

investigations suggest that for optimum performance, the MHkT should be installed such that, the turbine rotational disc is at least one radial distance away from the solid channel wall and half the radial distance below the free surface.

CHAPTER 5

EXPERIMENTAL INVESTIGATIONS OF NEAR-WAKE FIELD FOR A MARINE HYDROKINETIC TURBINE IN A FREE SURFACE ENVIRONMENT

5.1 BACKGROUND

Marine hydrokinetic turbines (MHkT) operate in an environment where the water velocity and water level above the turbine rotation disc undergo cyclic variations [22]. Therefore, for an efficient operation of MHkT, it is crucial to understand the effect of these fluctuations on its performance characteristics. Like wind turbines, MHkT blades are made from airfoil sections and any change in flow velocity modifies its lift/drag characteristics which affects the turbine performance. In addition, the restriction offered by the turbine rotation disc to the freestream flow, referred to as blockage, results in flow acceleration around the turbine. The total blockage can be thought of as a combination of solid blockage and wake blockage. While the solid blockage depends on the area of turbine rotation disc relative to the tidal channel (or river bed) cross section area; the wake blockage is an add-on and primarily due to flow obstruction imposed by a counter-rotating wake that expands and dissipates behind the turbine. Though the solid blockage is constant for a given turbine and channel cross-section area, the extent of the wake blockage varies with flow speed and turbine rotation speed. If tip speed ratio (TSR = ratio of flow speed at blade tip to channel flow speed) is held constant at the design TSR value, an increase in flow velocity implies increased rotational speed; the higher the turbine rotation speed, the stronger the wake behind the turbine which leads to higher wake blockage which further improves the turbine performance. Hence, for similar TSR values, turbine performance is different at different flow speed and rotation speed combinations [35, 51, 54]. Thus, the variation in performance with the flow speed (and the rotational speed) may be due to variation in the Reynolds number or due to enhanced wake blockage or a combination both.

The effect of blockage on turbine performance has been experimentally and analytically investigated by many researchers [1, 5, 13-15, 21, 48, 55, 57, 61]. The majority of the early experimental work was done either in wind or water tunnels with the aim of validation and verification of simple physics based models of such flows [5, 13-15, 48, 52, 55, 57]. Analytical models for characterizing the turbine performance in blocked environment are based on the application of a linear momentum theory [21, 61]. Chen and Liou [5] experimentally investigated the effects of tunnel blockage on turbine performance. Blockage effect was quantified in terms of the blockage factor by measuring tunnel flow velocity with and without the turbine. The blockage factor was found to be strongly related to solid blockage, *TSR*, and blade pitch angle. The higher blockage effects were observed at higher values of solid blockage and *TSR*. McTavish *et al.* [14] studied the effect of blockage on initial wake expansion for different sized rotors in a water channel using the dye visualization technique. Higher blockage was found to narrow down the wake expansion and modify the vortex pairing behind the turbine. The presence of the turbine in a tidal channel, not only affect the downstream flow but also the flow upstream of the turbine. Experimental and computational investigations of Medici *et al.* [48] show the influence of blockage on the flow up to three turbine diameters upstream of the rotor plane. The near upstream flow showed three dimensional flow structures indicating effect of turbine geometry on the incoming flow, similar to the near wake flow.

In addition to wake blockage, when the MHkT is installed in a near-free surface environment to take advantage of higher flux near the free surface, they may be subjected to additional blockage due to free surface deformation [54]. The proximity of the turbine to the free surface provides additional restriction to the flow by compressing the wake flow

125

in a radial direction. Several studies have also been performed to analyze the effect of free surface proximity on turbine performance using porous discs to replicate the turbine rotors [13, 54-57]. Myers & Bahaj [55] carried out experiments with mesh discs to study the effect of disc proximity to sea bed andwater surface on wake structures behind porous discs. Varying the disc proximity to sea/bed and water surface was found to affect wake structure and its recovery duration. Bahaj *et al.* [56] performed both analytical and experimental studies to investigate the effect of surface proximity on turbine performance. Their experiments in a cavitation tunnel and tow tank showed reduction in turbine power with decreasing blade tip-free surface clearance. Experimental investigations by Birjandi *et al.* [57] with a vertical axis hydrokinetic turbine reported improved performance with increasing free surface proximity. Kolekar and Banerjee [54] performed an experimental study to investigate the effect of free surface proximity on MHkT performance characteristics and reported enhanced performance with increasing proximity. The highest performance was observed for blade tip-to-free surface clearance of half turbine radius. Experimental investigations were augmented by steady and transient CFD to quantify effects of blockage ratio and Reynolds number. A transient CFD analysis revealed faster bypass flow (flow region outside the wake) and free surface deformation behind a turbine rotation plane whose magnitude varied with free surface proximity. An increase in flow velocity and/or blockage ratio was reported to enhance the turbine performance.

Flow visualization techniques, based on dye and particle image velocimetry (PIV) have been used by many researchers to identify the flow features in the wake of wind turbines and marine hydrokinetic turbines. Chamorro *et al.* [58] performed three dimensional PIV study in the wake of a miniature axial-flow hydrokinetic turbine and

reported wake expansion proportional to the one-third power of the stream-wise distance. Wake rotation was observed up to three rotor diameters, with higher tangential velocities near wake core, and higher radial velocities near turbine tip. Experimental investigations by Whale [59] on a lab-scale wind turbine reported high blockage at the large *TSR* values, due to obstruction offered by a slow moving (stream-wise) wake to free stream flow. A vortex merging and reduced vortex pitch was reported at higher *TSR* values with a plausible occurrence of wake acceleration. Flow visualization was carried out with PIV technique and a comparison was presented with the rotor vortex lattice method which showed good qualitative agreement for wake shape, expansion and tip vortex pitch. Experimental analysis by Manar *et al.* [60] through experimental study on a rotating wing in a confined space concluded that the magnitude of the measured blade forces was dependent on the Reynolds number and blade-to wall tip clearance. The measured lift coefficients were highest for the tip clearance of $0.5c$ (c=chord length $= 0.2R$, R=rotor radius). An increase in tip clearance to $3c$ and $5c$ did not show any effect on force measurements at a low Reynolds number. The test case with $3c$ clearance performed similar to a $5c$ case at low Reynolds number and similar to a $0.5c$ case at an elevated Reynolds numbers. A stronger wall to tip vortex interaction was observed for $0.5c$ case that entrained dye off the wall into the tip vortex path. A slight upward movement of the dye streak (originating from near-wall region) was observed for $3c$ clearance without any entrainment. For a MHkT operating in a near free surface environment, similar phenomena are expected, leading to an increased thrust and torque. However, flow entrainment in this case is expected to result in free surface deformation modifying the near-wake field and its propagation downstream the turbine. The current research is aimed at enhancing our limited knowledge about the flow

127

physics and its implication on the turbine performance in a free surface proximity environment.

Analytical models to characterize the turbine performance in a free surface-blocked environment are based on linear momentum theory. Garrett and Cummins [61] applied this momentum theory for flow constrained between two rigid surfaces and found increase in turbine power with increasing blockage ratio. Houlsby *et al.* [21] presented an application of the linear momentum theory to analyze performance in various finite flow domain scenarios: pressure constrained, parallel-sided tube and open channel flow. A quartic equation was presented relating the flow Froude number (ratio of characteristic flow velocity to gravitational wave velocity), blockage ratio, and flow speeds in wake and bypass region behind turbine. Whelan *et al.* [21] presented blockage correction to blade element momentum predictions for prediction of turbine performance in a blocked-free surface environment. Analytical predictions were comparable with experimental data for mesh disc simulator and two bladed rotor in wind tunnel and water channel for different blockage conditions. Lartiga and Crawford [52] used actuator disc modelling with blockage corrections to predict the performance of a tidal turbine in a blocked environment. Flow field data from PIV measurements and CFD simulations were used to account for blockage effect. Analytical predictions were in good agreement at lower blockage ratios but showed significant deviations at higher blockage ratios. Computational study with porous discs by Sun [53] reported localized flow acceleration in the region between the wake and the channel bottom. Free surface drop behind mesh disc was observed to affect both wake characteristics and turbine performance as well. Consul *et al.* [15] investigated the effect of blockage and free surface deformation on the performance of a marine cross-

128

flow turbine for different blockages and free surface boundary conditions using two-dimensional CFD modelling. The deformable free surface boundary condition lead to a 6.7% performance improvement compared to the closed top condition due to a higher effective blockage caused by the free surface deformation. The Froude number (over the range studied: 0.08 to 0.13) was reported to have a very small effect on the power coefficient (henceforth referred to as C_p = ratio of power extracted to water power available), but significantly affected the free surface drop.

The majority of the earlier reported experimental investigations attempting to quantify the effect of blockage on turbine performance are limited to a turbine operating at either a single flow speed, and/or single depth of immersion; very little is known about the effect of free surface proximity on performance and flow dynamics of MHkT. In this manuscript, we report the first experimental study to understand the effect of free surface proximity, and flow velocity on a MHkT, through system level measurements that include thrust and torque to quantify turbine performance, as well as detailed flow-field visualization using a stereoscopic particle image velocimetry technique. The principle objective of current work is to contribute towards understanding the influence of free surface proximity and flow velocity on blockage effects which are quantified in terms of increase in flow velocity, increase in power and thrust coefficient. The detailed flow-field visualization allows to identify the principle flow mechanisms that are responsible for variation in performance with variation in turbine depth. Experimental investigations are conducted on a three bladed, constant chord, zero twist hydrokinetic turbine in an open surface water channel with a test section of 0.61m × 0.61m cross section. The turbine was subjected to various flow speeds, rotational speeds and depth of immersions. The torque

and thrust data was obtained from a submerged torque-thrust sensor connected in-line with the turbine axis. Experimental data was corrected to unblocked dataset, using a blockage correction methodology, based on actuator disc theory for a finite domain with a constant volume (representative of a closed top wind/water tunnel) [1, 13]. In addition, a modification to finite domain-constant volume blockage correction is presented to incorporate free surface effects, which is a better representation of current open channel experiments (please refer to §2.5 for details of blockage correction methodologies). A comparison is presented between unblocked data (from both methods), and blocked experimental data at various flow velocities, rotational speeds and depths of immersion. Further, to identify the flow structures associated with wake blockage and free surface deformation, a quantitative flow visualization was carried out with stereo-PIV technique in the near-wake region of MHkT. This chapter is organized as follows: section 5.2 presents an experimental set-up and facility used for current study. In section 5.3, results from experimental investigations are discussed. A comparison of various cases is presented in section 5.3.1 to demonstrate the effect of Reynolds number and free surface proximity on blockage effects in terms of enhancements in flow velocity, power coefficient and thrust coefficient. Sections 5.3.2-5.3.9 are devoted to address mechanisms which govern this variation (described in §5.3.1), wherein, results from stereo-PIV visualization are presented for different rotational speeds and depths of immersions.

5.2   FACILITY, EXPERIMENTAL SET-UP AND MODEL PROTOTYPE

All experiments were carried out in an open surface recirculating water channel at Lehigh University with a test cross-section size of 0.61m × 0.61m, and length of 1.98m (Engineering Laboratory Design, USA). This facility is equipped with a 25HP single stage

130

axial flow propeller pump, with maximum discharge of 21,160 liters/min. The propeller

pump rotational speed and hence the test section flow velocity is controlled and regulated

through a transistor inverter type variable frequency controller (Toshiba Model VFAS1-

2185PM-HN). Flow velocity can be varied from 0.03m/s to 0.94m/s and controlled within

an accuracy of $\pm$ 2%. The flow conditioning upstream of the test section was such that the

turbulence intensity (ratio of root-mean-square of the turbulent velocity fluctuations to

mean channel velocity $= u'/U_1$) across the test section is less than 1%. The model prototype

used for current study is a three bladed, 0.14m radius (R), zero twist, constant chord blade

turbine made from corrosion resistant aluminum alloy (Figure 5.1).

Figure 5.1: Photograph of turbine prototype used for current study [R=0.14m]

Turbine blades are formed from a SG6043 airfoil profile on a five-axis CNC machine.

Turbine blades are held together inside a two-part hub and their orientation can be changed

to adjust the blade pitch to the desired angle. During current experimental campaign, all

experimental runs were performed with turbine blades oriented at 10° blade pitch. The

choice of 10° blade pitch was governed by our earlier computational and analytical fluid-

structure interaction study [51], with a full scale prototype (R=1m) which showed high

structural and hydrodynamic performance around 10° blade pitch. The turbine prototype, when operated in our facility, leads to area based blockage ratio (*B*) of 0.165.

The experimental setup, which is shown in Figure 5.2, consisted of a lab scale model hydrokinetic turbine attached to a horizontal shaft which was driven by a stepper motor which maintains a precise rotational velocity through a micro-stepping driver and controller mechanism. The stepper motor used for current study was the NEMA23 series, 24VDC motor with resolution of 1600 micro-steps per revolutions (Model # 23MDSI, Anaheim Automation Inc.). The stepper motor was connected to the turbine shaft through a flexible coupling. The motor and flexible coupling were enclosed inside a watertight acrylic cylinder, which was then connected to a thrust torque sensor (Model # TFF400, Futek Inc.). The acrylic cylinder was continuously pressured/purged to avoid water leakage into the system. The reaction torque-thrust sensor was fixed to a vertical post, which was connected to a horizontal frame supported at channel top. The vertical post can be raised/lowered inside the water channel to vary the distance between the turbine and the free surface.
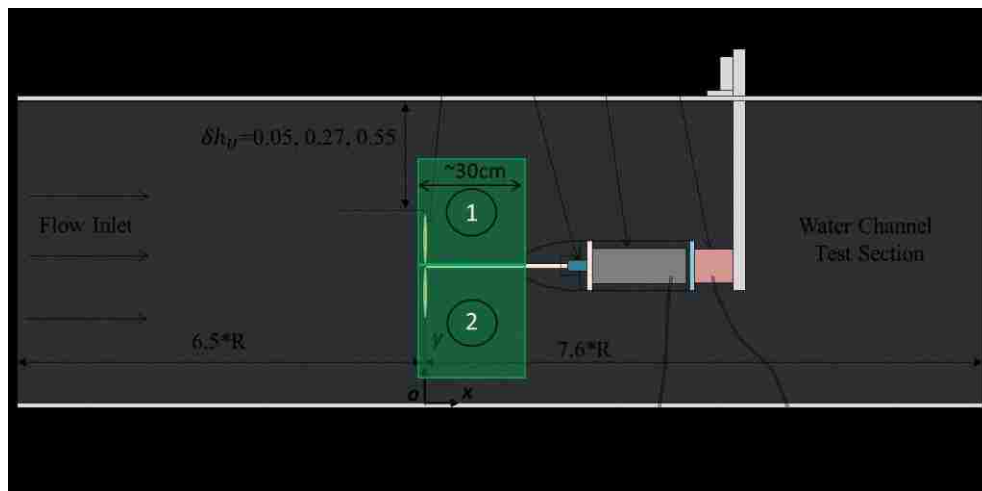
1 – Turbine, 2 – Flexible Coupling, 3 – Motor, 4 – Thrust-Torque Sensor,
5 – Support Structure, 6 – To Motor Controller, 7 – To Data Logging

Figure 5.2: Schematic of experimental set-up showing location of field of view for current study [R=0.14m]

During an experimental run, data from torque-thrust sensor was continuously monitored and acquired at high sampling rate of 500 samples/second for the duration of 60 seconds per run for further analysis. Figure 5.3 plots the convergence of experimental measurements with time. The time averaged data (average of accumulated data before a given instant of time) is plotted against measurement time for thrust (Figure 5.3a) and torque (Figure 5.3b).
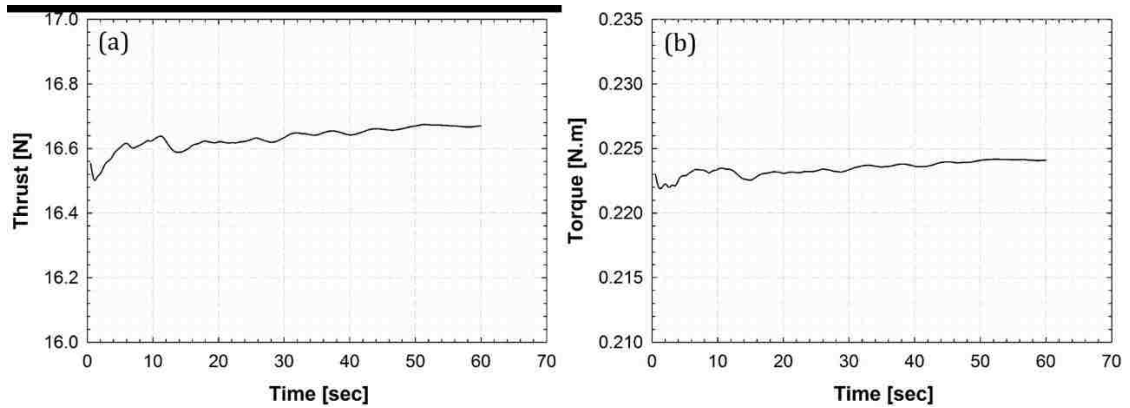
Figure 5.3: Convergence of experimental data from (a) thrust and (b) torque measurements

Table 5.1: Flow variables and turbine depths of immersions investigated during current experimental study

Flow Velocity U_1 [m/s]	Re_{Chord} (U_{tip}, TSR=5)	$Re_{Diameter}$	Froude number	Tip clearance ratio (δh_U)
0.3	2.5×10^4	8.2×10^4	0.12	
0.5	4.1×10^4	1.4×10^5	0.20	0.05, 0.27, 0.55
0.7	5.7×10^4	1.9×10^5	0.29	
0.8*	6.6×10^4	2.2×10^5	0.33	

*SPIV investigations were performed for a channel flow velocity of 0.8m/s with laser sheet parallel to XY plane at Z$\cong$ 0.1R, that corresponds to a blade root location (see Figure 5.2)

The torque/thrust sensor was accurate to within $\pm$ 1% for current measurement range (torque $<$ 0.4N.m, thrust $<$ 35N). A single sample uncertainty analysis for channel velocity, RPM, and torque based on Kline and McClintock [77] showed maximum uncertainty of 1% on *TSR* and 3% on C_p measurements. Table 5.1 presents details of experimental runs carried out during current study.

5.3 RESULTS AND DISCUSSION:

Results from experimental investigations carried out on a constant chord, untwisted three bladed MHkT are discussed. Experiments were performed with a turbine operating at various flow velocities and immersion depths over a range of *TSR* values. The flow Reynolds number (based on free stream velocity and chord-length) was varied from 6.7×10^3 to 3×10^4 which corresponded to channel flow velocity (U_1) variation of 0.2m/s to 0.9m/s to quantify its influence on blockage effects. Experiments were performed with turbine rotating at various rotational speeds [30, 360] RPM to achieve complete bell shaped C_p vs. *TSR* curve. The rotation rate of the turbine was precisely controlled by a stepper motor that also helped avoid turbine blade stalling at higher angles of attack. Additionally, to understand the effect of free surface proximity on blockage effects, experimental runs were performed with a turbine operating at various depths of immersions. The free surface proximity is expressed in terms of tip clearance factor, $\delta h_U = {h_U}/{D}$, where, h_U represents water depth between turbine rotation disc and free surface and D represents turbine diameter. Experimental data was corrected to free-stream velocity-unblocked dataset by incorporating blockage correction methodology based on closed-top formulation. A comparison is the presented between blocked and unblocked data for flow velocity, power coefficient, thrust coefficient and blockage factors to quantify the blockage effects at

134

various Reynolds numbers and tip clearance factors. Additionally, an open surface blockage correction formulation was applied to experimental data and a comparison is presented between two methodologies.

5.3.1 Results of experimental investigations for performance (thrust and torque) measurements

5.3.1.1 Measured thrust data for various flow velocities and depths of immersion:

The thrust loading on the turbine was continuously recorded from a submerged thrust sensor placed in-line with the turbine on a desktop computer. Figure 5.4a presents thrust force plotted against flow velocity for different rotational speeds – 90, 180, 270 RPMs at δh_U of 0.55. As expected, an increase in flow velocity lead to an enhanced thrust loading on the turbine. For a given flow velocity, higher the rotational speed, larger the thrust value due to higher effective solidity. Further, the difference between measured thrust forces at various rotational speeds increased with increasing flow velocities as shown in Figure 5.4a. To identify the effect of free surface proximity on thrust force, variation of turbine thrust force with flow velocity at various δh_U cases are plotted in Figure 5.4b. For all depths of immersions, thrust forces increased with increasing flow speed and rotational speed. For all flow velocities, the case with δh_U=0.27 resulted in the highest thrust forces, with δh_U=0.55 and δh_U=0.05 cases showing almost similar values except for the high rotational speed of 270 RPM. For low rotational speed values (*TSR*<3) no significant variation was observed between measured thrust forces. With increasing *TSR* values, thrust forces between various δh_U cases started deviating from each other with maximum deviation observed for the highest velocity and RPM case. This variation of thrust force with flow velocity and depth of immersion forms the basis for blockage effect evaluation.

The experimental thrust data was then used to correct measured flow velocity, torque, *TSR*, and thrust forces to obtain corresponding values in an unblocked environment and is discussed in subsequent sections below.
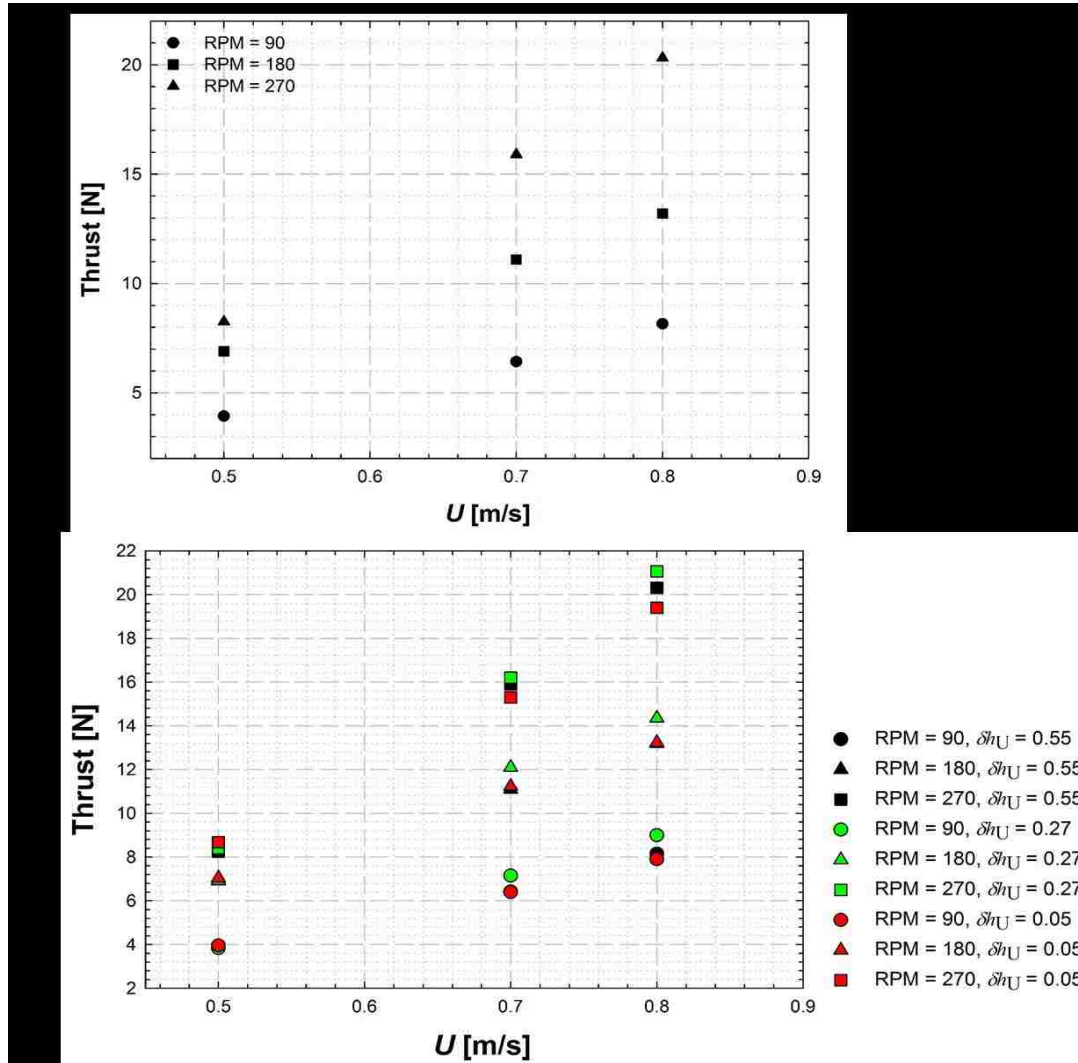
Figure 5.4: Variation of measured thrust with flow velocity at rotational speeds of 90, 180, 270 RPM (a) For $\delta h_U = 0.55$, (b) Comparison between various δh_U cases

5.3.1.2 Influence of Reynolds number on blockage effects:

Figure 5.5a (left column) presents the effect of Reynolds number on measured turbine performance over a range of *TSR* values for δh_U of 0.55 which corresponds to the

136

turbine in a water channel such that its axis is at the channel center. C_p vs. *TSR* curves are

plotted for flow velocities of 0.3, 0.41, 0.5, 0.525, 0.55, 0.7, and 0.8m/s which correspond
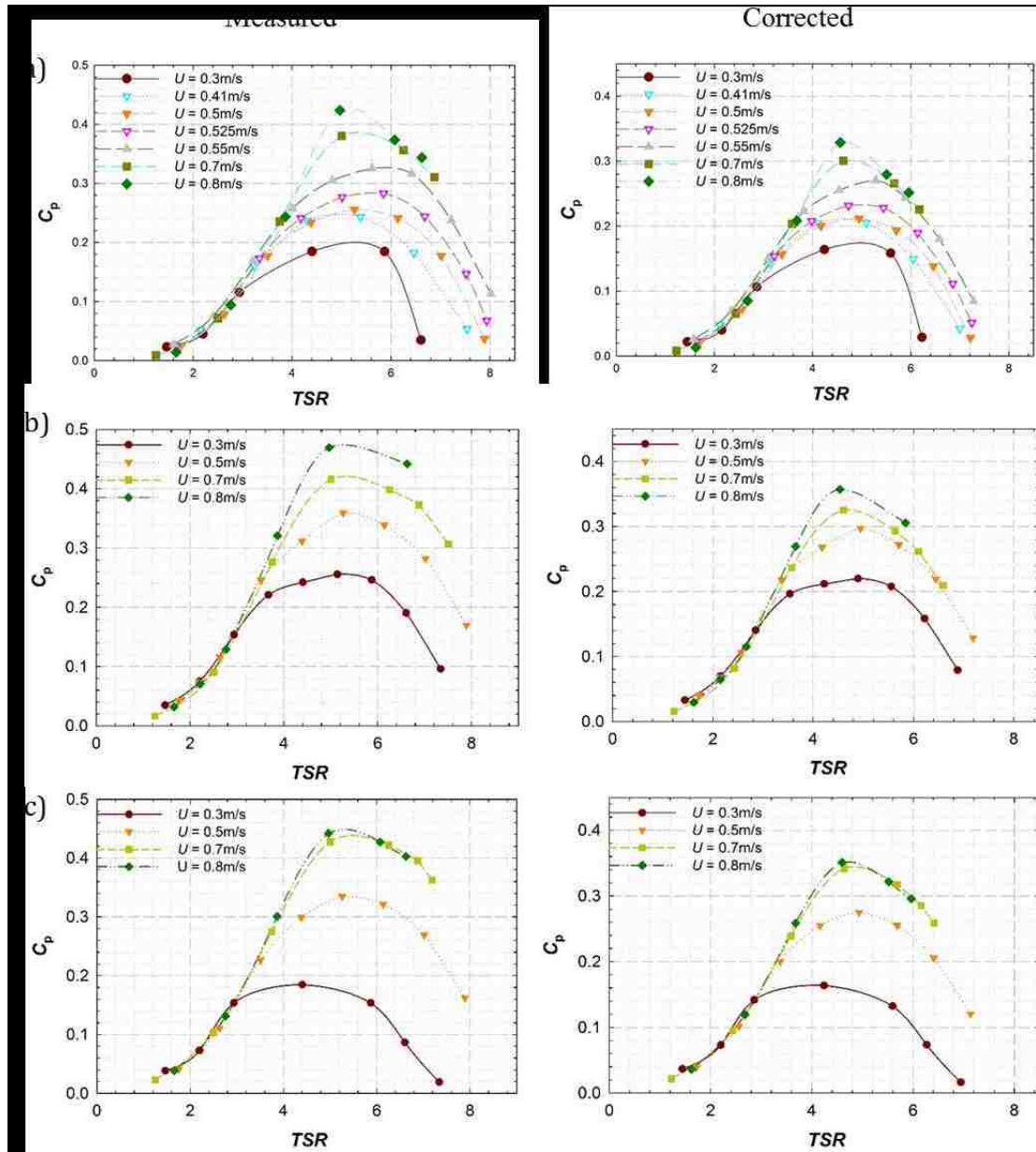
Figure 5.5: Left column: Variation of power coefficient (measured) with TSR for δh_U of
(a) 0.55, (b) 0.27, and (c) 0.05 Right column: Variation of corrected power coefficient
with corrected *TSR* for δh_U of (a) 0.55, (b) 0.27, and (c) 0.05

to the Reynolds number (based on turbine diameter) of 8.4×10^4, 1.15×10^5, 1.4×10^5, 1.47×10^5, 1.54×10^5, 1.7×10^5, 1.96×10^5, and 2.24×10^5 respectively (see Table 5.1 for details of experimental conditions). Increasing Reynolds number from 8.4×10^4 to 1.15×10^5 resulted in improved performance due to higher lift coefficients of SG6043 airfoil used for current turbine blades. However, increasing the Reynolds number from 1.15×10^5 to 1.4×10^5 did not result in any significant performance improvement. This is attributed to the fact that the SG6043 airfoil exhibits a laminar separation bubble formation in this Reynolds number range. Beyond Re_D of 1.4×10^5 the turbine performance resumes improving with increasing Reynolds number. The improvement in C_p started to diminish around Re_D of 2×10^5 beyond which C_p vs. *TSR* curve started to coincide irrespective of increase in the Reynolds number (except for the highest C_p point).

Figure 5.5a also presents a comparison between actual experimental data (raw-blocked data, on left), and corrected (unblocked, on right) data. The blockage correction is observed to shift the entire curve in a southwest direction, decreasing the *TSR* (proportional to the change in flow velocity between blocked and unblocked cases) and C_p values (proportional to the cube of change in flow velocity between blocked and unblocked cases). It is to be noted that all the cases discussed in this manuscript have a constant solid blockage ratio of 0.165. For a given flow velocity (Reynolds number), no significant difference was observed between measured and corrected C_p for *TSR*<3, indicating negligible blockage effects at low rotation speeds. As the *TSR* increased beyond 3, the blockage started altering the measured power yielding higher values compared to the unblocked case. This trend continued until a maximum *TSR* case experimented during the current study. Further, increasing the Reynolds number resulted in higher percent change in C_p indicating higher

blockage effects. A higher Reynolds number (i. e. higher flow velocity) means higher rotational speeds if the *TSR* is to be maintained. Thus, cases with higher *Re* corresponds to faster rotating turbine which leads to stronger wake region behind a turbine offering a higher wake blockage. The percentage change in C_p was found to be (almost) linearly increasing with *TSR* for lower *Re*, however, at a higher *Re* and higher *TSR*, higher order (quadratic or cubic) variation was observed.

5.3.2   Effect of free surface proximity on blockage:

In the previous section, experimental data was presented for demonstrating the influence of flow velocity on blockage effects. An increase in the Reynolds number and associated rotational velocity to maintain the *TSR*, resulted in higher blockage effects leading to higher turbine performance. This section presents the results of an experimental campaign that was carried out to study effect of free surface proximity on the turbine performance and associated blockage effects. During these experiments, the turbine depth of submersion was varied to achieve different tip clearance ratios: $\delta h_U = 0.55, 0.27$, and 0.05. Figure 5.5 compares results of measured experimental data for these three cases. Moving the turbine away from the channel bottom resulted in higher power coefficients due to higher wake blockage effects caused by a deforming free surface behind the turbine. This trend continued until it reached an optimal tip clearance distance beyond which a reduction in performance was observed. Highest performance for all flow velocities was attained for δh_U of 0.27 when turbine is submerged such that the turbine rotation disc is 0.076m (~0.5×*R*) away from the free surface. In this case, a radial compression of wake caused by the free surface drop complemented the wake blockage that resulted in an improved turbine performance. These results are consistent with our earlier published

dataset [54] which showed the highest performance for δh_U of 0.2 which corresponded to a tip clearance distance of approximately half the turbine radius. Similar observations were reported by Manar *et al.* [60] for a rotating wing in proximity of a solid wall who found that the forces on the wing are related to the tip to wall clearance and the flow Reynolds number.

When the turbine was moved further closer to the free surface, a performance degradation occurred due to penetration of the wake by a significant localized free surface drop behind the turbine that adversely affected the turbine performance. These findings are further supported by the results of flow visualization carried out in the near-wake region of the turbine and are discussed in section 5.3.3. The right column of Figure 5.5 presents C_p vs. *TSR* curves for the corrected data. The blockage correction was found to shift C_p vs. *TSR* curves towards origin in a southwest direction with larger shifts observed at higher flow velocities and *TSR* values. The difference between the measured and the corrected values are the direct implication of blockage effects that varied with *TSR*, flow velocity and tip clearance ratio and is discussed next.

5.3.2.1 Effect of δh_U on percent change in C_p and C_T: blockage correction based on closed-top formulation:

Figure 5.6a (left column) presents the influence of the blockage effects on a percent change in C_p when turbine was placed at different depths of immersion. Relative position of MHkT inside the water channel was found to affect the turbine performance due to variation of blockage effects with depth. At the lower *TSR* values (<3) no significant difference was observed in measured C_p vs. *TSR* curves. However, at the higher *TSR* values, a larger percent change was observed between various Reynolds numbers as well as various δh_U cases. Higher percent change in C_p (with respected to unblocked condition:
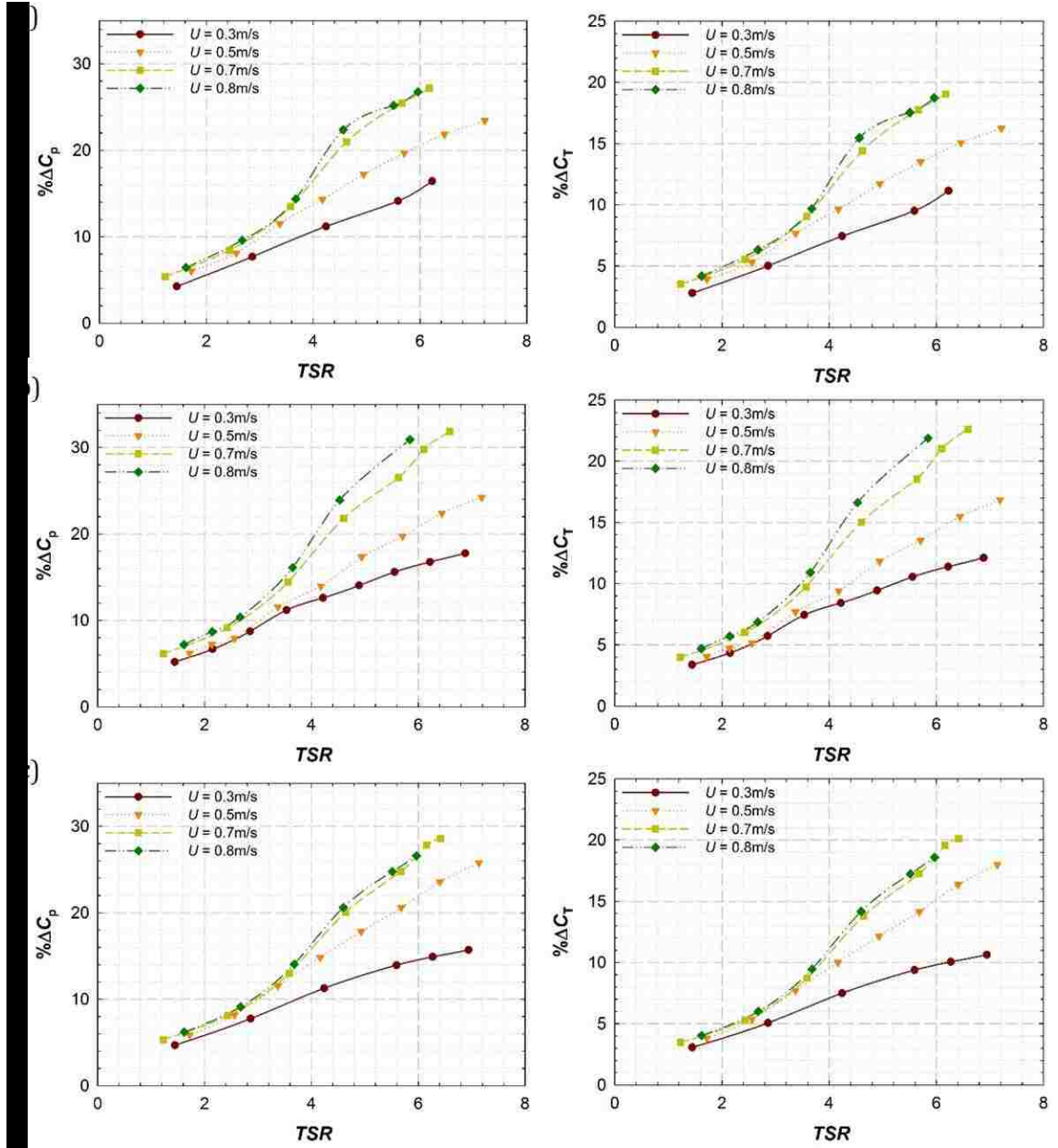
Figure 5.6: Blockage effect as a function of channel velocity, *TSR* and depths of immersion: Percentage change in power coefficient (left column) and thrust coefficient (right column) vs. *TSR* for different tip clearance ratios (δh_U): (a) 0.55, (b) 0.27, and (c) 0.05

$\left[\% \Delta C_p = \left(C_{p\,Measured} - C_{p\,Corrected} \right) / C_{p\,Corrected} \times 100 \right]$ was observed for higher flow velocities,

which for a given *TSR*, correspond to higher rotational speeds leading to higher wake

blockage effects. Further, higher values of rotational speed and flow velocity are also

141

associated with free surface deformation providing additional blockage. The extent of this additional blockage differed in magnitude and inception depending on the free surface proximity. This can be visualized from the slope of %ΔC_p vs. *TSR* curves in Figure 5.6a. For a deeply submerged turbine ($\delta h_U = 0.55$), operating at flow velocities of 0.7m/s and 0.8m/s, additional blockage inception occurred at *TSR*~4.5 and can be visualized by change in the slope of %ΔC_p vs. *TSR* curve. However with an increasing free surface proximity ($\delta h_U = 0.27$ and 0.05), the change in slope became more gradual indicating earlier and gradual inception of the additional free surface blockage. The highest improvement in C_p was observed for δh_U of 0.27 for all flow speeds. Figure 5.6 (right column) which presents an increase in thrust coefficient due to blockage also exhibits a behavior similar to the power coefficients curves. However, thrust force being proportional to square of velocity as opposed to torque which varies with velocity cube, the variations of C_T with flow velocity, *TSR* and tip clearance ratio are lesser in magnitude compared to C_p.

Figure 5.7a plots percentage increase in the flow velocity $\left[\% \Delta U = \left(U_\infty - U_1 \right) / U_1 \times 100 \right]$ due to blockage effect for various flow velocities: 0.3, 0.5, 0.7, 0.8 m/s at $\delta h_U = 0.55$. For a given flow velocity, higher *TSR* values imply a faster rotating turbine leading to a faster rotating wake region resulting a higher wake blockage. Similar to the C_p vs. *TSR* curve, at lower Reynolds numbers, a linear curve relation was observed between ΔU and *TSR* that changed to a higher order curve for a higher Reynolds number. Moving the turbine closer to the free surface (Figure 5.7b and c) resulted in further enhancement in the effective velocity with a maximum improvement observed for the highest flow velocity of 0.8m/s. All tip clearance cases showed similar velocity variations upto *TSR* value of 3, however with increasing rotational speed, larger variation was

observed at *TSR* > 4. For *TSR* of ~5.5, blockage effects lead to upto 9.3% increase in flow velocity for U_1 = 0.8m/s (Re_D = 2.2×10^5, RPM= 330), 6.9% for U_1 = 0.5m/s (Re_D = 1.4×10^5, RPM= 200), and 4.8% for U_1 = 0.3m/s (Re_D = 8.4×10^4, RPM=120) that corresponded to 25%, 19%, and 14% respective enhancements in C_p.
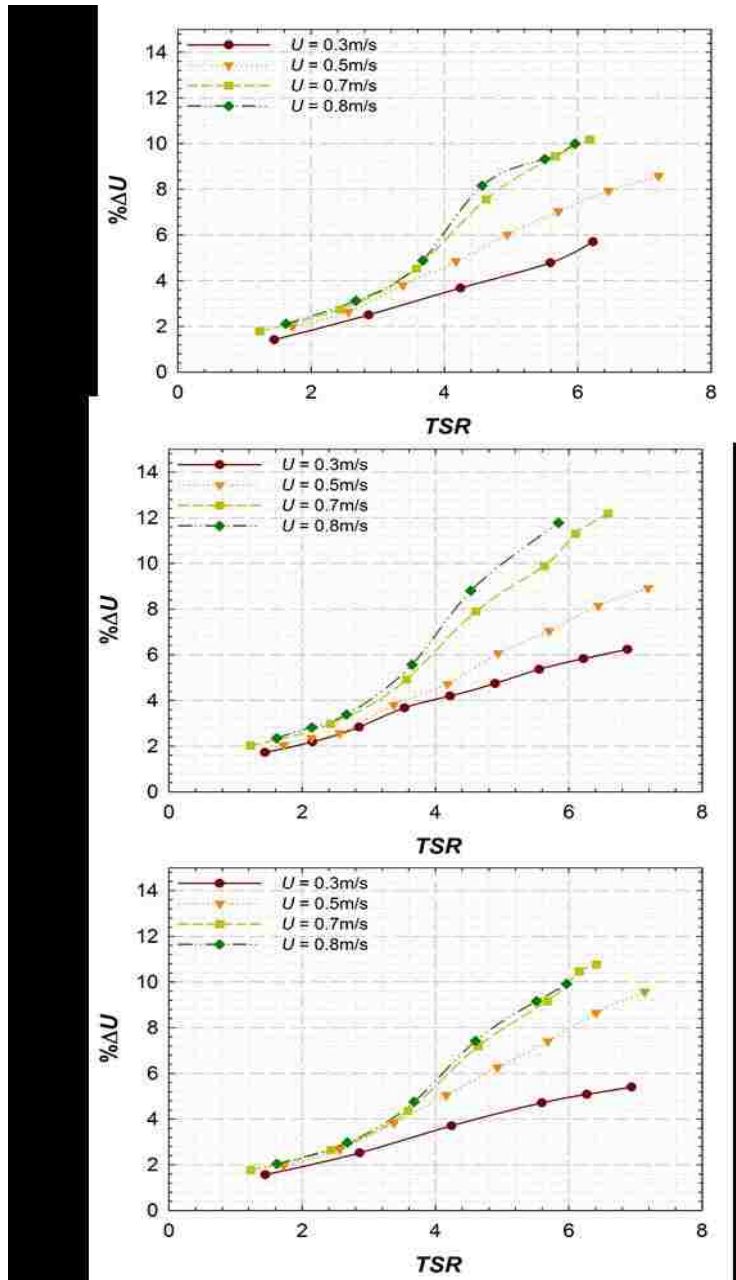
Figure 5.7: Effect of blockage on effective channel velocity: percentage change in *U* vs. *TSR* at various tip clearance ratios (δh_U): (a) 0.55, (b) 0.27, and (c) 0.05

For flow velocity of 0.8m/s, increasing rotational speed from 90RPM to 270 RPM resulted in velocity improvement from 2% to 8.2% which corresponds to C_p improvement of 6.4% to 22.4% respectively. For a constant rotation speed of 270 RPM, increasing flow velocity from 0.5m/s to 0.8m/s resulted in 8.6% and 8.2% increase in flow velocity. Thus the rotational speed has a higher effect on blockage compared to the flow velocity.

To demonstrate the effect of tip clearance ratio on flow acceleration, Figure 5.8 plots variation of power coefficient, increase in power coefficient and increase in effective velocity for channel velocity of 0.8m/s, at different tip clearance ratios for various *TSR* values. As depicted in Figures 5.8a and b, performance for all tip clearance ratio cases was comparable at lower *TSR* values and started deviating around *TSR* ~4 with $\delta h_U = 0.27$ case showing consistently higher C_p and %ΔC_p. Figure 5.8c plots variation of percentage change in effective channel velocity as a function of δh_U for various *TSR* values. At low *TSR* values (1.66, 2.76), when rotational speeds are low, tip clearance ratio did not have any effect on percentage increase in flow velocity. However, at larger *TSR* values (>3.86), %ΔU started varying with depth of immersion. The largest increment in flow velocity was observed for δh_U=0.27. It is to be noted that the actuator disc theory and the blockage correction methodology applied during current study assume a stream tube (control volume) passing through the edge of the disc with uniform loading on disc, steady state flow and no flow across the control surfaces [68, 101]. During present study, for a turbine operating in close proximity of free surface, the deformation of free surface is expected to change the shape of this stream tube behind the turbine rotation plane (and is illustrated in section 5.3.3.1 later). However, this does not invalidate the use of actuator disc model as deforming stream tube will modify both thrust and torque field on turbine blades. As the

correction is based on measured thrust data (which reflects the deformation effects), it is expected to take care of modifications in disc loading due to variation of stream tube shape.
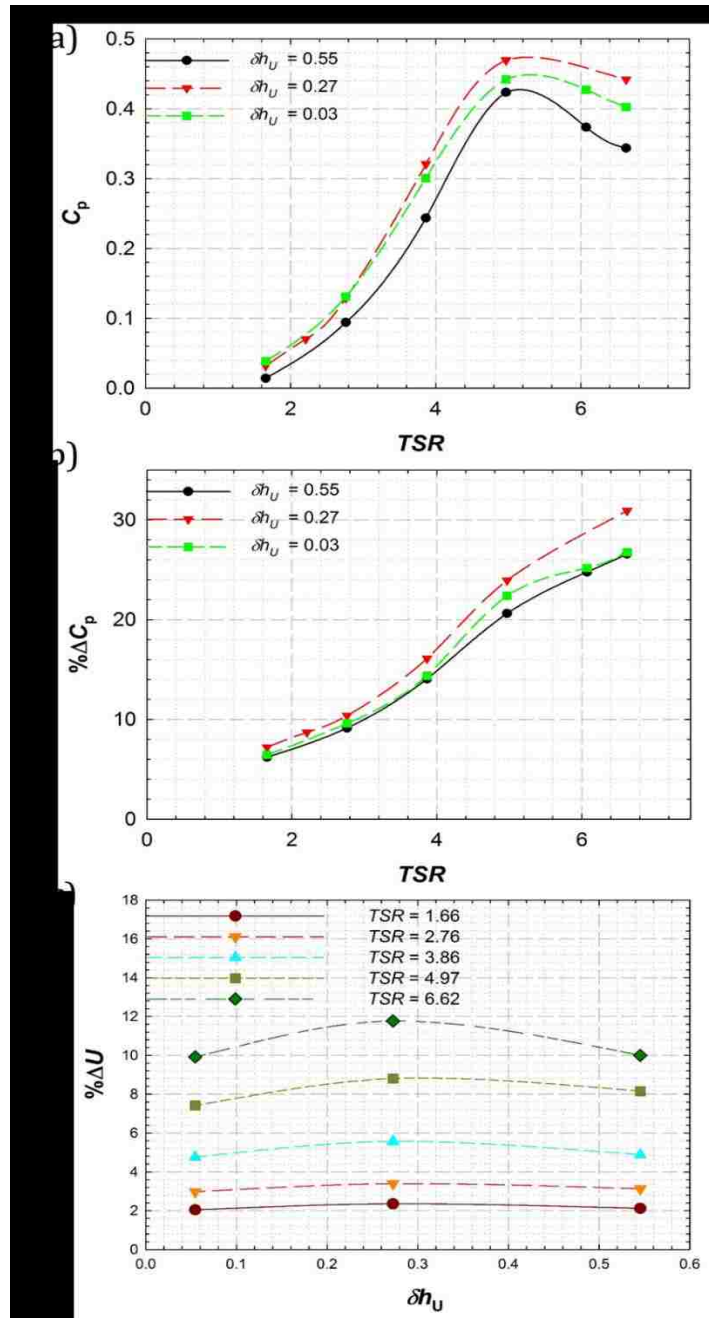
Figure 5.8: Effect of tip clearance ratio on (a) power coefficient, (b) percent change in power coefficient, and (c) percent change in effective channel velocity as a function of *TSR* for U_1 =0.8m/s

In fact, it is an objective of current work to identify the nature of stream tube shape modifications due to wake and free surface blockage and relate them to the power developed by turbine in free surface proximity environment under various flow velocity and rotational velocity operations.

5.3.2.2 Blockage correction for open surface water channel:

For a more realistic representation of current experimental facility, a blockage correction methodology was devised for an open surface water channel. Figure 5.9 presents results of this blockage correction analysis for a turbine operating in a free surface environment.
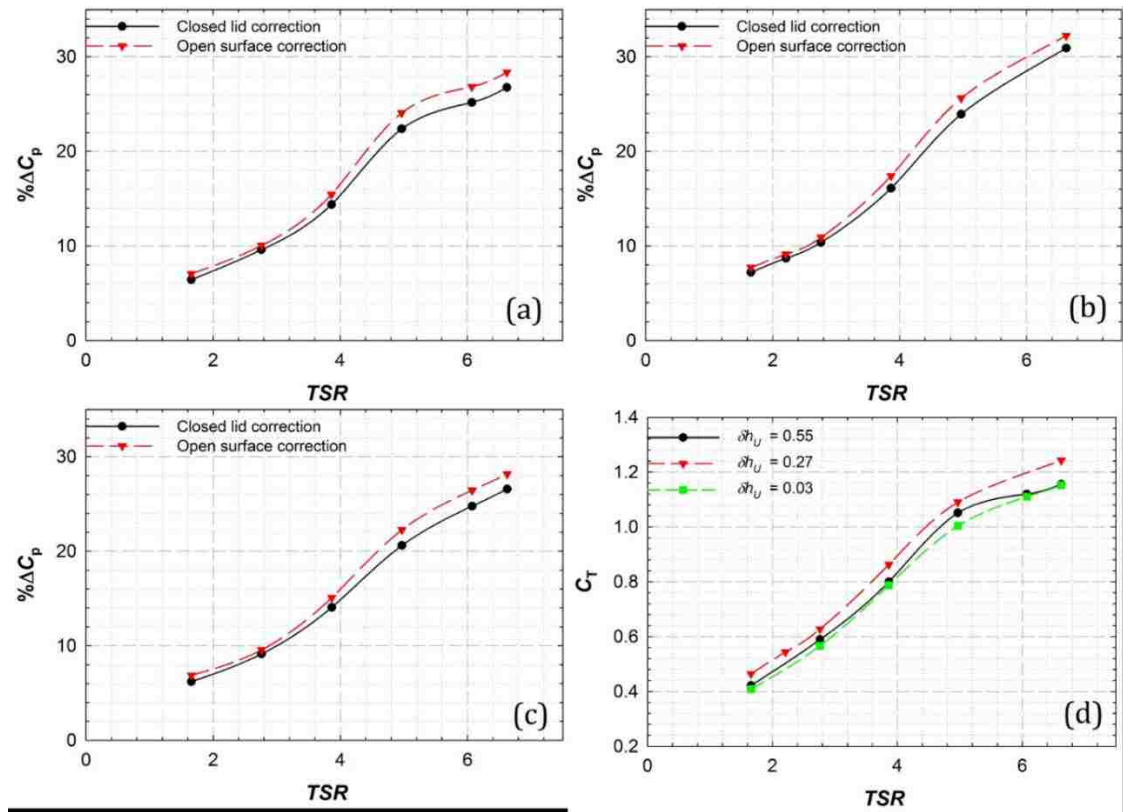
Figure 5.9: Comparison of blockage corrections based on closed top formulation and free surface formulation: percentage change in power coefficient (with respect to unblocked data) plotted against *TSR* for channel velocity of 0.8m/s and δh_U of (a) 0.55, (b) 0.27, and (c) 0.05; (d) measured thrust coefficient against *TSR* for various tip clearance ratios.

This methodology models the free surface effects in terms of a Froude number based on the water channel velocity (U_1) and the water channel depth (h_1). A comparison is presented between blockage correction methodologies based on a closed-top formulation and an open surface formulation for the flow velocity of 0.8m/s in Figures 5.9a, b, and c. Incorporation of a quartic equation (Equation 2.20) relating the flows in bypass, wake, turbine plane and upstream regions with a blockage ratio and a Froude number resulted in higher percentage change in the power coefficient compared to the closed-top formulation as shown in Figure 5.9. Thus, the open surface blockage correction which is a better representation of current experimental facility, predicts higher blockage effects compared to a closed-top formulation. The deviation between the $\%\Delta C_\mathrm{p}$ obtained from two methods increased with increasing *TSR* values indicating higher free surface effects at larger rotational speeds. The authors would like to note here that the current formulation models the free surface in terms of a Froude number based on the total channel depth and does not take into account the turbine tip to - free surface clearance. However, as the blockage correction is based on the measured thrust values from actual experiments, they reflect the effect of free surface clearance and account for this variation during the blockage effect calculations.

5.3.3   Effect of blockage and free surface proximity on near-wake flow features:

The flow visualization measurements based on a stereo-PIV technique were carried out for a channel velocity (U_1) of 0.8m/s, at different depths of immersion and rotational speeds to understand flow features in the wake and bypass regions that were responsible for the improved performance in a free surface-blocked environment. The choice of the

flow velocity for the PIV measurements was governed by the *Re* dependence study for the performance characteristics discussed previously (see Figure 5.5). The performance curve was found to be weakly dependent on *Re* change at $U_1 = 0.8$m/s. This section discusses the results of flow visualization and unravels the flow mechanisms that would help understand the thrust and power coefficients variations described in earlier section (Figures 5.4-9). During the present study, the laser sheet for the PIV measurements was aligned to the stream wise direction (XY plane) and was located at the blade root section ($z \cong 0.1 \times R$) as illustrated in Figure 5.2. For each rotational speed and tip clearance ratio, two sets of PIV measurements were carried out: first in the upper wake and second in the lower wake of the turbine. Images from these two measurements were stitched together to visualize a complete near-wake flow and bypass flow upto $X \cong 1.5 \times R$ (Figure 5.2).

5.3.3.1 Contours of stream-wise velocity:

Figure 5.10 shows contours of a normalized stream-wise velocity $\left(U_{\text{Normalized}} = U \middle/ U_1\right)$ where U represents local stream-wise velocity) for δh_U of 0.55 and rotational speeds of 180 and 270 respectively. The horizontal dashed lines represent position of the turbine tip and vertical solid lines correspond to the turbine rotation plane. For this high depth of immersion, the free surface is seen to have no effect on the wake development behind the turbine resulting in more or less symmetric structures around the turbine rotation axis. At the blade root position, a circular localized low velocity region (region I) is observed, the size of which was of the order of blade root diameter. For the case of lower rotation speed i.e. 180 RPM, wake starts to develop behind turbine rotation plane as a conical structure (regions II and III above and below the turbine axis respectively) that expands downstream the turbine as depicted in Figure 5.10. An increase

in rotational speed to 270RPM, leads to a higher effective blockage developing a recess-like structures in the upper and the lower parts of the wake (Figure 5.10b). This results in formation of additional low velocity structures in the upper and the lower parts of the wake near the blade root and blade tip - regions IIa, IIIa and IIb, IIIb as shown in Figure 5.10b. The regions IIa and IIIa start closer to the rotation plane compared to regions IIb, IIIb due to their smaller radius of rotation. In addition, the regions IIa and IIIa are observed to expand faster than regions IIb and IIIb.
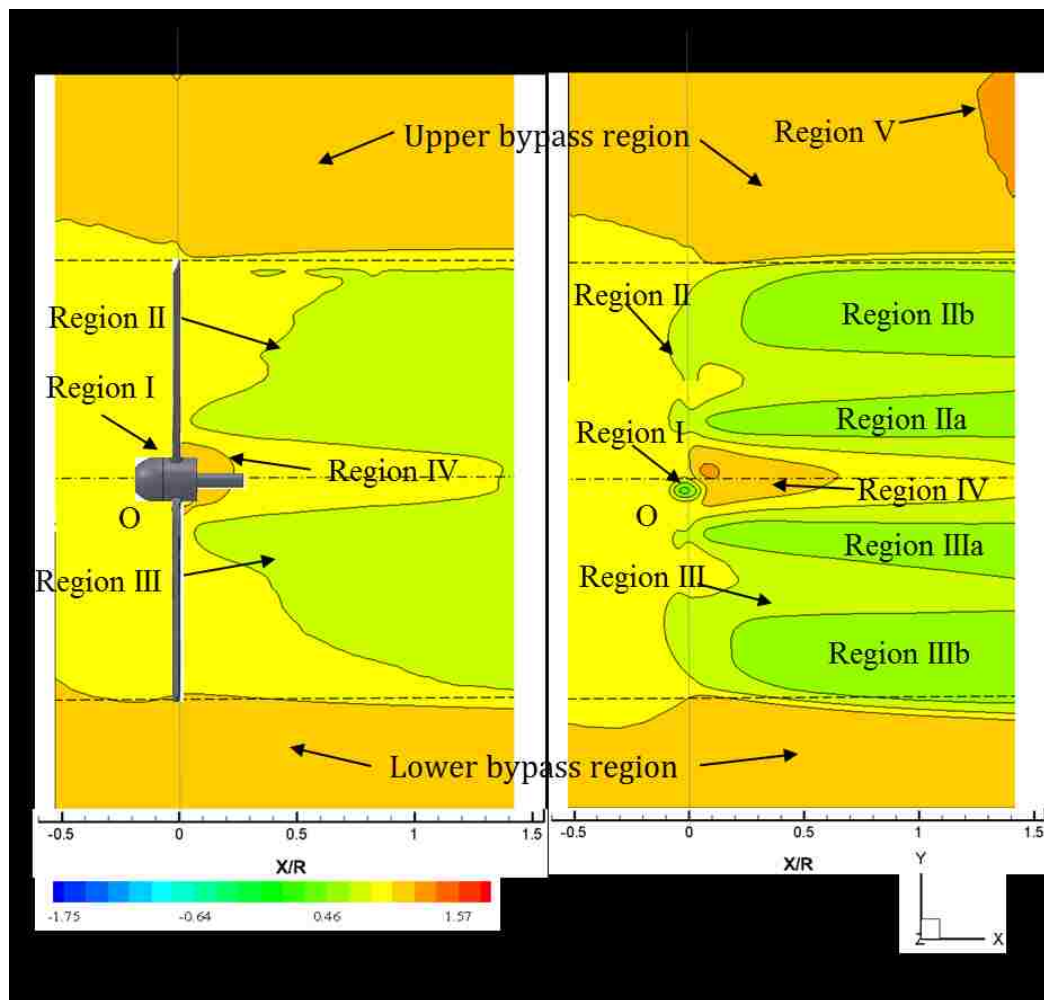
Figure 5.10: Time averaged contours of normalized stream-wise velocity $(U_{Normalized} = U/U_1)$ for $\delta h_U = 0.55$ at rotational speed of (a) 180, (b) 270 RPM (The centerline represent turbine axis location while dotted line represent blade tip location)

A localized high velocity region was developed right behind the blade root (region IV) due to flow acceleration that occurs due to smaller blockage near the blade root that has diameter smaller than the blade chord. With an increase in rotational speed, this region was observed to further elongate and extend downstream the turbine as can be seen in Figures 5.10a and b. The region IV was followed by a region of comparatively lower velocity but still higher than rest of the wake. In this region the flow velocity was comparable to the free stream velocity upstream the turbine. For the case of δh_U = 0.55, no significant difference was observed between the flow structures in the upper bypass and lower bypass regions.

Figure 5.11 presents contours of stream-wise velocity for the case of δh_U = 0.27 for rotational speeds of 180 and 270 RPM. Similar to the case of δh_U = 0.55, in this case also increasing the rotational speed of the turbine resulted in modification of the wake flow with additional flow structures at larger rotational speeds. However, in this case, flow was no more symmetric about the turbine axis, with different flow structures observed in the upper and the lower wake (regions II and III). A closer proximity to the free surface resulted in compressed upper wake leading to thinner upper wake compared the lower wake - compare Figures 5.10a with 11a and 10b with 11b. Figure 5.10a and 11a are contour plots of stream-wise velocity at same flow velocity and rotational speed but at different depths of immersions namely 0.15m and 0.08m respectively. These two cases lead to similar shape of lower wake regions (region III) but significantly different upper wake regions. At this low rotational speed, wake expansion in a radial direction for the upper wake is limited by the faster moving upper bypass region. Free surface being deformable drops behind the turbine rotation plane that leads to flow structure modifications, particularly in the upper

bypass and the upper wake regions. Increasing the turbine rotation speed lead to a higher

wake blockage and a stronger wake that extended the entire turbine rotation disc behind

the turbine. Again, as observed in Figure 5.11b, a higher velocity recess was observed to

Figure 5.11: Time averaged contours of normalized stream-wise velocity
$(U_{Normalized} = U/U_1)$ for $\delta h_U = 0.27$ at rotational speed of (a) 180, (b) 270 RPM

penetrate into the wake regions at half radial distances, however its shape was different in

upper and lower bypass regions. Moreover, the wake flow in region II was observed to be

closer to the turbine rotation plane compared to wake flow in region III as evident in Figure

5.11b. At higher rotational speed of 270RPM, a low velocity region was observed even

before the turbine rotation plane indicating inflow modification before it approaches the rotor plane.

A close proximity and associated wake compression effects can be visualized by comparing the upper wake (region II) and the upper bypass regions in Figures 5.10 and 11. Figure 5.10a and b shows a radially expanding wake for both upper and lower wake regions for $\delta h_U = 0.55$. However, in the case of $\delta h_U = 0.27$ (Figure 5.11), this radial expansion behavior was restricted to the lower wake region only. For the upper wake, where the flow is restricted by a free surface drop and associated faster moving fluid, the wake expansion process is not just inhibited, but in fact reversed, leading to a wake compression. The shape of the upper wake with respect to dashed line (corresponding to the blade tip height) in Figure 5.11 elucidate the wake compression behavior. Further, the faster the rotational speed, the higher the free surface drop that leads to progressively faster upper bypass flow and higher wake compression as depicted in Figures 5.10 and 11. The faster bypass flow and higher wake compression are primary driving forces for the high power coefficient in this case. The upper wake compression leads to asymmetric wake with narrower IIa and IIb regions in upper wake compared to IIIa and IIIb regions in lower wake.

For $\delta h_U = 0.05$ (Figure 5.12), at a rotational speed of 270 RPM, the lower wake region exhibited flow structures similar to $\delta h_U = 0.27$ case, however the upper wake was significantly different due to free surface drop that penetrated not only into the upper bypass but into the upper wake region. For all depths of immersion, at a higher rotational speed of 270RPM, a secondary region of higher flow velocity (region V) was observed in the upper bypass region whose strength increased with increasing free surface proximity (see Figures 5.10-12). For a deeper submersion depth, a high velocity region V of only a

marginal strength was observed near the upper right corner of the region of interest. However, for the case of $\delta h_U = 0.27$, a stronger and larger high velocity region was observed in the upper right corner of the region of interest. For the case of $\delta h_U = 0.05$ (Figure 5.12), a secondary region of high velocity, region V was developed, for all rotational speeds and was closer to the turbine rotation plane as compared to the case of $\delta h_U = 0.27$. Increasing rotational speeds moved this region closer to the turbine and deeper into the upper wake region.
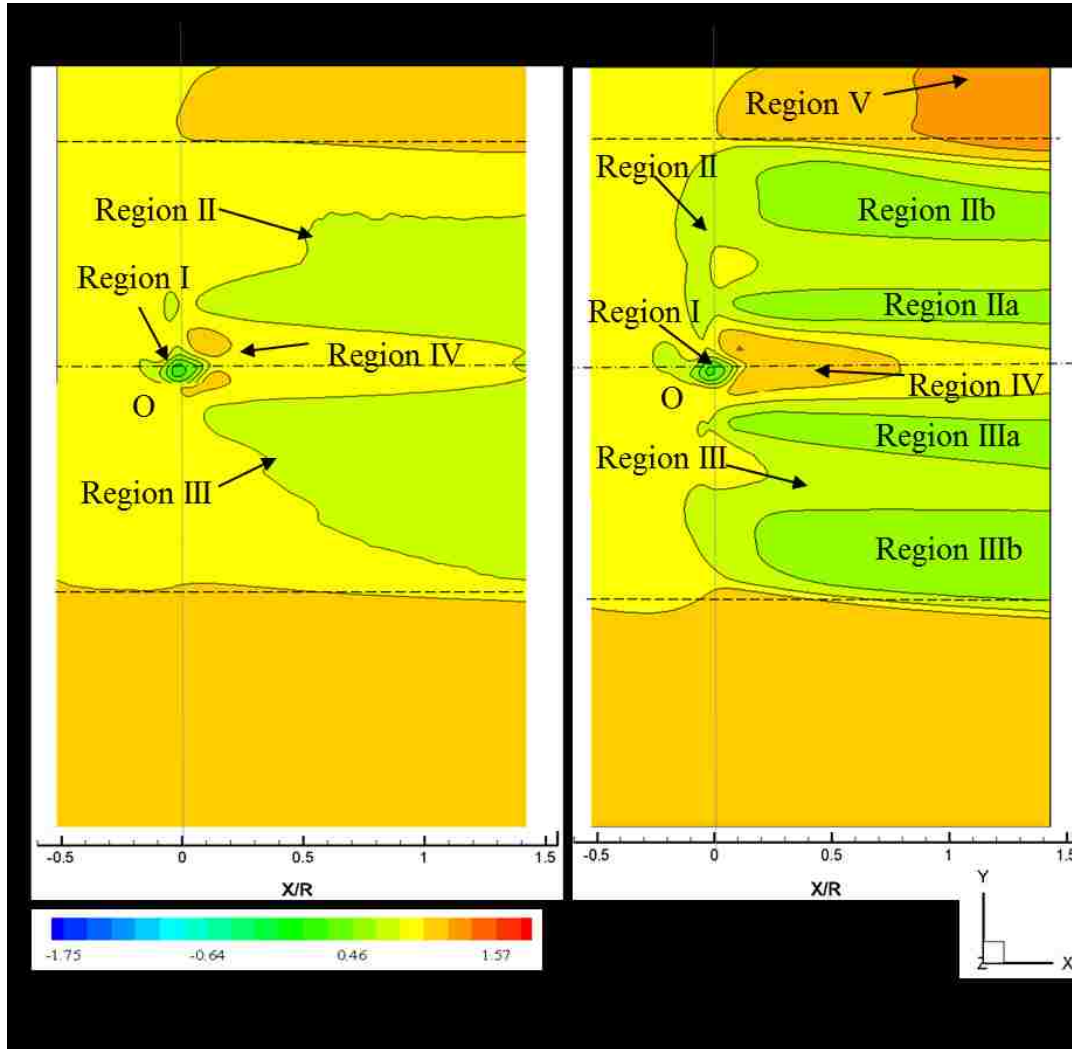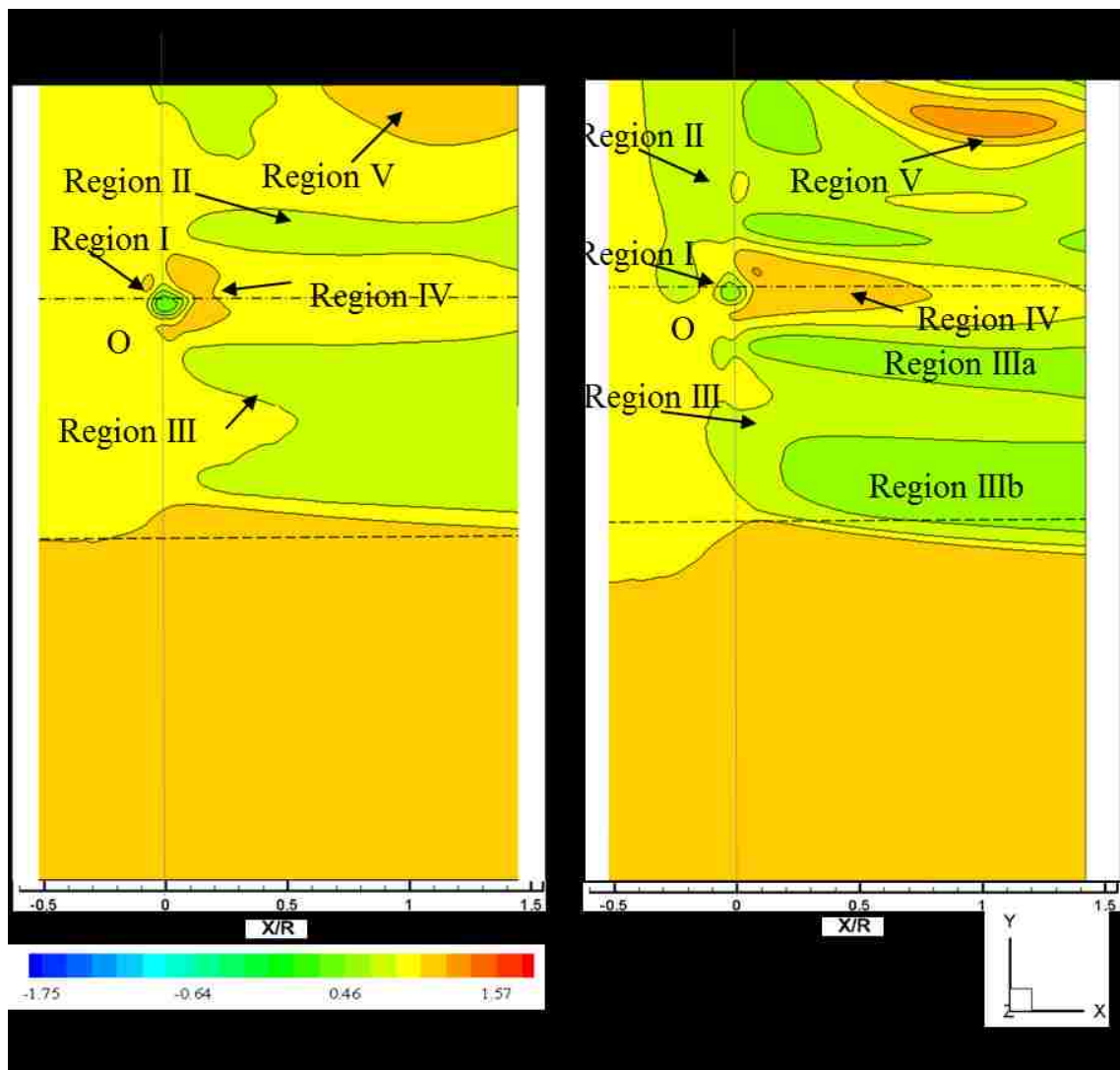

Figure 5.12: Time averaged contours of normalized stream-wise velocity $\left(U_{Normalized} = U/U_1\right)$ for $\delta h_U = 0.05$ at rotational speed of (a) 180, (b) 270 RPM

Further, it is interesting to note the shape of incoming stream-tube near the turbine rotation plane. An increase in rotational speed leads to a higher obstruction (higher effective blockage) to the incoming flow that resulted in a bulge in stream-tube just before the rotation plane (compare Figures 5.10a with 10b and 11a with 11b). The bulge is higher near the upper bypass region compared to the lower bypass region due to an upward deflection of the flow as it approaches the rotation plane. Further, the shape of upper bypass and its interface with wake varied significantly with tip clearance distances. For the case of $\delta h_U = 0.55$, the stream-tube containing the turbine rotation disc was found to be enclosed by the upper bypass and lower bypass regions. However, a reduction in depth of immersion modified the incoming stream-tube that extended well into the upper bypass region (compare Figures 5.11 and 12). This delayed the inception of the upper bypass region to the turbine rotation plane.

5.3.3.2 Contours of Vertical velocity:

Figure 5.13 presents contours of vertical velocity normalized by freestream velocity ($V_{\text{Normalized}} = V/U_1$) for turbine operating at two different rotational speeds: 180 (left column), 270RPM (right column) and two different tip clearance ratios ($\delta h_U = 0.55$ and 0.27). For all cases, regions of high vertical velocity were observed at blade tip locations near the turbine rotation plane. The intensity of this high vertical velocity region increased with increasing rotational speed - compare left column (180 RPM) to right column (270 RPM). Additional regions of high velocity were observed behind the hub indicating flow deflection as it passes over the hub. In general the lower submersion depth ($\delta h_U = 0.27$, second row) resulted in lower vertical velocities compared to the case of deeply submerged turbine ($\delta h_U = 0.55$, first row). Moreover, for $\delta h_U = 0.27$, a region of negative localized

vertical velocity was observed behind the turbine rotation plane whose intensity increased with an increase in the rotational speed (Figure 5.13b). This region of downward velocity is an indicative of a bulk downward motion of fluid causing a free surface deformation at approximately X=0.5×R behind the turbine. This results in radial compression of the upper wake leading to an unsymmetric wake and a faster upper bypass region.
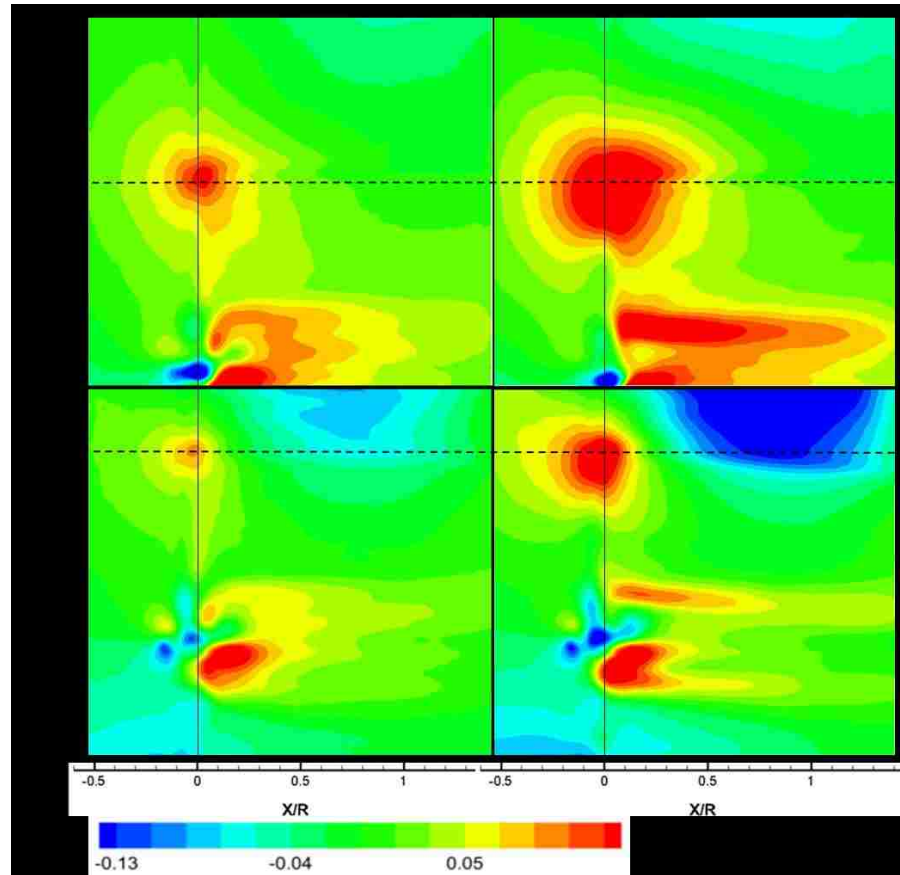
Figure 5.13: Time averaged contours of normalized vertical velocity $\left(V_{Normalized} = V/U_1\right)$ for rotational speed of 180 RPM (left column) and 270 RPM (right column) for δh_U of: (a) 0.55 and (b) 0.27

5.3.4 Profiles of stream-wise and vertical velocities:

5.3.4.1 Variation along depth of the channel (along lines of constant X):

To get a better insight into the velocity variations in the bypass and wake flow, we plot profiles of stream-wise and vertical velocities at various downstream locations. The profiles are plotted on vertical lines of constant X ranging from -0.25R to 1.35R

5.3.4.2 Stream-wise velocity profiles:

Figure 5.14 presents profiles of stream-wise velocity in the near wake region on vertical lines at one upstream and six downstream locations ranging from -0.25R to 1.35R. These lines are coincident with a vertical plane that passes through the blade root ($Z \cong 0.1R$).
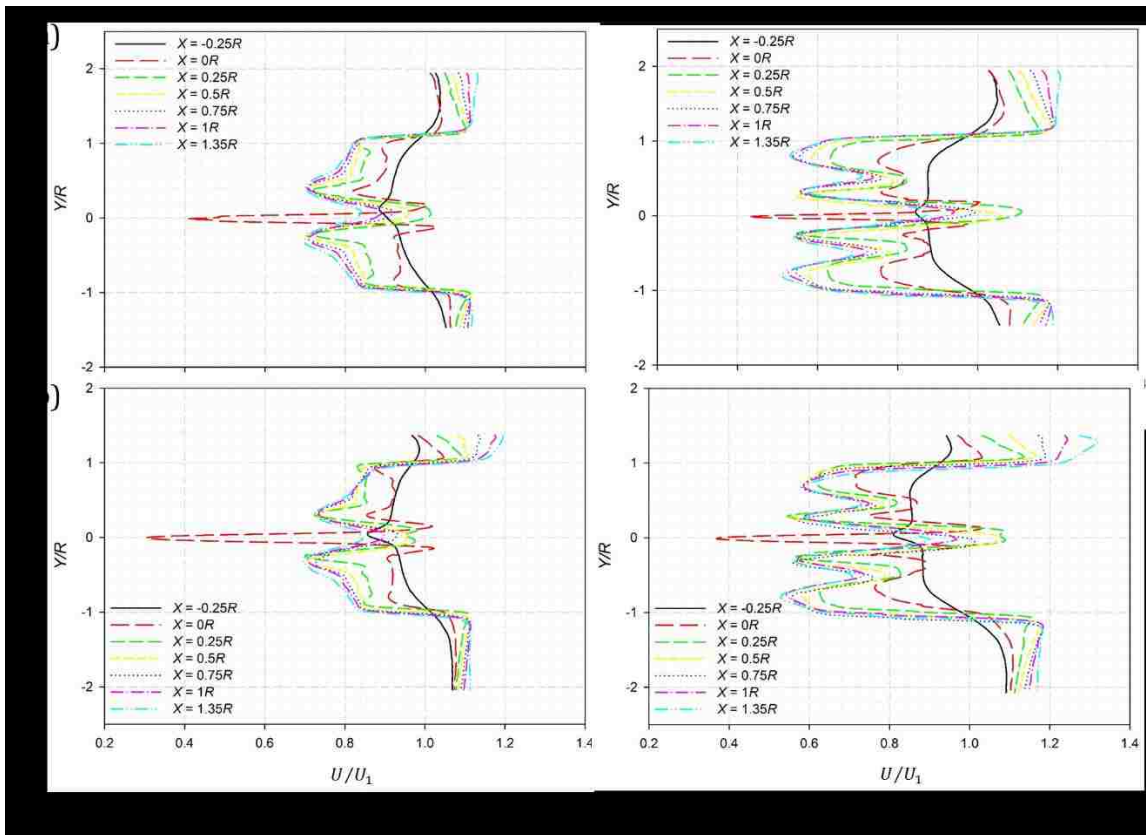
Figure 5.14: SPIV time-averaged data: Profiles of normalized stream-wise velocity at various downstream locations for 180 RPM (left column) and 270RPM (right column) for δh_U of (a) 0.55 and (b) 0.27

156

Positioning the turbine at $\delta h_U = 0.55$ resulted in identical upper and lower bypass regions with comparable flow velocities for a rotational speed of 180RPM (see Figure 5.14a, left column). For the upper bypass region, minimum velocity was observed at X=0R, while for the lower bypass region, minimum velocity was observed at X=-0.25R, however the difference was not very significant. Further, this case also produced a symmetric wake with similar velocity distributions in the upper and lower wake regions. Highest wake velocity was observed at the turbine rotation plane, X=0R that progressively decreased further away from the turbine rotation plane until X=1.35R with successively lower percentage change as seen in Figure 5.14a. However the trend was exactly opposite for the bypass regions with minimum velocity observed at X=0R and maximum velocity at X=1.35R which is in accordance with the conservation of mass principle. A spike at position X=0R corresponds to blade root position showing minimum flow velocity.

Figure 5.14a, right column plots profiles of stream-wise flow velocity for a rotational speed of 270RPM. Compared to the 180RPM case, a larger spread was observed in both wake and bypass flow velocities. A higher rotational speed lead to a stronger wake region with lower wake velocities compared to the case of 180RPM. This also lead to formation of additional low velocity wake structures named as IIa, b and IIIa, b regions as illustrated in right column of Figure 5.14a. Regions IIa and IIIa emerge from a near blade root region and regions IIb and IIIb emerge from a near tip region and form inner and outer cores of the wake. These low velocity regions can be identified by four parabolic profiles in Figure 5.4b, two in the upper wake and two in the lower wake region. Faster rotational speed resulted in slower wake region that was accompanied with faster bypass regions compared to the left column of Figure 5.14a. For this case, the wake region shows a strong

flow deceleration from position X=0R to 0.25R, almost twice compared to the case of 180RPM. This flow deceleration in the wake region is balanced by a flow acceleration in the bypass region with a higher percentage increase in the flow velocity from position X=0R to 0.25R. Similar to the case of 180RPM, position X=1.35R corresponds to a maximum bypass flow velocity and a minimum wake velocity.

Figure 5.14b shows profiles of stream-wise velocity on vertical lines at one upstream and six downstream locations for $\delta h_U = 0.27$ and rotational speeds of 180 and 270. For a rotational speed of 180 RPM, wake structures similar to the case of $\delta h_U = 0.55$ were developed, but in this case they were less symmetric. The lower wake region shows larger parabolic profiles compared to the upper wake indicating a faster upper wake due to the wake compression effects. Though the lower bypass flow exhibited characteristics similar to the case with $\delta h_U = 0.55$, a wider spread was observed in the upper bypass region with minimum velocity observed at X=0R and maximum velocity at X=1.35R. All these effects substantiate an asymmetry in the wake and the bypass flows that modifies the turbine performance. Increasing the rotational speed from 180 to 270RPM (Figure 14b, right column) resulted in an expansion of parabolic profiles in the horizontal and vertical directions indicating a slower and stronger wake. This was also accompanied with successively faster upper bypass regions. A larger deviation between the examined bypass velocities was observed at the higher rotational speeds. The upper bypass and the upper wake regions were found to be more prone to changes in the turbine rotation speed and free surface proximity compared to the lower wake and bypass regions. Further, it is to be noted that the velocity profiles show maxima at different depths for different downstream

locations, suggesting presence of a strong time-varying shear flow which is further discussed in section 4.3.3.

5.3.4.3 Vertical Velocity profiles:

Profiles of vertical velocities are plotted on vertical lines in Figure 5.15 for rotational speed of 180RPM (left column) and 270RPM (right column) at one upstream and six downstream locations for $\delta h_U = 0.55$ and 0.27. For rotational speed of 180RPM, both cases show maximum velocity on turbine rotation plane ($X=0R$) due to centrifugal and Coriolis forces causing span-wise flow.
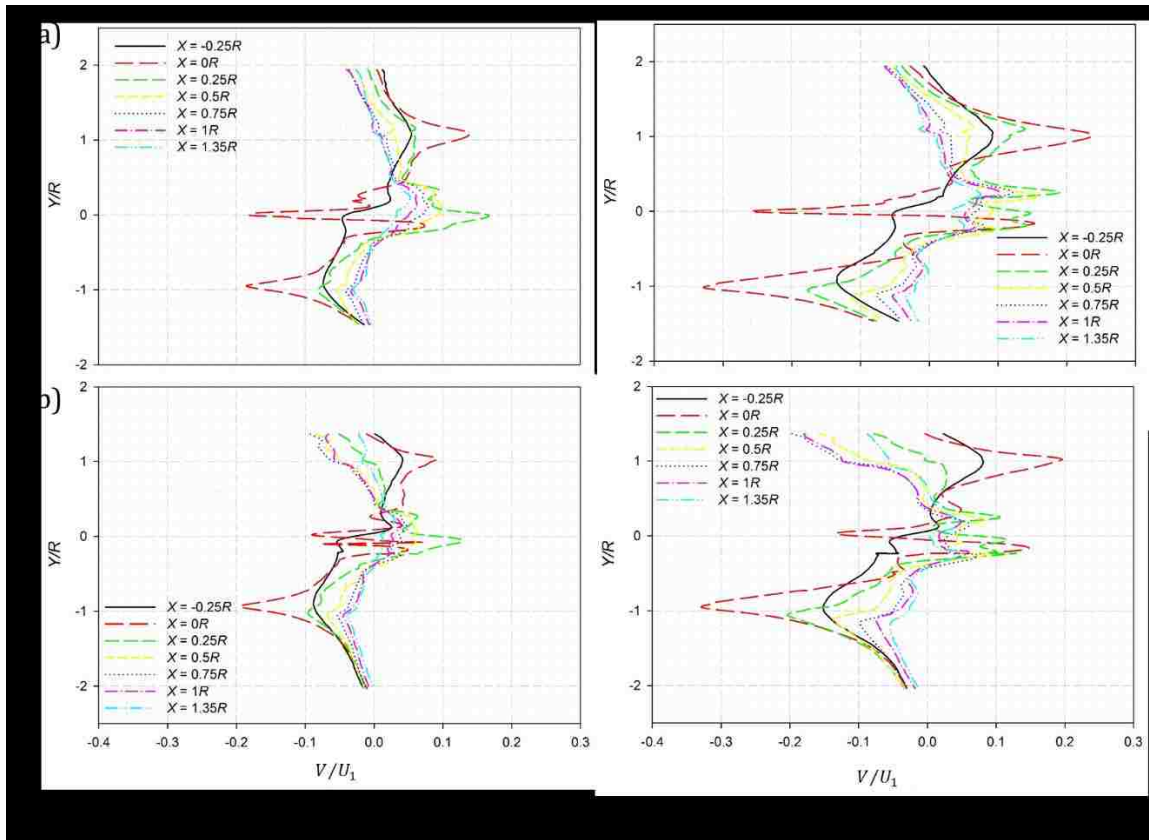
Figure 5.15: SPIV time-averaged data: Profiles of normalized vertical velocity at various downstream locations for 180 RPM (left column) and 270RPM (right column) for δh_U of (a) 0.55 and (b) 0.27

Further, spikes (positive in upper wake and negative in lower wake) are observed at blade tip locations due to flow acceleration from pressure side to suction side of blade which is

responsible for formation of tip vortices. Additional spikes are also observed at hub radius due to tangential flow leaving the hub.

For the case with $\delta h_U = 0.55$, the velocity profiles in the upper bypass region show a very narrow spread between various downstream locations (Figure 5.15a). However, with decreasing depth of immersion (Figure 5.15b), a wider spread of vertical velocities was observed between various downstream locations. For $\delta h_U = 0.55$, minimum velocity occurred around X=1R, while for $\delta h_U = 0.27$, it was around X=0.75R and for $\delta h_U = 0.05$, minimum velocity occurred at X=0.5R. The negative vertical velocities in the upper bypass region are indicative of wake re-energization process due to flow from upper bypass region into the wake region. However when these negative velocities are accompanied with downward motion of a lump of fluid mass (due to free surface deformation), it leads to either a wake compression or a wake penetration effect. The wake compression process leads to a longer propagation distance while the wake penetration by high localized downstream motion of free surface results in shorter wake propagation distance behind the turbine plane. The case with $\delta h_U = 0.27$ shows higher downward velocities compared to the case with $\delta h_U = 0.55$ which was accompanied with free surface drop and wake compression as shown earlier in Figure 5.11. Moving the turbine further closer to the free surface resulted in higher downward velocities and higher (and localized) free surface drop that penetrated into the upper wake virtually killing it with no signs of regions IIb as shown earlier in Figures 5.12 and 13.

Figure 5.15 (right column) presents profiles of vertical velocity for 270RPM at various downstream locations. Higher rotational speeds in this case led to larger spikes at hub radius and blade tip location. This increase in the magnitude of spike is more evident

at the blade tip locations due to faster span-wise flow and larger radius of rotation at blade tips compared to hub radius resulting in higher tangential velocity. Further, much wider spread was observed between upper bypass velocities at various downstream locations compared to the case with 180 RPM (compare left and right columns of Figure 5.15). Increasing the proximity to free surface resulted in spanning the velocities in upper bypass region over a wider range as compared to lower rotation speed of 180RPM. Similar to 180 RPM case, lowest vertical velocities were observed at X=1R, 0.75R and 0.5R for $\delta h_U =$ 0.55 and 0.27, but with higher magnitudes. Looking at Figures 5.14 and 15 collectively, it can deduced that, the shape of the free surface drop depends on proximity to surface but the intensity of drop depends on rotational velocity induced wake blockage.

5.3.5   Variation along wake propagation direction (along lines of constant Y):

To quantify the near wake development, profiles of stream-wise, and vertical velocities are plotted in Figures 5.16-19 along horizontal lines at different heights measured from turbine axis that correspond to 0R, 0.5R, 1R, and 1.3R. This data is extracted from ensemble averaged images of respective cases. For 180RPM case (Figure 5.16), no significant variation was observed between δh_U = 0.55 and 0.27 cases at hub height (Y=0R), except for near-hub region of -0.3<X/R<0.3, in which δh_U = 0.55 case showed consistently higher velocities than δh_U = 0.27 case (Figure 5.16a). A spike in U at X=~0.15R corresponds to a high velocity region that develops behind the hub due to flow acceleration around the hub. At Y=0.5R (Figure 5.16b), stream-wise velocity for both δh_U = 0.55 and 0.27 case showed similar trends up to X/R of 0.15, beyond which, higher velocities were observed for δh_U = 0.27 case. An interesting phenomenon was observed at Y=1R (Figure 5.16c) which elucidates wake compression and faster bypass velocity

behaviors. At this height, $\delta h_U = 0.55$ case shows slower moving fluid with normalized velocity of 0.87 at 1.4R downstream the turbine. However, at the same location, $\delta h_U = 0.27$ case shows significantly higher (normalized) flow velocity of 1.12, which implies that fluid in this region is moving faster that incoming flow and is not a part of wake but of upper bypass flow.
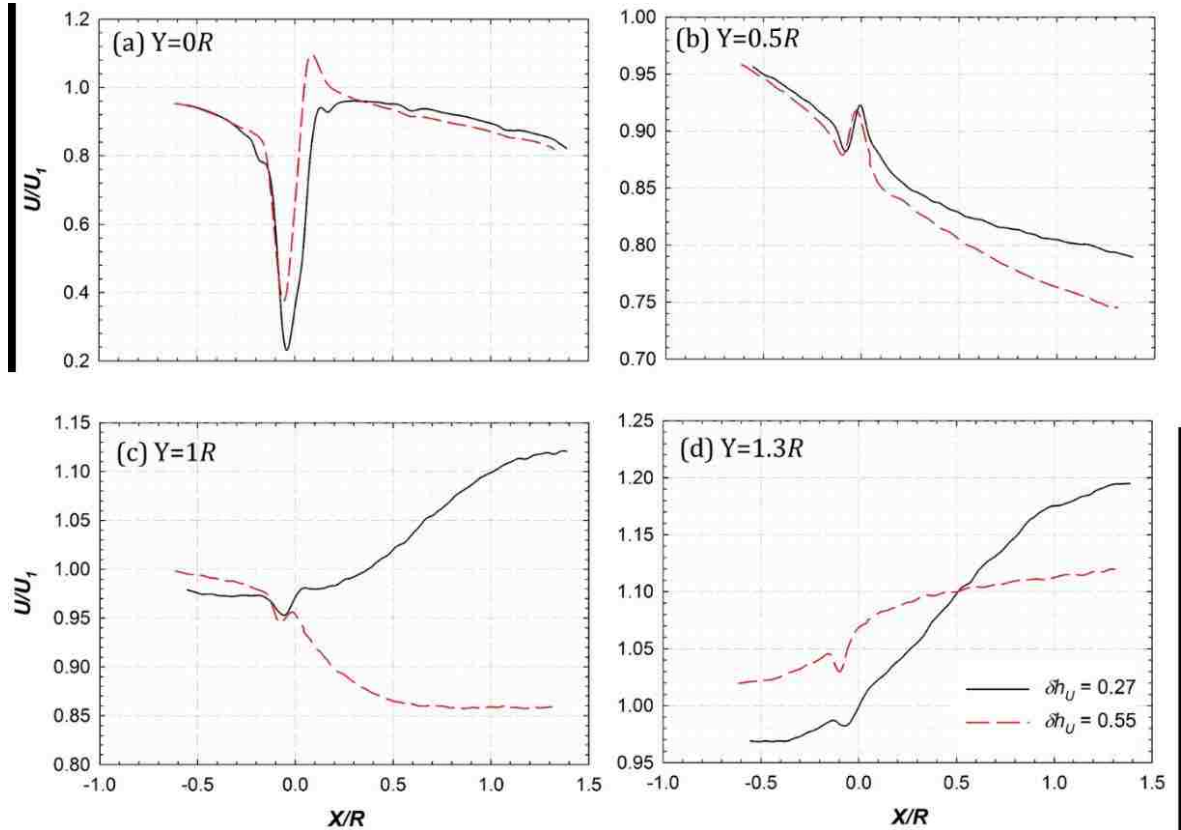
Figure 5.16: Variation of normalized stream-wise velocities for rotational velocity of 180 RPM and tip clearance ratios of 0.55 and 0.27 on horizontal lines at various depths: (a) Y=0R, (b) Y=0.5R, (c) Y=1R, (d) Y=1.3R

The decreasing U_1 velocity trend for the case of $\delta h_U = 0.55$ tends to reach asymptote around X/R of 1, while increasing trend of U_1 for $\delta h_U = 0.27$ case continues beyond X=1.4R but with progressively lower slope. The $\delta h_U = 0.27$ case shows significantly higher slope compared to $\delta h_U = 0.55$ case. Further away from the turbine axis at Y=1.3R (Figure 5.16d), flow belongs to upper bypass region for both $\delta h_U = 0.55$ and 0.27 cases. At this

162

height, $\delta h_U = 0.55$ case exhibited higher flow velocity than that of the $\delta h_U = 0.27$ case up to X/R of 0.5, beyond which a faster bypass region was observed for $\delta h_U = 0.27$ case. It is also worth noting the incoming flow behavior for various cases. The incoming flow for both depths was of same magnitude at Y=0R and 0.5R, but in regions away from the turbine axis, faster incoming flow was observed for $\delta h_U = 0.55$ case.

Figure 5.17 shows profiles of vertical velocities along constant X lines at rotational speed of 180RPM and various depths of immersions. For all Y locations, $\delta h_U = 0.55$ case showed higher vertical velocities compared to $\delta h_U = 0.27$ case. Due to rotational motion

Figure 5.17: Variation of normalized vertical velocities in upper bypass region for rotational velocity of 180 RPM and tip clearance ratios of 0.55 and 0.27 on horizontal lines at various depths: (a) Y=0R, (b) Y=0.5R, (c) Y=1R, (d) Y=1.3R

of turbine, the vertical velocities in the +XY quadrant, (the laser sheet is in a plane parallel to XY plane, but offset from origin at Z≅0.1R) are expected to be positive. For the wake

region, at a constant (X, Y) position, a high value of vertical velocity indicates faster rotating fluid.

Thus, higher vertical velocities of $\delta h_U = 0.55$ case indicate faster rotating wake region compared to $\delta h_U = 0.27$ case. Thus, for $\delta h_U = 0.55$ case, we can deduce from Figure 5.16b and 17b that, the wake flow is rotating faster but has lower stream-wise velocity for Y=0.5R. The vertical velocity profiles at Y=1R height (Figure 5.17c) indicate vertical transfer of momentum flux between upper wake and upper bypass region. At this height, for $\delta h_U = 0.27$ case, a downward vertical velocity is observed starting around X=0.2R behind the turbine which reaches minimum (6.5%U_1) at X=0.8R downstream the turbine rotation plane. This downward motion causes wake compression yielding faster flow that explains higher stream-wise velocities for $\delta h_U = 0.27$ case in Figure 5.14b. At Y=1.3R, even higher downward velocities (up to 8.2% of U_1) were observed at similar downstream distance of X=0.8R (Figure 5.17d).

5.3.6 Effect of rotational speed on flow features:

To quantify the effect of rotational velocity (wake blockage) on velocity distribution in near wake region, profiles of horizontal and vertical velocities for 270RPM at Y=1R and 1.3R are plotted in Figures 5.18 and 19 respectively. A comparison is presented between respective profiles for 180RPM (Figures 5.16 and 5.17) and 270RPM (Figures 5.18 and 5.19). In general, for a deeply submerged turbine, a higher rotational speed led to faster rotating wake and slower moving (stream-wise) flow. For $\delta h_U = 0.55$ case, higher rotational rate resulted in slower wake (at Y=1R) with stream-wise velocity ~5% lower than 180RPM case. However, for a turbine operating at low free surface proximity ($\delta h_U = 0.27$) case, increasing rotational speed to 270RPM led to up to 6% faster

164

flow (at Y=1R) compared to 180RPM case (compare Figures 5.16c and d with 5.18a and b). Comparison of Figures 5.17c with Figure 5.19a shows that, vertical velocity profiles at
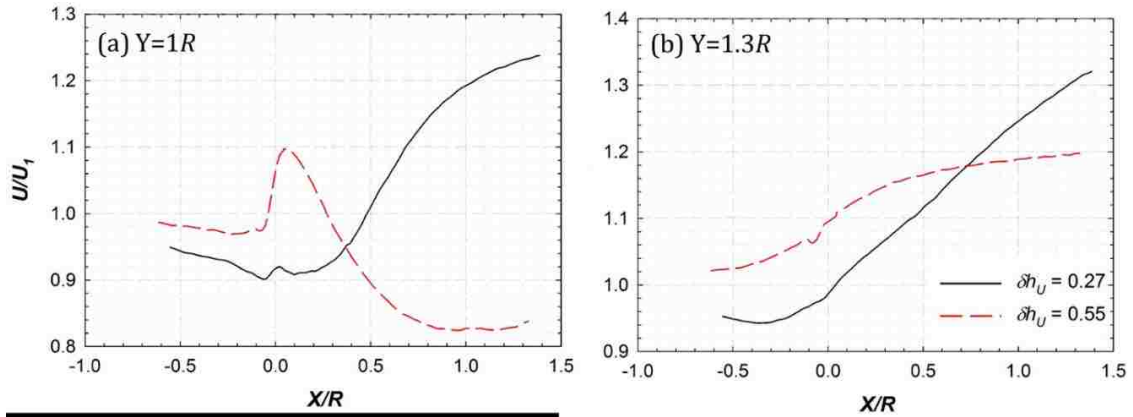
Figure 5.18: Variation of normalized stream-wise velocities in upper bypass region for rotational velocity of 270 RPM and tip clearance ratios of 0.55 and 0.27 on horizontal lines at various depths: (a) Y=1R, (b) Y=1.3R
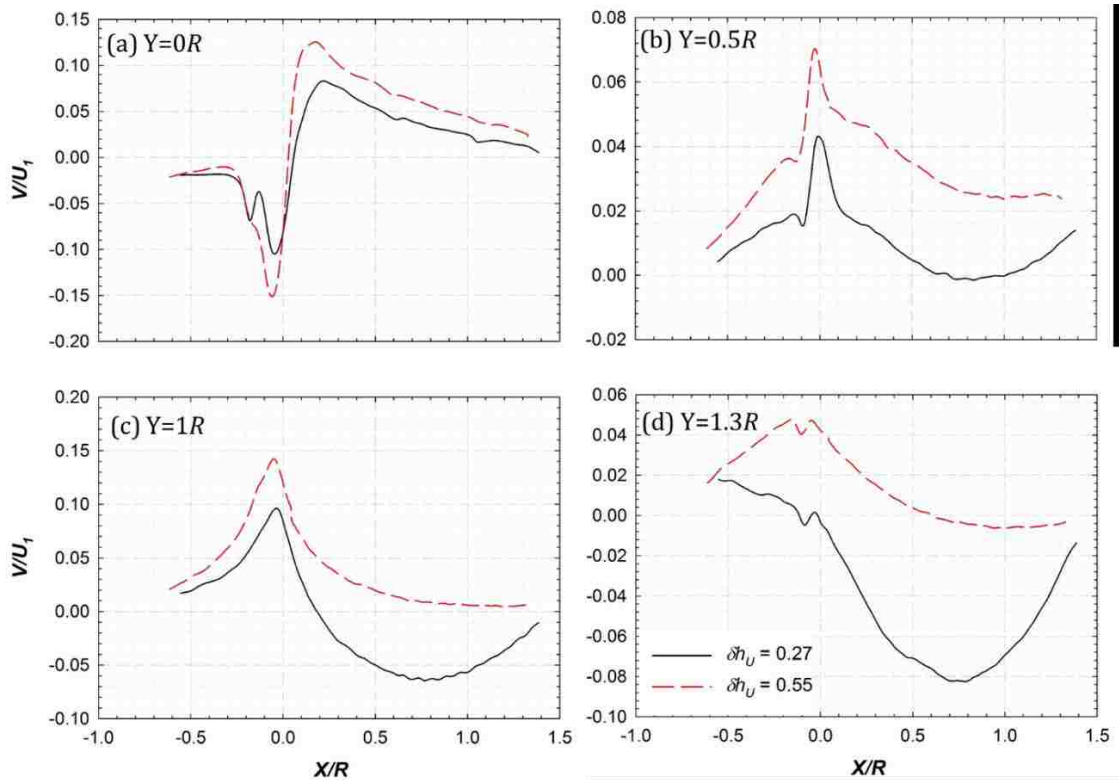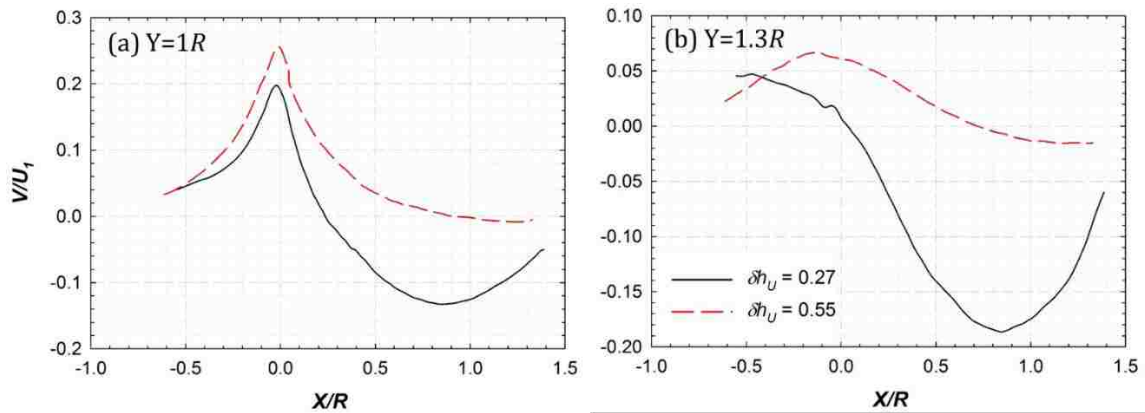

Figure 5.19: Variation of normalized vertical velocities in upper bypass region for rotational velocity of 270 RPM and tip clearance ratios of 0.55 and 0.27 on horizontal lines at various depths: (a) Y=1R, (b) Y=1.3R

Y=1R, exhibit maxima near X=0R similar to 180RPM case, however maximum value increased from 0.095U (Figure 5.17c) to 0.2U (Figure 5.19a) for $\delta h_U = 0.27$ case and 0.14 (Figure 5.17c) to 0.24 (Figure 5.19a) for $\delta h_U = 0.55$ case (higher % change for $\delta h_U = 0.27$ depth). The minima of vertical profile line for Y=1R was observed at X=0.8R (Figure 5.19a) with a magnitude -0.13U compared to -0.06 U at X=0.74R of 180 RPM case (Figure

165

5.17c). This implies that higher rotational speeds lead to higher downward velocities, meaning higher wake compression effects.

5.3.7   Comparison of flow in upper and lower bypass regions:

Figures 5.20 and 21 presents profiles of horizontal and vertical velocities in the lower wake and bypass region for $\delta h_U = 0.55$ and 0.27 and rotational speeds of 180RPM (left column) and 270RPM (right column).
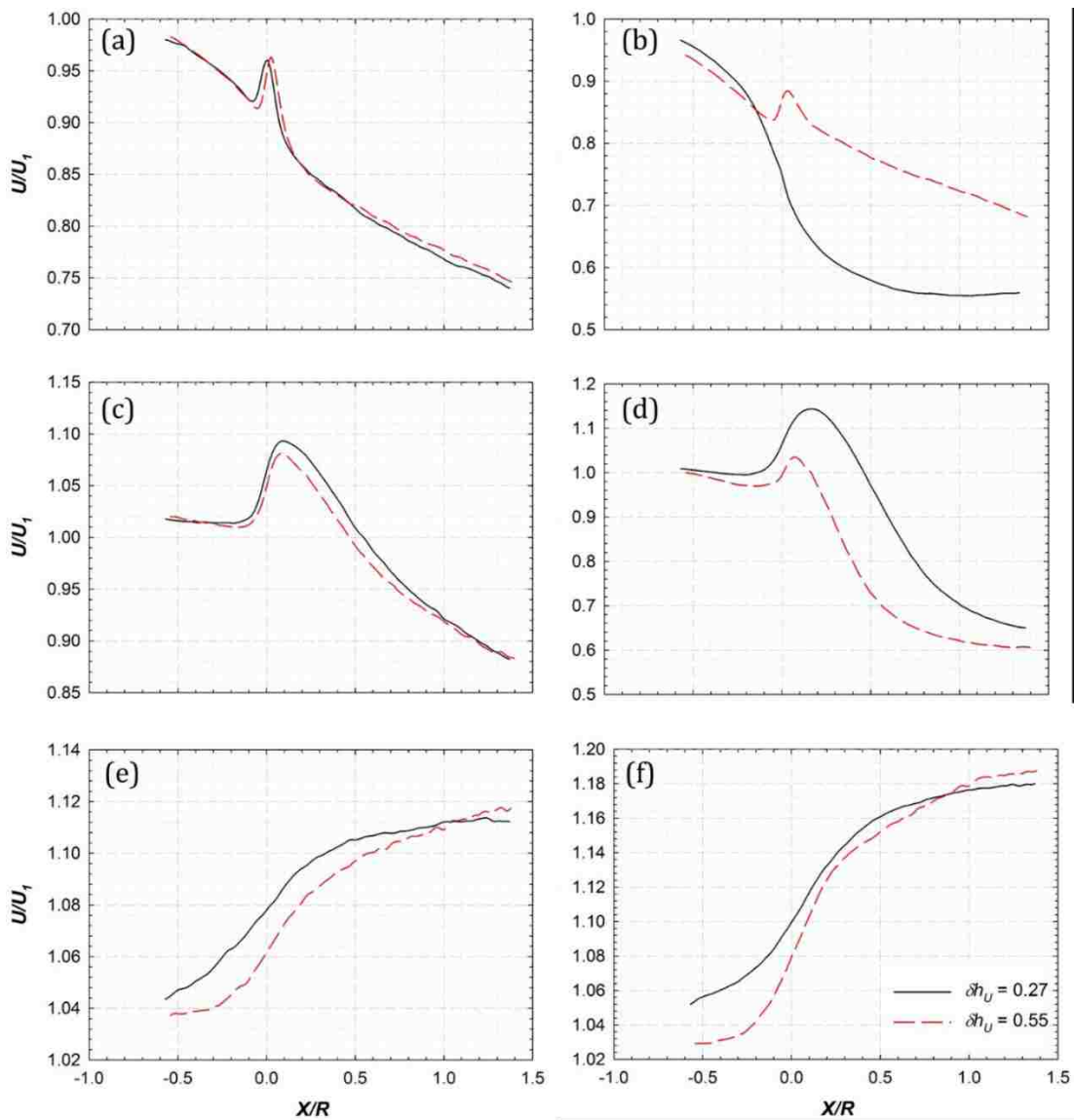
Figure 5.20: Variation of normalized stream-wise velocities in lower bypass region for rotational velocity of 180 (left column) and 270 RPM (right column) and tip clearance ratios of 0.55 and 0.27 on horizontal lines at various depths: (a) and (b) Y=0.5R, (c) and (d) Y=1R, (e) and (f) Y=1.3R

For rotational speed of 180RPM (Figures 5.20a, c and e), both $\delta h_U = 0.55$ and 0.27 cases, exhibited similar stream-wise velocity behavior at Y=-0.5R, -1R, and -1.3R, with $\delta h_U =$ 0.27 cases showing slightly faster flow. However, as rotational speed increased to 270RPM (Figures 5.20b, d and f), a wide variation was observed between two depths of immersions. The case with $\delta h_U = 0.27$ exhibited lower velocity at Y=0.5R but higher stream-wise velocities at Y=1R and 1.3R indicating free surface effects. Comparison of Figure 5.20 with Figure 5.16 shows higher stream-wise velocities in lower wake compared to upper wake for both $\delta h_U = 0.55$ and 0.27 cases. A significant difference between velocity profiles at Y=±1R indicates that, the point Y=-R corresponds to lower wake region while Y=+R is a point outside upper wake and belongs to a faster upper bypass region. This shows presence of asymmetric wake with smaller radius for the upper wake compared to the lower wake. Further away from the turbine axis, U profiles appear to fall on each other for lower bypass, while upper bypass region shows appreciable variation. Further, Figure 5.21 presents variation of normalized vertical velocity for two rotational speeds (180RPM-left column and 270RPM-right column) and two depths of immersions ($\delta h_U = 0.55$ and 0.27). Higher rotational speed led to larger values of vertical velocity as depicted in Figure 5.21. Further, a low proximity case ($\delta h_U = 0.27$) exhibited higher vertical (downward) velocities compared to a deeply submerged turbine case.
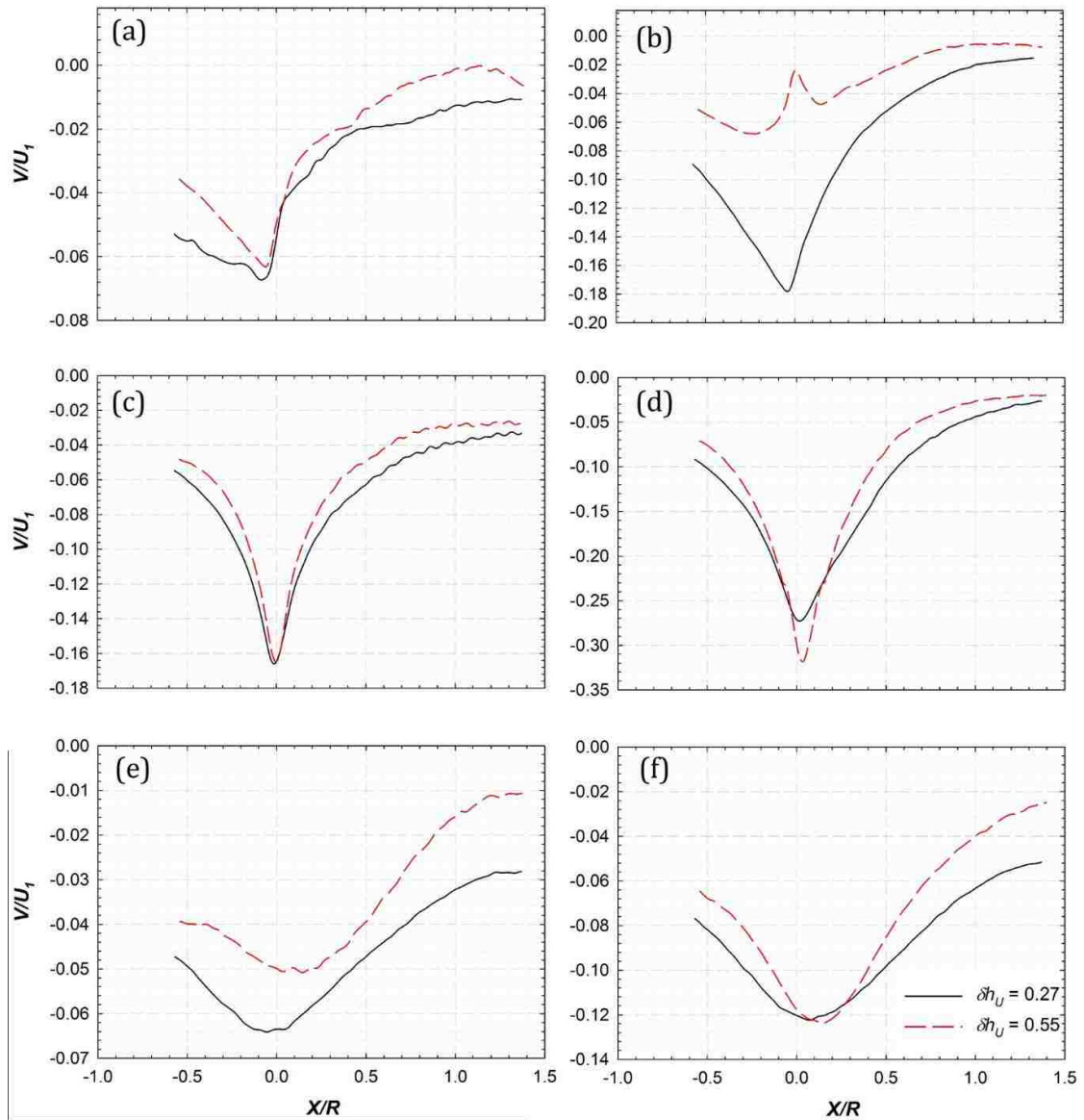
Figure 5.21: Variation of normalized vertical velocities in lower bypass region for rotational velocity of 180 (left column) and 270 RPM (right column) and tip clearance ratios of 0.55 and 0.27 on horizontal lines at various depths: a) and (b) Y=0.5R, (c) and (d) Y=1R, (e) and (f) Y=1.3R

5.3.8 Contours of strain rates and turbulence parameters:

According to the conservation of momentum principle, the thrust force on a turbine is due to pressure discontinuity across the turbine rotation plane which is balanced by: (a) momentum change between incoming flow and wake flow and (b) shear stresses at the wake and bypass flow interface [101]. As illustrated in Figures 5.10-21, an increase in free

168

surface proximity results in free surface deformation leading to wake compression. This results in faster flow in both upper wake and upper bypass regions. However, as the flow in upper bypass region is sandwiched between free surface and wake flow, a higher percentage increase (compared to unconfined-no free surface proximity scenario) occurs in upper bypass region compared to upper wake region as can be visualized in Figure 5.14b. This will lead to higher shear stresses at the interface between wake and bypass region. Further, the shape and intensity of free surface deformation was found to be dependent on Reynolds number, rotational speed and tip clearance. For tip clearance ratio of 0.27, the free surface deformation was found to complement the turbine performance, while for δh_U = 0.05, excessive localized free surface drop lead to wake instabilities. For this low tip clearance ratio, the free surface was found to penetrate into the wake region as depicted in Figures 5.12-13. In the upper wake region, the tip vortex structures bounding the wake region were washed away by the free surface drop without any significant modifications of the lower wake and tip vortices below the turbine axis.

Thus for MHkT operating in free surface environment, the wake is highly unsymmetric (depending on δh_U, RPM and U), leading to cycling variation in the flow structures in wake and at the interface of wake and bypass regions. This will result in higher shear stresses in upper bypass and upper wake regions leading to faster dissipation and shorter propagation of wake structures enabling faster wake recovery process. The combined effect is to increase the thrust force on turbine with increasing proximity (compare δh_U = 0.55 and 0.27). However, very close proximity (δh_U = 0.05) results in localized free surface drop leading to wake instabilities and higher turbulence stresses negating the complimentary effects of elevated shear stresses. The results from stereo-PIV study

presented in Figures 5.22-24 confirm this hypothesis. Figures 5.22 and 23 plot contours of strain rates and Reynolds stresses respectively obtained from PIV measurements for rotational velocity of 180RPM.
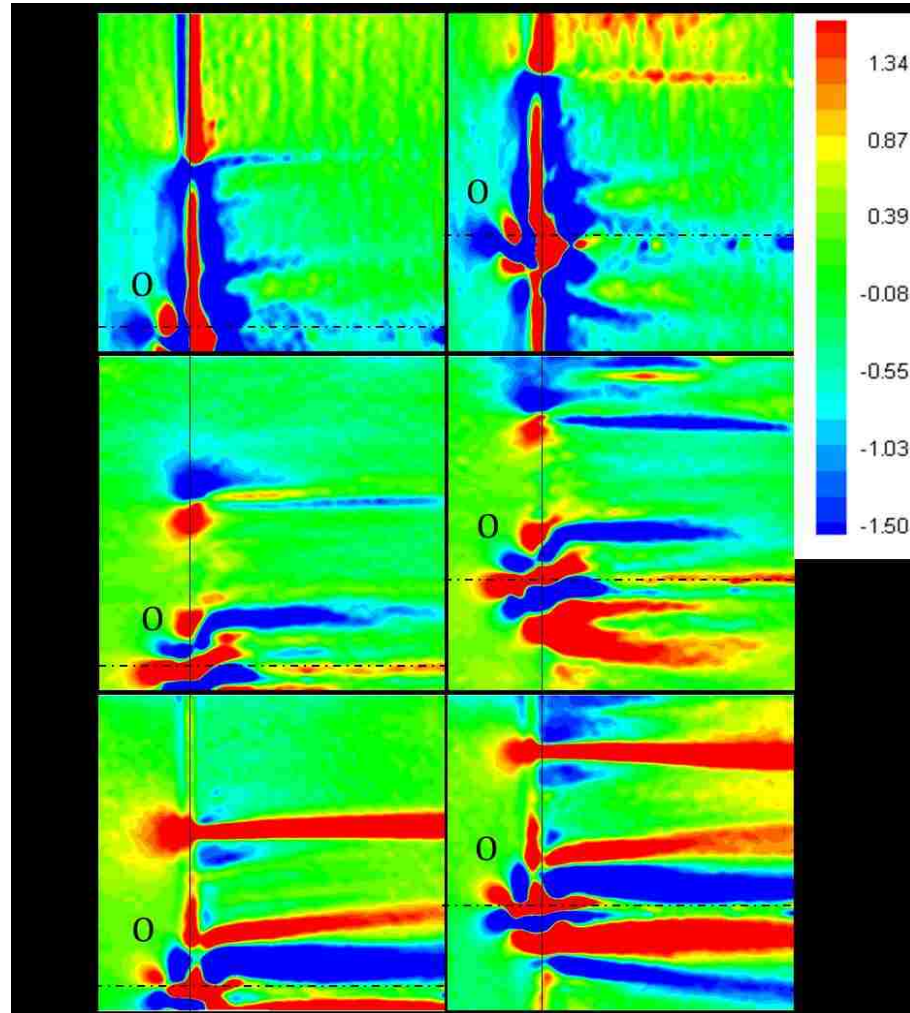
Figure 5.22: Time averaged contours of various strain rates at rotational speed of 180 for for $\delta h_U = 0.55$ (left column) and $\delta h_U = 0.27$ (right column): (a) principle strain rate U (S_{XX}), (b) principle strain rate V (S_{YY}), and (c) shear strain rate UV (S_{XY})

Higher strain rates (normal strain rates S_{xx}, S_{yy} and shear strain rate S_{xy}) were observed for $\delta h_U = 0.27$ (right column) compared to the case with $\delta h_U = 0.55$ (left column). Interaction of free surface with wake can be seen in all three contour plots (normal and shear stresses) for low tip clearance ratio. This supports our hypothesis of higher shear stresses for low tip

clearance value cases. Figure 5.23 plots $-\overline{u'w'}$ Reynolds stresses (left column) in the upper

bypass region for $\delta h_U = 0.55$ (Figure 5.23a), $\delta h_U = 0.27$ (Figure 5.23b), and $\delta h_U = 0.05$

(Figure 5.13c) where u' represents stream-wise velocity fluctuations and w' represents

transverse velocity fluctuations.
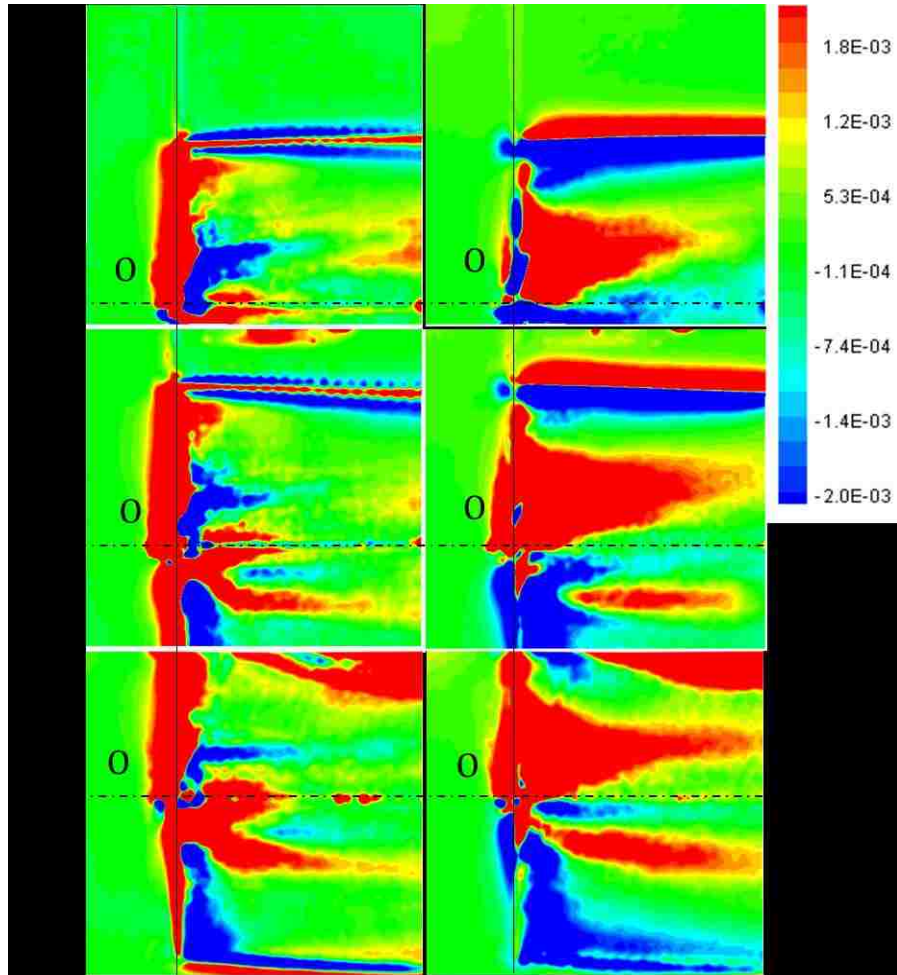
Figure 5.23: Time averaged statistics of $-\overline{u'w'}$ Reynolds stress (left column) and $-\overline{v'w'}$
Reynolds stress (right column) at rotational speed of 180 for δh_U of: (a) 0.55, (b) 0.27,
and (c) 0.05

A higher level of Reynolds stresses were observed in the vicinity of turbine rotation plane,

near hub, and along the tip vortex path. In addition, the lower tip clearance case ($\delta h_U =$

0.27) showed localized region of high $-\overline{u'w'}$ stresses near free surface that coincides with

region of high downward velocity in Figure 5.13. Further, the low tip clearance case also

171

exhibited stronger and larger regions of $-\overline{v'w'}$ stresses in wake region and in near-tip region. In addition, close proximity of turbine to the free surface increases turbulence intensities in the upper bypass and at the interface of wake and upper bypass regions. A region of high $-\overline{u'w'}$ and $-\overline{v'w'}$ Reynolds stresses in upper wake for $\delta h_U = 0.05$ is indicative of high turbulence stresses due free surface interacting with wake structures.

Contours of standard deviations of stream-wise, vertical and transverse velocities (normalized by channel velocity) from time averaged stereo-PIV measurements are plotted in Figure 5.24.
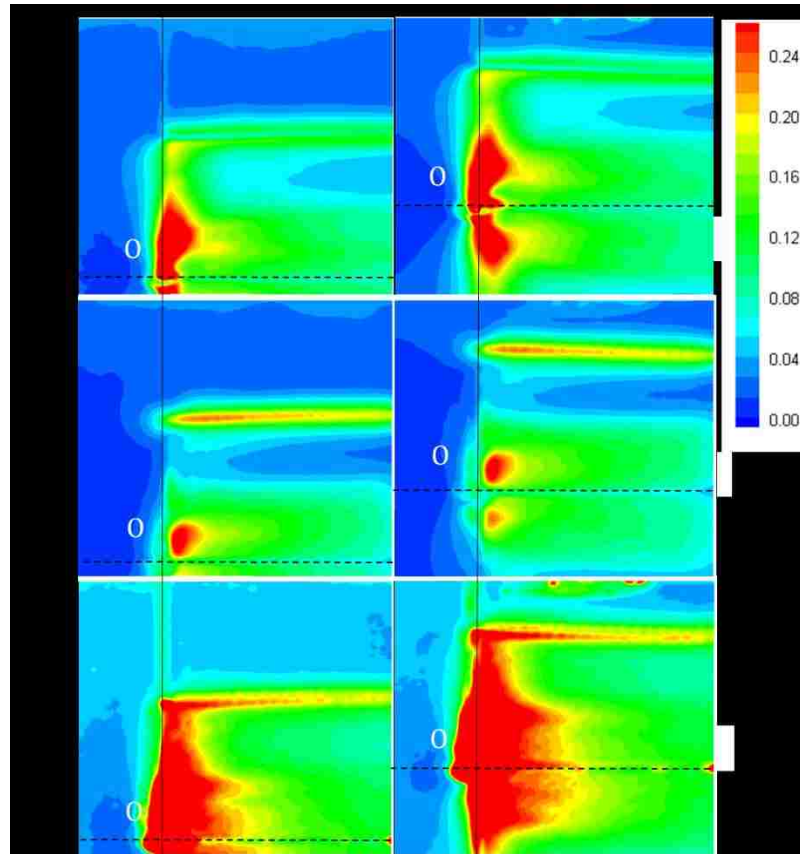
Figure 5.24: Time averaged statistics for $\delta h_U = 0.55$ (left column) and $\delta h_U = 0.27$ (right column) at rotational speed of 180 (a) Normalized standard deviation of stream-wise velocity ${\sigma_U}/{U_1}$, (b) Normalized standard deviation of vertical velocity ${\sigma_V}/{U_1}$, and (c) Normalized standard deviation of transverse velocity ${\sigma_W}/{U_1}$

Higher fluctuation in *U* and *V* velocities were observed for low immersion depth. Further, a region of reduced turbulence intensities was observed around 70% of span for both tip clearance ratios. The wake region showed regions of high turbulence intensities that extended between -0.4*R*<Y<0.4*R*. In transverse direction (Z), regions of high turbulence were observed up to ±0.4*R* and also along tip height (Figure 5.24c). A higher interaction was observed between wake and upper bypass flows for low tip clearance ratio of $\delta h_U = 0.27$ compared to $\delta h_U = 0.55$. Figure 5.25 plots contours of vorticity normalized by turbine diameter and free-stream velocity ($\omega D/U_\infty$) for rotational speed of 180RPM (Figure 5.25a) and 270RPM (Figure 5.25b) for $\delta h_U = 0.55$, (first column) and $\delta h_U = 0.27$ (second column).
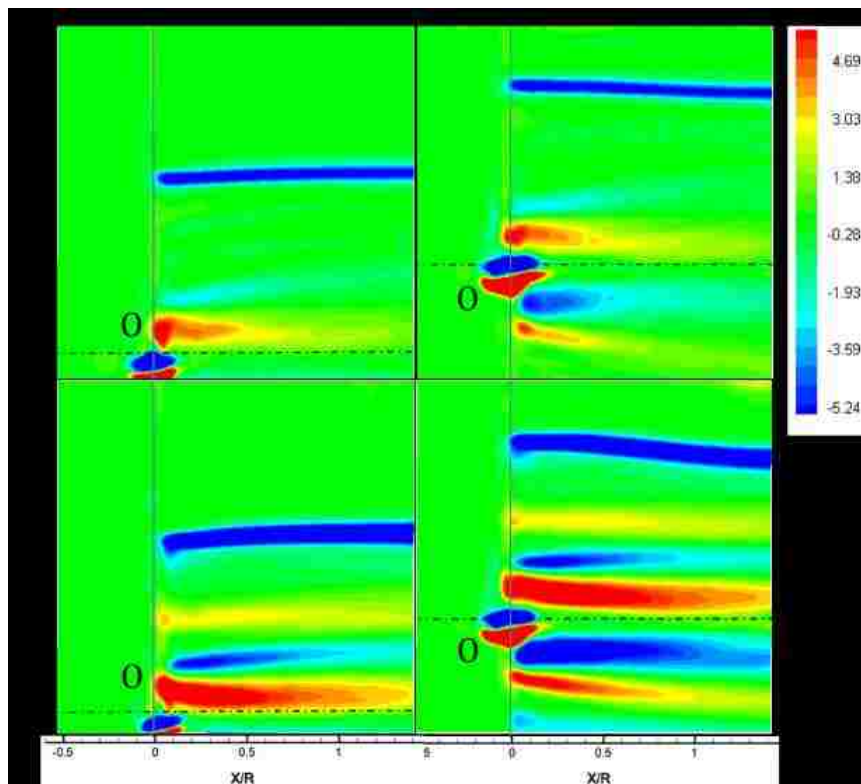
Figure 5.25: Time averaged statistics of normalized vorticity $\left(\omega D \big/ U_1 \right)$ for $\delta h_U = 0.55$ (left column) and $\delta h_U = 0.27$ (right column) at rotational speed of: (a) 180RPM and (b) 270RPM

Regions of high vorticity were observed near the blade tip locations and near-hub locations. Increasing the rotational speed from 180RPM to 270RPM resulted in increased vorticity levels as depicted in Figure 5.25 (compare Figures 5.25a with 5.25b). Further, the vortex filament at blade tip location is indicative of blade tip vortices which bounds the wake region. For a higher depth of immersion ($\delta h_U = 0.55$, first column), expanding vortex filament suggests radially expanding wake for both rotational speeds. However, for the lower depth of immersion ($\delta h_U = 0.27$, second column), with its downward propagation, the vortex filament tend to move closer to the turbine axis (Figure 5.25a, second column). With an increase in rotational speed, a further downward movement of vortex filament was observed (Figure 5.25b, second column). Thus, the lower submersion depth ($\delta h_U = 0.27$) hindered the wake expansion process, and resulted in radial compression of wake, the magnitude of which depended on rotational speed. In addition, a closer proximity to free surface was also observed to affect near-root vortex structure, with higher effects observed at larger rotational speeds (Figure 5.25, second column).

5.3.9 Phase averaged statistics for bypass and wake region:

Figure 5.26 present phase averaged stream-wise velocity contours for various rotational speeds and depths of immersions. Total 500 images are averaged per run that were captured every time a pre-marked turbine blade reaches horizontal position on the other side of light sheet as demonstrated in Figures 2.4 and 5.2. Figure 5.26a compares upper bypass and upper wake regions for $\delta h_U = 0.55$. At low rotation speed of 180RPM, three (circular) high velocity regions are observed approximately at blade tip height and are representative of tip vortices. For low rotation speed of 180 RPM, the wake inner core and outer core were found to be interacting with each other with intermediate regions of

high velocity. An increase in rotation speed to 242 RPM resulted in faster rotating wake with four vortices observed within the same downstream distance (1.4R). This also led to formation of additional low velocity structures IIa,b and IIIa,b as discussed earlier for time averaged statistics in Figure 5.11. The intermediate regions of high velocity that were observed for 180RPM case were compressed and limited to only near-tip and near-hub locations. Increasing the rotation speed to 270RPM (Figure 5.26c), resulted in further reduction in tip vortices spacing and formation of larger IIa, b and IIIa, b regions.

The contours of stream-wise velocity in upper bypass and upper wake regions for the case with $\delta h_U = 0.27$, are presented in Figure 5.26b. This case corresponds to the highest performance condition, due to wake compression effects caused by free surface drop. Comparison of Figures 5.26a with 26b show stronger wake and faster upper bypass regions for lower depths of immersion. Figure 5.26b (third column) plots contours of stream-wise velocity at 270RPM and depth of submersion of $\delta h_U = 0.27$. Compression of upper wake by faster upper bypass region is more evident at higher rotational speeds as elucidated in second and third columns of Figure 5.26b (dotted horizontal lines represent blade tip location). Upper wake region which is expected to expand with its propagation downstream the turbine (as in Figure 5.26a), is actually observed to compress in this case (see Figure 5.26b). Downwards movement of tip vortices (that bound the wake region) with their downstream propagation is indicative of wake compression process. This results in wake propagating to longer downstream distances behind turbine, which is an important consideration for farm layout design. Third and fourth tip vortices were found to be merging with upper bypass region developing faster secondary flow in the upper bypass region that was also observed in time averaged statics of Figure 5.11.
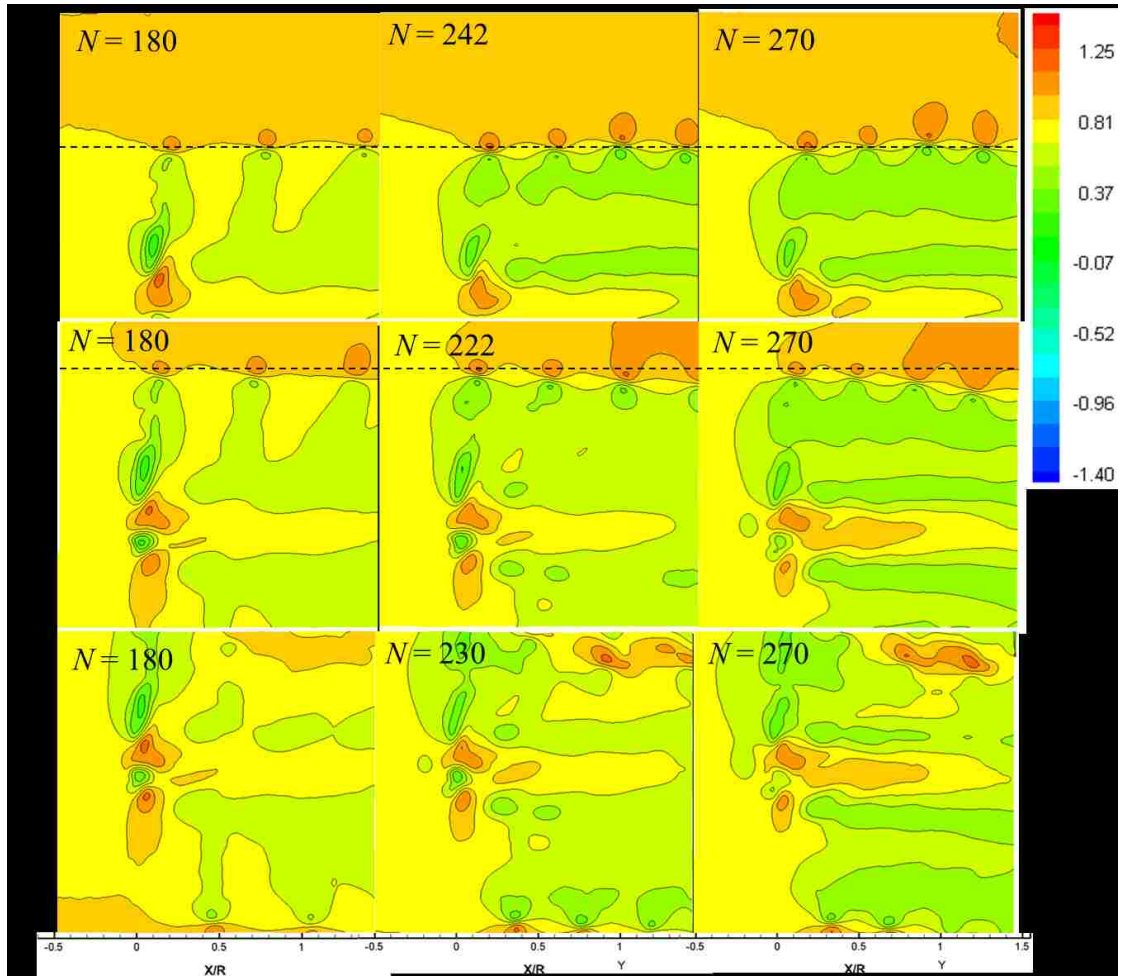
Figure 5.26: Contour plot of normalized stream-wise velocity $\left(U_{Normalized} = U/U_1\right)$ for δh_U of (a) 0.55, (b) 0.27, and (c) 0.05 at different rotational velocities (N)

Figure 5.26c presents contours of stream-wise velocity for $\delta h_U = 0.05$ rotational speeds of 180, 230 and 270 RPM in the upper region of interest. Even at low rotational speed of 180RPM, traces of upper bypass region penetrating into the upper wake can be seen in Figure 5.26c (first column), that are characterized by a high velocity region (identified as region V in Figures 5.10 and 11 earlier). The bypass region shows presence of only two vortical structures (tip vortices) compared to three vortical structures for δh_U = 0.55 for the same rotational speed. Further, upper wake lacks presence of outer wake core (region IIb) which was washed away for faster upper bypass region. Higher rotational

176

speed of 270RPM (third column) leads to formation of IIIa and IIIb regions in lower wake simultaneously increasing the strength of high velocity region V in combined upper bypass and upper wake region. The high velocity region was not just stronger but penetrated deeper into the upper wake indicating higher amplitude of free surface wave caused by faster rotating turbine. Authors would like to note here that the second column of Figure 5.26 corresponds to operational cases that yielded similar power coefficient value but operating at different values of rotational speeds and tip clearance ratios as depicted in Figure 5.26. For a similar value of Cp, an increase in free surface proximity ($\delta h_U = 0.55$ to 0.27 i.e. Figure 5.26a to 29b) requires reduction in rotational speed (from 242 to 222). However, a further increase in free surface proximity ($\delta h_U = 0.05$) requires a slight increment in rotational speed (to 230RPM) to maintain the Cp value. And it is interesting to note the widely different flow structures in the wake region for these cases as depicted in Figure 5.26 (second column), though they yield a similar performance behavior.

The phase averaged contours of normalized vorticity for rotational speed of 180RPM at various tip clearance ratios are plotted in Figure 5.27. The rectangle in Figure 5.27 represents radial position for first tip vortex-position corresponding to blade tip location. In an unbounded environment each tip vortex, during its downstream movement, is expected to move in radially outward direction, which is an indicative of expanding wake. This scenario was observed for the highest tip clearance ratio case experimented during current investigations ($\delta h_U = 0.55$). However, with decreasing tip clearance distance ($\delta h_U = 0.27$), the wake expansion process was inhibited due to free surface deformation that was also discussed earlier for Figures 5.11, 12, and 25. A slight downward

movement of tip vortex path was observed for $\delta h_U = 0.27$. However, with further decrease in free surface to blade
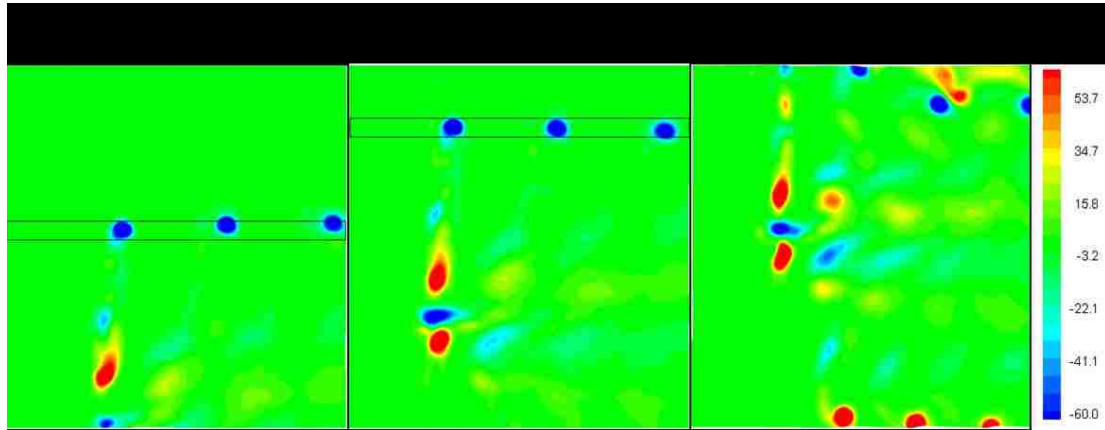
Figure 5.27: Phase averaged contours of normalized vorticity $\left(\omega D \middle/ U_1 \right)$ for δh_U of (a) 0.55, (b) 0.27 and (c) 0.05 at rotational speed of 180RPM

tip clearance ($\delta h_U = 0.05$), the vertical structures at blade tip were observed to penetrate into the upper wake as depicted in Figure 5.27.

5.4   CONCLUSIONS:

The results of experimental investigations to quantify the effect of free surface proximity and associated blockage effects on performance and flow-field of MHkT are presented. The experimental study was conducted with a constant chord, untwisted three bladed MHkT in a recirculating water channel. Experiments were carried out with turbine operating at various flow velocities and immersion depths over a range of *TSR* values. The experimental data were corrected to find contribution of blockage effect towards measured power using two different formulations: a closed-top formulation and an open surface blockage correction formulation. A comparison was presented between blocked and corrected datasets (from both formulations) in terms of changes in power coefficient, thrust coefficient and flow velocity to quantify blockage effects. An increase in flow velocity and

rotational speed was found to increase the blockage effect resulting in accelerated flow, improved power and thrust loading on turbine. Though both formulations are based on the measured experimental data, incorporation of free surface effects in blockage correction analysis resulted in prediction of higher blockage effects (upto 3-4% higher $\%\Delta C_p$). Additionally, experimental investigation with stereo-PIV to understand the effect of free surface proximity on blockage effects revealed free surface deformation behind turbine rotational plane leading to unsymmetric wake. The shape and intensity of free surface drop was found to be dependent on flow velocity, rotational speed and tip clearance distance. Maximum improvement in turbine performance characteristics was observed for $\delta h_U = 0.27$ for which additional blockage provided by wake compression (due to free surface drop) complimented the total blockage. The flow visualization based on stereo-PIV also revealed faster upper bypass region with elevated normal and shear stresses in upper bypass and wake region that lead to increased thrust and power coefficient at low tip clearance ratios. Moving the turbine further closer to the free surface ($\delta h_U = 0.05$) caused localized free surface drop that penetrated into the upper wake adversely affecting turbine performance. For $\delta h_U = 0.05$ case, stereo-PIV analysis showed high levels of turbulence intensities and Reynolds stresses in upper wake and bypass regions. The phase averaged PIV analysis showed presence of wake compression effects by the virtue of radially inward motion of tip vortex filament for low free surface proximity ($\delta h_U = 0.27$) and wake penetration by free surface for $\delta h_U = 0.05$.

CHAPTER 6

CONCLUSIONS AND RECOMMENDATIONS FOR FUTURE WORK

6.1 SUMMARY

The work presented in this dissertation investigated performance and flow-field of a Marine hydrokinetic turbine in its natural environment. This objective was achieved through analytical, computational and experimental studies that were discussed throughout this document. Analytical model was developed based on blade element momentum theory to investigate effect of rotational speed, flow speed, blade pitch, chord length, twist angle on hydrodynamic and structural performance of turbine. The analytical model was further extended to perform one way fluid-structure interaction analysis and a multi-objective optimization study for improving hydrodynamic and structural performance of turbine blades. Computational models were developed based on CFD methodology that consisted of steady state-rotating reference frame technique and transient sliding mesh motion models with VOF formulation for free surface modeling. Experimental investigations consisted of performance measurements with a lab-scale prototype in water channel. Torque and thrust measurements were carried out with a submerged torque-thrust sensor mounted in-line with the turbine shaft. Measurements were carried out at various flow velocity, rotational speeds, depths of immersions to understand effects of Reynolds number, Froude number on power and thrust developed by turbine. To understand the near-wake flow development and propagation, flow-field measurements were performed with stereoscopic PIV flow visualization technique for turbine operating at various rotational speeds and free surface proximities. Further, blockage correction methodologies were developed for two different scenarios: first, for a turbine operating in a closed-top water channel and second, for a turbine operating in near-free-surface environment to account for effect of blockage on turbine performance in absence and presence of free surface. The

results of analytical, computational and experimental investigations are summarized below:

6.2 A COUPLED HYDRO-STRUCTURAL DESIGN OPTIMIZATION FOR HYDROKINETIC TURBINES

A multi-objective hydro-structural optimization was presented in Chapter 3 for both constant chord, zero twist blade turbine and variable chord, twisted blade turbine designs. GA based on BEM proved to be a fast and efficient tool for hydro-structural optimization of HKTs. The results of optimization for a constant chord, zero twist blade design were supported with detailed CFD and FE analysis. Compared to the CFD analysis, the thrust and torque loading calculated from BEM are under-predicted near the blade tip and over-predicted elsewhere. But the integral performance parameters (total thrust and torque) calculated from BEM agree well the CFD analysis. The total thrust forces obtained from the BEM analysis were comparable to the FSI analysis within ~7% variation. Thus the BEM analysis offered a quick, reliable tool for multi-objective optimization which would have been virtually impossible with CFD analysis due to higher computational time involved. Though the BEM analysis was able to predict the total thrust and torque loading on a turbine, it could not capture the variation of these forces along the blade span due to inherent simplifications of the BEM theory. On the other hand, coupled CFD-FE analysis precisely determined this force distribution along the blade span and also considered the effect of blade root thickness. This resulted in larger deviation (up to 30%) between stress compared to forces calculated from BEM and FSI analysis. A variable chord, twisted blade turbine was found to improve structural performance of turbine without compromising any of the hydrodynamic efficiency. Three different blade designs were presented for different

rotational speeds and optimization was performed for variable chord, twisted blade design for hydro-structural performance improvement. The parametric study suggested that, lower values of blade pitch angles and chord lengths maximize the hydrodynamic performance while for the structural stability of turbine, a higher blade pitch angle and lower *TSR* are required. A hydro-structural optimization that was performed with GA for a constant chord blade turbine yielded a C_p of 0.47 with flap-wise bending stresses of ~210MPa. Further, for a constant chord blade design, a higher ΔP was observed across blade section near tip as compared to rest of the blade that leads to a non-uniform blade loading and is considered to be detrimental to turbine life. This also implies a higher contribution of near tip part of the blade towards thrust and torque loading. To reduce structural stresses and improve hydrodynamic performance, a design was presented with varying chord and twist distribution that resulted in entire blade surface contributing uniformly to thrust and torque loading thus improving hydro-structural performance of turbine. Hydro-structural optimization with a variable chord twisted blade turbine resulted in C_p of 0.55 (a 17% improvement compared to a constant chord design) with flap-wise bending stresses below 200MPa.

6.3 PERFORMANCE CHARACTERIZATION AND PLACEMENT OF A MARINE HYDROKINETIC TURBINE IN A TIDAL CHANNEL UNDER BOUNDARY PROXIMITY AND BLOCKAGE EFFECTS

In Chapter 4, the results of experimental and computational analysis for blockage effects, Reynolds number dependency and boundary proximity effects on flow-field and performance of a MHkT are presented. Experiments were carried out on a lab-scale MHkT at various flow velocities inside a 0.61m×0.61m test section open surface recirculating

water channel. CFD predictions based on rotating reference frame technique were in agreement with experimental data. CFD study was further extended to understand effect of flow Reynolds number and blockage ratio on turbine performance characteristics. Increasing flow velocity resulted in improved performance until 0.7m/s beyond which C_p vs. *TSR* curve was found to be insensitive to Reynolds number change. Further, effect of solid blockage on turbine performance was analyzed by varying the size of fluid domain for lab prototype model. Blockage ratio below 10% did not show any appreciable effect on turbine performance characteristics. Increasing the solid blockage ratio from 10% to 42% resulted in widening the operating *TSR* range with up to ~35% improvement in power coefficient. Higher *TSR* values were found to exhibit higher blockage effects (higher percentage increase in C_p compared to unblocked case) due to faster rotational speed that lead to stronger wake and faster bypass flow. Further, to understand effect of surface proximity on turbine performance and flow-field, experiments were carried out with turbine at different depths of immersion. An improvement in performance was observed when turbine axis was moved away from the channel bottom (channel bottom wall to blade tip clearance > turbine radius). This trend continued until turbine was raised to tip clearance of half radius distance below the free surface, after which reduced performance was observed. Beyond this height, appreciable free surface drop was observed behind turbine rotational plane restricting the wake expansion and propagation process resulting in reduced performance. A three dimensional transient CFD analysis (with VOF formulation) that was performed for wake and near-free surface flow characterization revealed presence of three distinct flow regions behind turbine: wake, upper bypass and lower bypass region. The flow structures in these regions were found to depend strongly on proximity to channel

bottom and free surface. For lower tip clearance ratios, a significant drop (up to 5 to 10% of channel depth) in free surface was also observed behind turbine with complex three dimensional flow structures that lead to a skewed wake affecting its expansion and restoration process. Further, a reduction in performance was observed when the turbine was operated close to the channel bottom wall. This can be attributed to two facts: first, the boundary layer and associated viscous effects at channel bottom wall that adversely affect the turbine performance, and second, absence of additional blockage due to free surface deformation that manifests when a turbine operates in proximity of a free surface. Since both distances were varied simultaneously, it is not possible to pin down the cause to the either of the cases described above. Free surface deformation and higher flow velocities in the upper bypass region (compared to lower bypass region) lead to an asymmetric wake behind the turbine. Transient CFD analysis at *TSR*=5.85 for all depths of immersion studied during present work did not show any flow separation effects on turbine blades suggesting that, free surface deformation is the primary mechanism for increased or reduced performance of turbine operating in free surface proximity environment. In addition to wake and bypass regions behind the turbine, the presence of turbine in flow channel was observed to affect flow upstream of the turbine as well. Our experimental investigations suggest that for optimum performance, MHkT should be installed such that, turbine rotational disc is at least one radial distance away from the solid channel wall and half radial distance below the free surface.

6.4 CHARACTERIZATION OF BLOCKAGE EFFECTS FOR A MARINE HYDROKINETIC TURBINE IN FREE SURFACE PROXIMITY ENVIRONMENT

The results of experimental investigations to quantify the effect of free surface proximity and associated blockage effects on performance and flow-field of MHkT were presented in Chapter 5. The experimental study was conducted with a constant chord, untwisted three bladed MHkT in a recirculating water channel. Experiments were carried out with turbine operating at various flow velocities and immersion depths over a range of *TSR* values. The experimental data were corrected to find contribution of blockage effect towards measured power using two different formulations: a closed-top formulation and an open surface blockage correction formulation. A comparison was presented between blocked and corrected datasets (from both formulations) in terms of changes in power coefficient, thrust coefficient and flow velocity to quantify blockage effects. An increase in flow velocity and rotational speed was found to increase the blockage effect resulting in accelerated flow, improved power and thrust loading on turbine. Though both formulations are based on the measured experimental data, incorporation of free surface effects in blockage correction analysis resulted in prediction of higher blockage effects (upto 3-4% higher %ΔC_p). Additionally, experimental investigation with stereo-PIV to understand the effect of free surface proximity on blockage effects revealed free surface deformation behind turbine rotational plane leading to unsymmetric wake. The shape and intensity of free surface drop was found to be dependent on flow velocity, rotational speed and tip clearance distance. Maximum improvement in turbine performance characteristics was observed for $\delta h_U = 0.27$ for which additional blockage provided by wake compression (due to free surface drop) complimented the total blockage. The flow visualization based

186

on stereo-PIV also revealed faster upper bypass region with elevated normal and shear stresses in upper bypass and wake region that lead to increased thrust and power coefficient at low tip clearance ratios. Moving the turbine further closer to the free surface ($\delta h_U = 0.05$) caused localized free surface drop that penetrated into the upper wake adversely affecting turbine performance. For $\delta h_U = 0.05$ case, stereo-PIV analysis showed high levels of turbulence intensities and Reynolds stresses in upper wake and bypass regions. The phase averaged PIV analysis showed presence of wake compression effects by the virtue of radially inward motion of tip vortex filament for low free surface proximity ($\delta h_U = 0.27$) and wake penetration by free surface for $\delta h_U = 0.05$.

6.5   RECOMMENDATIONS FOR FUTURE WORK

A MHkT operating in its natural environment is subjected to dynamic effects of incoming flow that affects its performance and flow-field around it. The current investigations provide a basis for understanding the effect of turbine geometry and operating conditions on the performance and flow-field of MHkT in its natural environment. The design-optimization and one way FSI framework presented in Chapter 3 are useful tools for efficient design of MHkT. This study can be further extended to understand the effects of blade deflections on turbine flow-field and interaction between the two. This can be achieved through two-way FSI by strongly coupling fluid and structural domains. Experimental investigations and transient CFD study presented in Chapter 4 addressed effects of operating variables – flow velocity, blockage ratio, and depths of immersions on lab-scale turbine performance. In chapter 5, flow-field investigations were discussed for the near-wake field for various rotational speeds and free surface proximities. The near-wake reflects the effects of turbine geometry and is very

important to understand its performance behavior. However, for a turbine operating in a farm layout, it is also important to understand effects of wake from upstream turbine on the incoming flow. Further, presence of free surface and its interaction with incoming wake is expected to complicate the incoming flow-field as demonstrated in Chapters 4 and 5. The present study can be extended to understand performance and flow-field of MHkT operating in a farm layout with free surface proximity environment. It will be very insightful to understand effect of turbine spacing and position, in free surface environment, on flow-field around MHkT in a farm layout.

LIST OF REFERENCES

1. Hall, D.G., Reeves, K.S., Brizzee, J., Lee, R.D., Carroll, G.R., and Sommers, G.L., *Wind and Hydropower Technologies, Feasibility Assessment of the Water Energy Resources of the United States for New Low Power and Small Hydro Classes of Hydroelectric Plants, Tech Report-Doe-Id-11263*, in *U.S. Department of Energy, Energy Efficiency and Renewable Energy*, Idaho National Laboratory, 2006.

2. Date, A. and Akbarzadeh, A., *Design and Cost Analysis of Low Head Simple Reaction Hydro Turbine for Remote Area Power Supply.* Renewable Energy, 2009. **34**: p. 409-415.

3. Korpela, S.A., *Principles of Turbomachinery*. 1 ed. 2011, Hoboken, NJ: Wiley. 457.

4. Consul, C.A., Willden, R.H.J., Ferrer, E., and McCulloch, M.D., *Influence of Solidity on the Performance of a Cross-Flow Turbine*. in *Proceedings of the 8th European Wave and Tidal Energy Conference*. 2009.

5. Chen, T.Y. and Liou, L.R., *Blockage Corrections in Wind Tunnel Tests of Small Horizontal-Axis Wind Turbines.* Experimental Thermal and Fluid Science, 2011. **35**: p. 565-569.

6. Bracmort, K., Stern, C.V., and Adam, V., *Hydropower:Federal and Nonfederal Investment*, Congressional Research Service, 2013.

7. *Dams and Developement - a New Framework for Decision Making*, World Commission on Dams, 2000.

8. Hall, D.G., Cherry, S.J., Reeves, K.S., Lee, R.D., Carroll, G.R., Sommers, G.L., and Verdin, K.L., *Water Energy Resources of the United States with Emphasis on Low Head/Low Power Resources*, Laboratory, I.N.E. and Environmental, Editors, U.S. Department of Energy, 2004.

9. Guney, M.S. and Kaygusuz, K., *Hydrokinetic Energy Conversion Systems: A Technology Status Review.* Renewable and Sustainable Energy Reviews, 2010. **14**: p. 2996-3004.

10. Jacobson, P., *Assessment and Mapping of the Riverine Hydrokinetic Resource in the Continental United States*, Electric Power Research Institute: Palo Alto, CA, 2012.

11. Haas, K.A., Fritz, H.M., French, S.P., Smith, B.T., and Neary, V., *The Assessment of Energy Production Potential from Tidal Streams in the United States*, Georgia Tech Research Corporation, 2011.

12. Stallard, T., Collings, R., Feng, T., and Whelan, J., *Interactions between Tidal Turbine Wakes: Experimental Study of a Group of Three-Bladed Rotors.* Phil Trans R Soc A, 2013. **371:20120159.**

13. Bahaj, A.S., Molland, A.F., Chaplin, J.R., and Batten, W.M.J., *Power and Thrust Measurements of Marine Current Turbines under Various Hydrodynamic Flow Conditions in a Cavitation Tunnel and a Towing Tank.* Renewable Energy, 2007. **32**: p. 407-426.

14. McTavish, S., Feszty, D., and Nitzsche, F., *An Experimental and Computational Assessment of Blockage Effects on Wind Turbine Wake Development.* Wind Energy, 2013.

15. Consul, C.A., Willden, R.H.J., and McIntosh, S.C., *Blockage Effects on the Hydrodynamic Performance of a Marine Cross-Flow Turbine*. Phil Trans R Soc A, 2013. **371:20120299**.

16. Maskell, E.C., *A Theory of the Blockage Effects on Bluff Bodies and Stalled Wings in a Closed Wind Tunnel*. Aeronautical Research Council London ed. 1963, Ft. Belvoir: Defense Technical Information Center.

17. Gould, R.W.F., *Wake Blockage Corrections in a Closed Wind Tunnel for One or Two Wall-Mounted Models Subject to Separated Flow*. 1969, London: HMSO.

18. Pope, A., *Wind-Tunnel-Boundary Corrections*, in *Wind-Tunnel Testing*. 1954, John Wiley & Sons Inc. p. 268-344.

19. Vermeer, L.J., Sorensen, J.N., and Crespo, A., *Wind Turbine Wake Aerodynamics*. Progress in Aerospace Sciences, 2003. **39**: p. 467-510.

20. Khan, M.J., Bhuyan, G., Iqbal, M.T., and Quaicoe, J.E., *Hydrokinetic Energy Conversion Systems and Assessment of Horizontal and Vertical Axis Turbines for River and Tidal Applications: A Technology Status Review*. Applied Energy, 2009. **86**: p. 1823-1835.

21. Whelan, J.I., Graham, J.M.R., and Peiro, J., *A Free-Surface and Blockage Correction for Tidal Turbines*. J. Fluid Mech., 2009. **624**: p. 281 - 291.

22. Goundar, J.N. and Ahmed, M.R., *Marine Current Energy Resource Assessment and Design of a Marine Current Turbine for Fiji*. Renewable Energy, 2014. **65**: p. 14–22.

23. Duquette, M.M. and Swanson, J., *Solidity and Blade Number Effects on a Fixed Pitch, 50w Horizontal Axis Wind Turbine*. Wind Engineering, 2003. **27**: p. 299-316.

24. Duquette, M.M. and Visser, K.D., *Numerical Implications of Solidity and Blade Number on Rotor Performance of Horizontal Axis Wind Turbines*. Journal of Solar Energy Engineering, 2003. **125**: p. 425-432.

25. Myers, L. and Bahaj, A.S., *Wake Studies of a 1/30th Scale Horizontal Axis Marine Current Turbine*. Ocean Engineering, 2007. **34**: p. 758-762; 758.

26. Myers, L. and Bahaj, A.S., *Power Output Performance Characteristics of a Horizontal Axis Marine Current Turbine*. Renewable Energy, 2006. **31**: p. 197-208.

27. Myers, L.E. and Bahaj, A.S., *Experimental Analysis of the Flow Field around Horizontal Axis Tidal Turbines by Use of Scale Mesh Disk Rotor Simulators*. Ocean Engineering, 2010. **37**: p. 218-227.

28. Neary, V.S., Fontaine, A.A., Bachant, P., Gunawan, B., Wosnik, M., Michelen, C., . . . Straka, B., *Us Department of Energy National Lab Activities in Marine Hydrokinetics: Scaled Model Testing of Doe Reference Turbines*. 10th European Wave and Tidal Energy Conference, Aalborg, Denmark, September 2-5, 2013, 2013.

29. Neary, V.S., Gunawan, B., Hill, C., and Chamorro, L.P., *Near and Far Field Flow Disturbances Induced by Model Hydrokinetic Turbine: Adv and Adp Comparison*. Renewable Energy, 2013. **60**: p. 1-6.

30. Glauert, H., *Airplane Propellers*, in *Aerodynamic Theory* Durand, W.F., Editor. 1935, Berlin:Springer Verlag.

31. Sørensen, J.N., *Aerodynamic Aspects of Wind Energy Conversion.* Annual Review of Fluid Mechanics, 2011. **43**: p. 427-448.

32. Hess, J.L., *Panel Methods in Computational Fluid Dynamics.* Annual Review of Fluid Mechanics, 1990. **22**: p. 255-274.

33. Young, Y.L., Motley, M.R., and Yeung, R.W., *Three-Dimensional Numerical Modeling of the Transient Fluid-Structural Interaction Response of Tidal Turbines.* Journal of Offshore Mechanics and Arctic Engineering, 2010. **132**: p. 011101.

34. Murray, J.C. and Barone, M., *The Development of Cactus, a Wind and Marine Turbine Performance Simulation Code.* 49th AIAA Aerospace Sciences Meeting including the New Horizons Forum and Aerospace Exposition, 4 - 7 January 2011, Orlando,Florida AIAA 2011-147, 2011.

35. Mukherji, S.S., Kolekar, N., Banerjee, A., and Mishra, R., *Numerical Investigation and Evaluation of Optimum Hydrodynamic Performance of a Horizontal Axis Hydrokinetic Turbine.* Journal of Renewable and Sustainable Energy, 2011. **3**: p. 063105.

36. Kang, S., Borazjani, I., Colby, J.A., and Sotiropoulos, F., *Numerical Simulation of 3d Flow Past a Real Marine Hydrokinetic Turbine.* Advances in water resources, 2012. **39**: p. 33-43.

37. Consul, C.A., Willden, R.H.J., and McIntosh, S.C., *Blockage Effects on the Hydrodynamic Performance of a Marine Cross-Flow Turbine.* Phil Trans R Soc A, 2013. **371:20120299**.

38. Churchfield, M.J., Li, Y., and Moriarty, P.J., *A Large-Eddy Simulation Study of Wake Propagation and Power Production in an Array of Tidal-Current Turbines.* . Phil Trans R Soc A, 2013. **371: 20120421**.

39. Batten, W.M.J., Harrison, M.E., and Bahaj, A.S., *Accuracy of the Actuator Disc-Rans Approach for Predicting the Performance and Wake of Tidal Turbines.* Phil Trans R Soc A, 2013. **371: 20120293**.

40. Hwang, I.S., Lee, Y.H., and Kim, S.J., *Optimization of Cycloidal Water Turbine and the Performance Improvement by Individual Blade Control.* Applied Energy, 2009. **86**: p. 1532-1540; 1532.

41. Dowell, E.H. and Hall, K.C., *Modeling of Fluid Structure Interactions.* Annual Review of Fluid Mechanics, 2001. **33**: p. 445-490.

42. Hou, G., Wang, J., and Layton, A., *Numerical Methods for Fluid-Structure Interaction - a Review.* Commun. Comput. Phys., 2012. **12**: p. 337-377.

43. Young, Y.L., *Fluid–Structure Interaction Analysis of Flexible Composite Marine Propellers.* Journal of Fluids and Structures, 2008. **24**: p. 799-818.

44. He, X.D., Hong, Y., and Wang, R.G., *Hydroelastic Optimisation of a Composite Marine Propeller in a Non-Uniform Wake.* Ocean Engineering, 2012. **39**: p. 14-23.

45. Selig, M.S. and Coverstone-Carroll, V.L., *Application of a Genetic Algorithm to Wind Turbine Design.* Journal of Energy Resources Technology, 1996. **118**: p. 22-28.

46. Belessis, M.A., Stamos, D.G., and Voutsinas, S.G., *Investigation of the Capabilities of a Genetic Optimization Algorithm in Designing Wind Turbine Rotors*. in *Proc. European Union Wind Energy Conf. and Exhibition*. 1996.

47. Fuglsang, P. and Madsen, H.A., *Optimization Method for Wind Turbine Rotors.* Journal of Wind Engineering and Industrial Aerodynamics, 1999. **80**: p. 191-206.

48. Medici, D., Ivanell, S., Dahlberg, J.Å., and Alfredsson, P.H., *The Upstream Flow of a Wind Turbine: Blockage Effect.* Wind Energy, 2011. **14**: p. 691-697.

49. Hu, D. and Du, Z., *Near Wake of a Model Horizontal Axis Wind Turbine.* Journal of Hydrodynamics, 2009. **21**: p. 285-291; 285.

50. Hu, H., Yang, Z., and Sarkar, P., *Dynamic Wind Loads and Wake Characteristics of a Wind Turbine Model in an Atmospheric Boundary Layer Wind.* Experiments in Fluids, 2012. **52**: p. 1277-1294.

51. Kolekar, N. and Banerjee, A., *A Coupled Hydro-Structural Design Optimization for Hydrokinetic Turbines.* Journal of Renewable and Sustainable Energy, 2013. **5**: p. 053146.

52. Lartiga, C. and Crawford, C., *Actuator Disk Modelling in Support of Tidal Turbine Rotor Testing*, in *3rd Int. Conf. on Ocean Energy*. 2010: Bilbao, Spain, .

53. Sun, X., Chick, J.P., and Bryden, I.G., *Laboratory-Scale Simulation of Energy Extraction from Tidal Currents.* Renewable Energy, 2008. **33**: p. 1267-1274.

54. Kolekar, N. and Banerjee, A., *Performance Characterization and Placement of a Marine Hydrokinetic Turbine in a Tidal Channel under Boundary Proximity and Blockage Effects.* Applied Energy, 2015. **148**: p. 121-133.

55. Myers, L.E. and Bahaj, A.S., *The Effect of Boundary Proximity Upon the Wake Structure of Horizontal Axis Marine Current Turbines*. in *27th International Conference on Offshore Mechanics and Arctic Engineering (OMAE 2008)*. 2008: The American Society of Mechanical Engineers.

56. Bahaj, A.S., Myers, L.E., Rawlinson-Smith, R.I., and Thomson, M., *The Effect of Boundary Proximity Upon the Wake Structure of Horizontal Axis Marine Current Turbines.* Journal of Offshore Mechanics and Arctic Engineering, 2011. **134**.

57. Birjandi, A.H., Bibeau, E.L., Chatoorgoon, V., and Kumar, A., *Power Measurement of Hydrokinetic Turbines with Free-Surface and Blockage Effect.* Ocean Engineering, 2013. **69**: p. 9-17.

58. Chamorro, L., Troolin, D., Lee, S.-J., Arndt, R.E.A., and Sotiropoulos, F., *Three-Dimensional Flow Visualization in the Wake of a Miniature Axial-Flow Hydrokinetic Turbine.* Experiments in Fluids, 2013. **54**: p. 1-12.

59. Whale, J., Anderson, C.G., Bareiss, R., and Wagner, S., *An Experimental and Numerical Study of the Vortex Structure in the Wake of a Wind Turbine.* Journal of Wind Engineering and Industrial Aerodynamics, 2000. **84**: p. 1-21.

60. Manar, F., Medina, A., and Jones, A., *Tip Vortex Structure and Aerodynamic Loading on Rotating Wings in Confined Spaces.* Experiments in Fluids, 2014. **55**: p. 1-18.

61. Garrett, C. and Cummins, P., *The Efficiency of a Turbine in a Tidal Channel.* Journal of Fluid Mechanics, 2007. **588**: p. 243-251.

62. Bai, X., Avital, E.J., Munjiza, A., and Williams, J.J.R., *Numerical Simulation of a Marine Current Turbine in Free Surface Flow.* Renewable Energy, 2014. **63**: p. 715-723.

63. Zhou, J.W. and Wang, D.Z., *Simulation of Tidal Stream Turbine Working near Free Surface.* Applied Mechanics and Materials, 2013: p. 361-363, 291.

64. Hirt, C.W. and Nichols, B.D., *Volume of Fluid (Vof) Method for the Dynamics of Free Boundaries.* Journal of Computational Physics, 1981. **39**: p. 201-225.

65. Betz, A., *Der Maximum Der Theoretisch Mölichen Ausnützung Des Windes Durch Windmotoren (the Maximum of the Theoretically Possible Exploitation of the Wind by Wind Motors).* Zeitschrift für das Gesamte Turbinenwesen, 1920. **17**.

66. Betz, A., *Windenergie Und Ihre Ausnutzung Durch Windmühen (Wind Energy and Its Application by Windmills).* Zeitschrift für das Gesamte Turbinenwesen , Göttingen, 1926.

67. Kolekar, N., Hu, Z., Banerjee, A., and Du, X., *Hydrodynamic Design and Optimization of Hydro-Kinetic Turbines Using a Robust Design Method*. in *Proceedings of the 1st Marine Energy Technology Symposium, METS13*. 2013. Washington, D.C.

68. Manwell, J.F., McGowan, J.G., and Rogers, A.L., *Wind Energy Explained: Theory, Design and Application*. Vol. 2nd. 2009, New York: John Wiley and Sons.

69. Mark, D. and Harold, Y., *Xfoil, subsonic Airfoil Development System*. http://web.mit.edu/drela/Public/web/xfoil/.

70. Degroote, J., Bathe, K.-J., and Vierendeels, J., *Performance of a New Partitioned Procedure Versus a Monolithic Procedure in Fluid-Structure Interaction.* Computers and Structures, 2009. **87**: p. 793-801.

71. Wilcox, D.C., *Turbulence Modeling for Cfd*. 3rd ed. 2006, La Canada, CA: DCW Industries.

72. Menter, F.R., Kuntz, M., and Langtry, R., *Ten Years of Industrial Experience with the Sst Turbulence Model, Edited by K. Hanjalic, Y. Nagano, and M. Tummers, Begell House, Inc.* Turbulence, Heat and Mass Transfer 4, 2003: p. 625 - 632.

73. Anderson, J.D., *Computational Fluid Dynamics: The Basics with Applications*. Mechanical Engineering Series, ed. McGraw Hill International, E. 1995: McGraw Hill International.

74. Adrian, R.J., *Particle-Imaging Techniques for Experimental Fluid Mechanics.* Annual Review of Fluid Mechanics, 1991. **23**: p. 261-304.

75. Zhang, S. and Hu, H., *Ch. 4: Stereo Particle Imaging Velocimetry Techniques*, in *Handbook of 3d Machine Vision Optical Metrology and Imaging*. 2013, Taylor & Francis 2013. p. 71-99.

76. *Insight 4g Data Acquisition, Analysis, and Display Software Platform - Users Guide, Tsi Inc.*, 2011.

77. Kline, S.J. and McClintock, F.A., *Describing Uncertainties in Single-Sample Experiments.* Mechanical Engineering, 1953. **75**: p. 3-8.

78. del Campo, V., Ragni, D., Micallef, D., Akay, B., Diez, F.J., and Simão Ferreira, C., *3d Load Estimation on a Horizontal Axis Wind Turbine Using Spiv.* Wind Energy, 2014. **17**: p. 1645-1657.

79. Raffel, M., Willert, C.E., and Kompenhans, J., *Particle Image Velocimetry: A Practical Guide*. 1998: Springer.

80. Adrian, R.J. and Westerweel, J., *Particle Image Velocimetry*. 2011: Cambridge University Press.

81. Prasad, A.K., Adrian, R.J., Landreth, C.C., and Offutt, P.W., *Effect of Resolution on the Speed and Accuracy of Particle Image Velocimetry Interrogation.* Experiments in Fluids, 1992. **13**: p. 105-116.

82. Lawson, N.J. and Wu, J., *Three-Dimensional Particle Image Velocimetry: Error Analysis of Stereoscopic Techniques.* Measurement Science and Technology, 1997. **8**: p. 894-900.

83. Stallard, T., Collings, R., Feng, T., and Whelan, J., *Interactions between Tidal Turbine Wakes: Experimental Study of a Group of Three-Bladed Rotors.* Phil Trans R Soc A, 2013. **371:20120159**.

84. Mark, D. and Harold, Y., *Xfoil User Guide.*

85. Kolekar, N.S., Mukherji, S.S., and Banerjee, A., *Numerical Modeling and Optimization of Hydrokinetic Turbine*, in *ASME 2011 5th International Conference on Energy Sustainability*. 2011: Washington, DC, USA. p. 1211-1218.

86. *Ansys Cfx 14 User's Guide*. 2011, ANSYS, Inc.

87. *Ansys Fluent 14.0 Theory Guide*. 2011, ANSYS, Inc.

88. *Ansys Cfx 14 Theory Guide*. 2011, ANSYS, Inc.

89. Menter, F.R., *Two-Equation Eddy-Viscosity Turbulence Models for Engineering Applications.* AIAA Journal, 1994. **32**: p. 1598-1605.

90. Menter, F.R., *Performance of Popular Turbulence Models for Attached and Separated Adverse Pressure Gradient Flows.* AIAA Journal, 1992. **30**: p. 2066-2072.

91. Giguère, P. and Selig, M.S., *Design of a Tapered and Twisted Blade for the Nrel Combined Experiment Rotor*, NREL: Golden, Colorado, 1999.

92. Madsen, H.A., Bak, C., Døssing, M., Mikkelsen, R., and Øye, S., *Validation and Modification of the Blade Element Momentum Theory Based on Comparisons with Actuator Disc Simulations.* Wind Energy, 2010. **13**: p. 373-389.

93. Neary, V., *Reference Inflow Characterization for River Resource Reference Model (Rm2)*, Oak Ridge National Laboratory: Oak Ridge, Tennessee, 2011.

94. Ponta, F.L. and Aref, H., *Numerical Experiments on Vortex Shedding from an Oscillating Cylinder.* Journal of Fluids and Structures, 2006. **22**: p. 327-344.

95. Holland, J.H., *Genetic Algorithms.* Scientific American, 1992.

96. Goldberg, D.E., *Genetic Algorithms in Search, Optimization and Machine Learning*. 1989: Addison-Wesley Longman Publishing Co., Inc. 372.

97. Okulov, V. and Sørensen, J.N., *Maximum Efficiency of Wind Turbine Rotors Using Joukowsky and Betz Approaches.* Journal of Fluid Mechanics, 2010. **649**: p. 497-508.

98. Giguère, P. and Selig, M.S., *New Airfoils for Small Horizontal Axis Wind Turbines.* ASME Journal of Solar Energy Engineering, 1998. **120**: p. 108-114.

99. Manwell, J.F., McGowan, J.G., and Rogers, A.L., *Aerodynamics of Wind Turbines*, in *Wind Energy Explained*. 2009, John Wiley & Sons, Ltd. p. 91-155.

100. Lee, J.H., Park, S., Kim, D.H., Rhee, S.H., and Kim, M.-C., *Computational Methods for Performance Analysis of Horizontal Axis Tidal Stream Turbines.* Applied Energy, 2012. **98**: p. 512-523.

101. van Kuik, G.A.M., Sørensen, J.N., and Okulov, V.L., *Rotor Theories by Professor Joukowsky: Momentum Theories.* Progress in Aerospace Sciences, 2015. **73**: p. 1-18.

VITA

The author was born to Sonapa and Suman Kolekar in Maharashtra, India on January 27th, 1982. He earned his Bachelor of Engineering degree in Mechanical Engineering from Shivaji University, India in May 2003. After his undergraduate studies, he served as a Scientist/Engineer for The Indian Space Research Organization, India. After four years of research and development activities, he decided to pursue higher studies and joined Missouri University of Science and Technology (formerly, University of Missouri, Rolla) for a Master of Science program in Mechanical Engineering. Promptly after completing his graduation in Fall 2010, he started his PhD studies under the mentorship of Professor Arindam Banerjee, initially at Missouri S&T and later at Lehigh University, where he graduated with a PhD in Spring 2015.